A Study of Magnetized Plasma Turbulence in the Nonrelativistic and Relativistic Regimes

by

Cristian S. Vega

A dissertation submitted in partial fulfillment of the requirements for the degree of

Doctor of Philosophy

(Physics)

at the

UNIVERSITY OF WISCONSIN-MADISON

2024

Date of final oral examination: 05/03/2024

The dissertation is approved by the following members of the Final Oral Committee:

Stanislav Boldyrev, Professor, Physics

Paul W. Terry, Professor, Physics

Ellen G. Zweibel, Professor, Astronomy and Physics

Carl R. Sovinec, Professor, Nuclear Engineering and Engineering Physics

To the massive globe of plasma that shines bright on the sky. This work wouldn't have been possible without it.

ACKNOWLEDGMENTS

It was May 2019 when I joined Stas Boldyrev's group after spending a couple of years wandering in a manner not too dissimilar from Brownian motion. I talked to many plasma physicists and astrophysicists in my search for a mentor, but Stas was the most persuasive when he said, and I'm paraphrasing, "I have summer funding". Just what I wanted to hear! The source of funding was, in fact, a summer visit to Los Alamos National Laboratory to collaborate with group T-5, under the mentorship of Gian Luca Delzanno. This would be the first of four summers I had the pleasure of working in T-5 (one of them remotely). I would like to thank Stas Boldyrev for his invaluable mentorship and Gian Luca Delzanno for his equally invaluable summer mentorship.

I would also like to thank the administration staff at T-5 for answering so many questions for me. And, of course, I thank the people from askIT@lanl who, when I contacted them with my university account saying that I could not access my LANL account, replied to the latter. But they would almost always fix my IT issues by the third or fourth time I asked:).

There is a third person whose contributions to this thesis were just as important as those of Stas and Gian Luca, who ran all the simulations in this manuscript and quite a few more not presented here, I'm talking about the one and only Vadim Roytershteyn. I thank him for all his help and hard work.

Last but not least, I would like to thank the taxpayers for funding my research.

— Cristian Vega (2024)

CONTENTS

Contents	iii	
List of Ta	bles	v

List of Figures vi

Abstract xiii

1	T . 1 1	1
	Introduction	- 1

- 1.1 The basic problem of turbulence 1
- 1.2 Hydrodynamic turbulence phenomenology 3
- 1.3 Plasma turbulence 9
- 1.4 Energy dissipation in collisionless plasmas 15
- 1.5 Magnetic reconnection 19
- 1.6 Relativistic plasma turbulence as a particle accelerator 21

2 Plasma turbulence in environments with low electron beta 25

- 2.1 Inertial kinetic Alfvén turbulence 25
- 2.2 Electron-only magnetic reconnection 37
- 2.3 Role of current sheets in energy dissipation 50
- 2.4 Discussion 53

3 Turbulence in relativistic plasmas 55

- 3.1 What is a relativistic plasma and why is it important? 55
- 3.2 Numerical simulations 57
- 3.3 Turbulence in strongly magnetized relativistic plasmas 60
- 3.4 Particle energization in relativistic plasma turbulenece 77
- 3.5 A closer look at acceleration by Alfvénic turbulence 86

- 3.6 Spatial intermittency of fast particles 99
- 3.7 Discussion109
- 4 Conclusions113
- ${f A}$ Low-frequency waves in a relativistic plasma 116
- $\, {\bf B} \,$ Curvature acceleration: the logarithmic factor 125
- C The critical energy127

References 130

LIST OF TABLES

3.1	Summary of the runs	59
3.2	Parameters of the velocity fluctuations for the electron fluid, and for the bulk	
	plasma motion, $\boldsymbol{U}=(n_i\boldsymbol{U}^i+n_e\boldsymbol{U}^e)/(n_i+n_e)$. Here, $\tilde{\gamma}^e$ is the Lorenz factor	
	associated with the electron fluid velocity and γ to the particle velocity. The	
	measurements are made at $ct/l=76$ for run VII and $ct/l=33$ for run VIII	76
3.3	Parameters of the runs and the corresponding predicted and measured exponents	
	of the particle distribution function, $f(\gamma)d\gamma \propto \gamma^{-\alpha}d\gamma$. The middle column states	
	the time when both the magnetic compressibility and observed slope were measured.	84

LIST OF FIGURES

1.1	Example of electron-only magnetic reconnection site found in one of the 2.5D	
	particle-in-cell simulations to be analyzed in Chapter 2. The color map shows	
	the out-of-plane (and guide-field-parallel) current density, J_z , normalized to the	
	root-mean-square out-of-plane current density computed over the whole simulation	
	domain. The thin black lines represent the magnetic field lines. The large, red	
	arrows exhibit the direction of the particle (electrons) inflow and outflow. On the	
	axes, d_e refers to the electron inertial scale	20
2.1	Top: Energy spectra of magnetic fluctuations. Bottom: Magnetic compressibility	
	$\delta B_{\parallel}^2/\delta B_{\perp}^2$. The red solid line is Equation (2.28) and the black dotted lines show	
	its asymptotic limits $1/(1+2/\beta_i)$ and 1. The green dashed line marks the scale	
	given by Equation (2.2), where the frequency of Alfvén waves no longer satisfies	
	$\omega \ll k_{\parallel} v_{\rm th,e}$. Figure 5 in Chen and Boldyrev (2017), copied here with the authors'	
	permission	34
2.2	Left: Magnetic (blue) and electric (red) energy spectra. Right: Magnetic com-	
	pressibility. The dashed line shows the analytic prediction of Equation 2.28. In	
	both panels, the vertical lines mark scales corresponding to (in order of increasing	
	k_{\perp}) $k_{\perp}d_e=1$ and $k_{\perp}\rho_e=1$	36
2.3	Contour lines of the magnetic potential ψ (black) and saddle points of ψ (blue).	
	Left: $\beta_e = 0.04$. Right: $\beta_e = 0.5$. Visual inspection reveals electron-only	
	reconnection candidates in both cases; the green-red X signs mark the specific	
	regions analyzed in detail below. The red and green lines were traced following	
	the direction of the (orthogonal) Hessian eigenvectors at the corresponding saddle	
	points	39

2.4	Profiles around the Λ -points marked on Figure 2.3. Direction ξ_1 corresponds to	
	the Hessian eigenvector directed along the outflow, while ξ_2 is directed along the	
	inflow. The X-point found by the Matlab algorithm is at $\xi_1 = \xi_2 = 0$. In the	
	$\beta_e = 0.5$ example, the J_z peak and the zero of the outflow velocity deviate from	
	the position of the X -point, which is expected since the reconnection layer is not	
	perfectly symmetric (e.g., Cassak and Shay, 2007; Doss et al., 2015). In both	
	cases, a large-scale plasma flow at the X-point results in nonzero mean electron	
	and ion flows in the reconnection layer	40
2.5	Current sheets found (in green). The red Xs are the current peaks of those sheets	
	containing saddle points (blue circles)	42
2.6	Example of reconnection candidate. Top-left: The color map shows the y compo-	
	nent of the electron flux and the arrows show the electron fluid velocity. Bottom-	
	left: Profiles of different fields along the inflow (direction X_1 ; red line in top panel)	
	and the outflow (direction X_2 ; green line in top panel). Top-right: Color map of	
	pressure-strain interaction. Bottom-right: Ion (blue) and electron (red) velocities	
	along outflow. The horizontal scale spans about $5d_i$, or half the domain length in	
	the field-perpendicular plane. There is no ion coupling to the electron motion. $$.	47
2.7	Left panel: Example of skeletonization of a current sheet. The red curve traces	
	the boundary of the current sheet as defined in the text. The curve within is the	
	skeleton obtained with the medial axis transform, with the color code representing	
	the shortest distance to the red boundary. Right panel: Color map of the same	
	current sheet	49
2.8	Histograms of half-thicknesses T (top), half-lengths L (middle), and aspect ratios	
	T/L (bottom) of the 2D current sheets, with different sets shown in different	
	colors. The number of 2D current sheets in each case is shown in parentheses.	
	The blue dots mark the centers of the bins. The data denoted by different colors	
	belong to the same bins but are shifted for clarity	51

2.9	Left: Average pressure-strain interaction around points of the current sheet	
	skeletons where the current density is above the threshold shown on the horizontal	
	axis. The pressure-strain interaction is normalized to its average over the whole	
	domain and the current density is normalized to its rms value. Right: Fraction	
	of the overall pressure-strain interaction contributed by the vicinity of points of	
	current sheet skeletons (in blue). The fractional volume occupied by the region	
	around skeletons where pressure-strain interaction was computed (in red). $$	53
3.1	Top left: Time evolution of energy in electromagnetic fluctuations normalized to	
	its initial value for runs II, IV, IX, and X, with guide field satisfying $B_0 \lesssim \delta B_0$.	
	The horizontal line is at half the initial energy. Top right: Time evolution of energy	
	in electromagnetic fluctuations normalized to its initial value for run VII, with	
	guide field satisfying $B_0 \gg \delta B_0$. Bottom left: Time evolution of root-mean-square	
	velocity of bulk plasma fluctuations for runs II, IV, IX, and X. Bottom right:	
	$\label{thm:continuous} \mbox{Time evolution of root-mean-square velocity of bulk plasma fluctuations for run VII.}$	59
3.2	Electric and magnetic energy spectra of runs II (top), IV (middle), and VI (bottom).	
	The sequence from the top to the bottom illustrates the growing deviation from	
	quasineutrality as σ_0 increases	68
3.3	The magnetic and electric spectra, and the total electromagnetic energy spectrum,	
	for two different magnetizations. The total energy spectrum approaches a $k^{-3/2}$	
	power-law at $k_{\perp}d_e \ll 1$, and a $k^{-3.5}$ power-law at $k_{\perp}d_e \gg 1$	69
3.4	The spectra of the normalized residual energy for two different magnetizations,	
	averaged over nine data cubes covering the indicated intervals of turn-over times.	
	The solid lines are shown for the reader's reference	69
3.5	The cosine of the alignment angle φ_{λ} between the magnetic and electric fluctuations	
	in numerical simulations. The results are averaged over nine data cubes covering	
	the indicated time intervals. The straight lines are shown for reference	70

3.6	Spectra of electric and magnetic fluctuations in the large-box run VII. The total	
	energy spectrum is slightly steeper than k^{-3} , but is consistent with the spectrum	
	including a logarithmic intermittency correction, cf. Equations (3.23) and (3.24).	73
3.7	The electric and magnetic spectra for the small-box run VIII. The left panel shows	
	the spectra of the perpendicular components of electric and magnetic fields, as	
	well as the spectrum of E_z . The E_z -spectrum is concentrated at the nonrelativistic	
	inertial scale defined in Equation (3.26) and corresponds to the ordinary mode	
	produced by the initial magnetic perturbations. The right panel shows the kinetic-	
	Alfvén spectra where the fluctuations associated with the ordinary mode have	
	been removed. The spectra indicated by the solid lines are given for the reader's	
	orientation	74
3.8	Frequencies of the ordinary fluctuations and the potential fluctuations measured	
	in Run VIII according to Equations (A.15) and (3.28). Here, we denote $d_p \equiv c/\omega_p$,	
	where the relativistic plasma frequency ω_p is defined in Equation (3.25), and	
	$\Omega_{\rm ce,rel} \equiv \Omega_{\rm ce}/\langle \gamma \rangle$, where $\Omega_{\rm ce}$ is the nonrelativistic electron cyclotron frequency and	
	$\langle \gamma \rangle$ is given in Table 3.2	75
3.9	The magnetic-field strength distribution functions and the corresponding mag-	
	netic compressibilities κ . The distribution is independent of the magnetization	
	parameter but depends on the relative strength of the applied magnetic field	81
3.10	The particle energy distribution functions in runs I, II (top-left), III, IV (top-right),	
	V, VI (middle row), IX, and X (bottom). The lines indicating power-law slopes	
	are given for reference. The middle-right panel shows a log-normal fit on run VI,	
	$f(\gamma) \propto \gamma^{-1} \exp[-(\ln \gamma - \mu)^2/(2\sigma_s^2)]$	85
3.11	Electron energy distribution functions. The black dashed lines show log-normal	
	fits, $f(\gamma) \propto \gamma^{-1} \exp[-(\ln \gamma - \mu)^2/(2\sigma_s^2)]$	86

3.12	The electron distribution functions. Here, p_{\parallel} and p_{\perp} are particle momenta in the	
	directions parallel and perpendicular to the background magnetic field $m{B}_0$. The	
	functions are strongly anisotropic. The anisotropy at very large energies is slightly	
	less pronounced in run VIII, which is likely a consequence of the smaller box size.	86
3.13	Sketch of a curved magnetic field line. The projection of the line on the plane	
	normal to the background magnetic field $m{B}_0$ is shown. For simplicity, it is assumed	
	that the magnetic structure moves with velocity $\boldsymbol{\beta}$ in the direction parallel to the	
	field-line curvature. An electron propagating along the curved line, experiences	
	curvature acceleration	89
3.14	Sketch of an electron-mirror interaction for $small$ pitch angles. For simplicity,	
	velocity $\boldsymbol{\beta}$ is directed along the magnetic mirror axis	94
3.15	Sketch of an electron-mirror interaction for <i>large</i> pitch angles. For simplicity,	
	velocity $\boldsymbol{\beta}$ is directed along the magnetic mirror axis	95
3.16	Electric and magnetic energy spectra for simulations with $B_0/\delta B_0=1$ (left panel)	
	and $B_0/\delta B_0=10$ (right panel). Note rather weak parallel electric field fluctuations.	
	The slopes indicated by the solid black lines are given for the reader's orientation.	96
3.17	Particle energy probability density function for simulations with $B_0/\delta B_0=1$ (left	
	panel) and $B_0/\delta B_0=10$ (right panel). In the case of a moderate guide field,	
	the energy distribution function has a power-law tail. In the case of a strong	
	guide field, the high-energy tail is well approximated by a log-normal function	
	$f(\gamma) \propto \gamma^{-1} \exp[-(\ln \gamma - \mu)^2/2\sigma_s^2]$, with $\mu \approx 2.6$ and $\sigma_s^2 \approx 0.61$. This function is	
	shown by the dashed line. Note the significantly longer time required to accelerate	
	the particles in the case of a strong guide field.	97

pitch angle distribution of ultrarelativistic particles ($\gamma > 100$) for simulations	
with a moderate guide field, $B_0/\delta B_0=1$ (left panel) and a strong guide field,	
$B_0/\delta B_0 = 10$ (right panel). In the case of a strong guide field, the pitch angles	
are extremely small. In the case of a moderate guide field, the pitch angles of	
accelerated particles crucially depend on the particle's energy. For energies smaller	
than the critical energy, $\gamma \ll \gamma_c$ (in this run, $\gamma_c \approx 70$), the particles are accelerated	
mostly along the background magnetic field. Above the critical energy, $\gamma \gtrsim \gamma_c$,	
particles with larger pitch angles are accelerated more efficiently	98
Sketh of particle interaction with a strong magnetic mirror moving with a plasma	
element	102
Probability density function of particle density n (number of particles per cell) for	
2.5D run IV (left) and 3D run IX (right) simulations, both with $\sigma_0 = 40$. Both	
curves are well approximated by a log-normal distribution around the peak and a	
normal distribution at low particle density $(n \ll 100)$	104
Left column: Particle energy pdfs. Quasi-steady states with well-established	
power-law tails are reached within one or two light-crossing times l/c of the	
electromagnetic fluctuation energy falling off to half of its initial value. Right	
column: Particle density pdfs for ultrarelativistic particles. Evidence of strong	
intermittency (non-Gaussianity) can be seen in the large-density power-law tails.	
The power slopes α and $\alpha + 1$ are given for the reader's orientation	106
	with a moderate guide field, $B_0/\delta B_0=1$ (left panel) and a strong guide field, $B_0/\delta B_0=10$ (right panel). In the case of a strong guide field, the pitch angles are extremely small. In the case of a moderate guide field, the pitch angles of accelerated particles crucially depend on the particle's energy. For energies smaller than the critical energy, $\gamma \ll \gamma_c$ (in this run, $\gamma_c \approx 70$), the particles are accelerated mostly along the background magnetic field. Above the critical energy, $\gamma \gtrsim \gamma_c$, particles with larger pitch angles are accelerated more efficiently

3.22 Top left: The color map shows the distribution of magnetic-field strength in the simulation domain. Top right: The color map shows the synchrotron radiation proxy $R = \sum_i \gamma_i^2 \beta_i^2 \sin^2 \theta_i B^2 / B_0^2$, where the sum is over the electrons in each cell in Run II and only the energetic particles with $\gamma > 100$ are taken into account. This is a proxy of the synchrotron radiation that would be emitted by electrons if this effect was included in the simulation. Note the logarithmic scale used in the color code, which implies very strong variations of the intensity of radiation in the simulation domain (the bottom of the color bar identifies all cells where $R < 10^4$). Bottom left: An enlarged subdomain indicated by the square in the top left panel. The color map shows the total magnetic field |B| and the black dots identify cells where there are more than 10 energetic ($\gamma > 100$) particles. Bottom right: The color map shows the magnetic fluctuations in the z direction δB_z . The field lines of the in-plane magnetic field δB_{\perp} are shown in red. The clusters of particles seem to concentrate in the vicinity of magnetic structures and align with the magnetic field lines. For the reader's orientation, we note that the gyroradius of ultrarelativistic particles scales in the presented simulation as $\rho_e \approx (\gamma/10)d_e$.

ABSTRACT

Turbulence is ubiquitous in space and astrophysical plasmas and is believed to play an important role in particle heating and nonthermal acceleration. These plasmas are commonly threaded by an external magnetic field imposed by the object they surround (e.g., planet, star), making magnetized plasma turbulence a problem of significant interest. In this thesis, we use numerical simulations to study two relatively unexplored regimes of magnetized plasma turbulence, viz., the sub-electron inertial scale in nonrelativistic low electron beta plasmas and both the magnetohydrodynamic and kinetic scales in relativistically hot plasmas. Phenomenology is used to model the energy distribution of turbulent fluctuations and particles.

In the nonrelativistic regime studied, energy dissipation is seen to be strongly intermittent, concentrating on electron-scale current sheets. A few of these current sheets exhibit signatures of electron-only reconnection.

The particle energy probability density function in the relativistic regime displays a nonthermal tail of ultrarelativistic particles that goes from power-law-like to log-normal as the guide field is increased. We propose that this can be understood in terms of the acceleration mechanism that dominates in each case. Also noteworthy is the observed intermittency in the spatial distribution of ultrarelativistic particles.

1.1 The basic problem of turbulence

The cover of the book "Turbulence" by Uriel Frisch shows a page of Leonardo da Vinci's notes from his lifelong studies on hydrodynamics. In it, drawings of different flows can be seen, including a couple displaying the formation of very complicated – turbulent – structures. Da Vinci's experimental research on turbulent water flows was surely remarkable for the time and even presaged some modern ideas (e.g., eddies spanning multiple scales) but, having lived in the pre-Newtonian era, he lacked both the physical and mathematical tools to provide a proper quantitative description of his observations and his conclusions were not always in line with modern fluid theory (Marusic and Broomhall, 2021).

It is an understatement to say that in the five centuries since da Vinci's passing physics and mathematics have advanced a great deal. Among the remarkable developments of theoretical physics is the discovery in the 19th century of the Navier-Stokes equation (Navier, 1823; Stokes, 1843), which is the dynamical equation governing incompressible flows. Today it is even possible to solve this equation on a computer and reproduce the turbulent flows da Vinci observed in the 15th and 16th centuries (Colagrossi et al., 2021).

It is noteworthy that turbulence emerges in numerical simulations that solve the Navier-Stokes equation, as it suggests that this phenomenon is contained in it (in the case of incompressible hydrodynamics). However, to say that we truly understand turbulence we would like to have a mental picture of the phenomenon that can be turned into a precise mathematical model to be corroborated or falsified against experiments and simulations. The complexity of the turbulent flow suggests that one should try to model the statistical properties of turbulence¹, ideally using quantities that are easy to measure in experiments or simulations. A first-principles understanding of turbulence based on the dynamical equation

¹For a more rigorous justification for a probabilistic description of turbulence, see Frisch (1995), Chapter 3.

would be highly desirable, but this is an extremely challenging mathematical problem that remains evasive to this day (although advances in this direction are taking place; see, for example, Eyink (2018b,a)).

An alternative to the first-principles approach is the use of phenomenology, where the dynamical equation is complemented by unproven but plausible assumptions inferred from empirical observations. This was the approach successfully followed by Andrey Kolmogorov to derive the second and third order structure functions (Kolmogorov, 1941a,b), obtaining the celebrated K41 theory, to be reviewed in the next section.²

The main topic of this dissertation is magnetized plasma turbulence, ubiquitous in space and astrophysical systems (e.g., heliosphere, magnetosphere, accretion disks; see Biskamp (2003); Bruno and Carbone (2013)). By magnetized we mean that the plasma is subjected to an externally imposed magnetic field, which we will refer to as guide field. In plasma turbulence, we have the additional complication of the formation of turbulent structures in the electromagnetic field. Moreover, the low collisionality typical of space and astrophysical plasmas and the different possible values of the plasma parameters (e.g., magnetic guide field, plasma beta) will offer us a wide variety of turbulent regimes that should keep plasma physicists entertained and employed for the foreseeable future.

Numerical simulations are even more important in plasma turbulence than in hydrodynamics, as in situ measurements of the space and astrophysical plasmas of interest require at best sending expensive probes into the magnetosphere or heliosphere, and at worst into astrophysical systems so distant that the project would violate the implicit rule of science that the researchers should still be alive by the start of the data collection.

In this dissertation, we use numerical simulations to study relatively unexplored regimes of magnetized plasma turbulence, viz., plasmas with low electron beta (and ion beta of order one) and relativistically hot plasmas. Phenomenology will be used to interpret the results and, in some cases, to derive mathematical models that can be contrasted against numerical

²We also note that the second order structure function was independently arrived at by Alexander Obukhov (Obukhov, 1941).

observations (for example, the energy spectrum).

Throughout the rest of this introduction, we will go over the background material necessary to understand the motivation and methodology of the work that will be presented in Chapters 2 and 3.

1.2 Hydrodynamic turbulence phenomenology

In this section, we illustrate the idea of turbulence phenomenology by briefly reviewing the well-understood hydrodynamic case. Thus, we will work out Kolmogorov 1941 theory, or just K41. The reader interested in more extensive treatises should check Frisch (1995) and Biskamp (2003).

To use phenomenology we need to have a good mental picture of the phenomenon we intend to describe, so let us begin this section by presenting the Navier-Stokes equation for an incompressible fluid:

$$\partial_t \boldsymbol{U} + (\boldsymbol{U} \cdot \nabla) \boldsymbol{U} = -\nabla \left(\frac{P}{\rho}\right) + \nu \nabla^2 \boldsymbol{U} + \boldsymbol{f},$$
 (1.1a)

$$\nabla \cdot \boldsymbol{U} = 0, \tag{1.1b}$$

where U(x,t) is the fluid velocity field, P(x,t) is the pressure, assumed isotropic, f is any external force per unit mass (it could be gravity or it could be the force with which you stir your tea), ρ is the mass density (which we are assuming uniform for simplicity), and ν is the kinematic viscosity (also assumed uniform). The first line is simply Newton's second law applied to a fluid element. The second line is the condition of incompressibility. These equations are to be complemented by initial and boundary conditions.

Let us now define the longitudinal structure function of order p, $S_p^{\parallel}(\mathbf{r}, \boldsymbol{\ell}, \mathcal{T})$, a quantity that is easy to measure in experiments (for low p) and that will be useful in our phenomenological

study of turbulence:

$$S_p^{\parallel}(\boldsymbol{r},\boldsymbol{\ell},\mathcal{T}) \equiv \langle \delta U_{\parallel}^p(\boldsymbol{r},\boldsymbol{\ell},t) \rangle, \quad \delta U_{\parallel}(\boldsymbol{r},\boldsymbol{\ell},t) \equiv \left[\boldsymbol{U}(\boldsymbol{r}+\boldsymbol{\ell},t) - \boldsymbol{U}(\boldsymbol{r},t) \right] \cdot \frac{\boldsymbol{\ell}}{\ell}, \quad (1.2)$$

where p > 0 is an integer and $\ell = |\boldsymbol{\ell}|$. The averaging $\langle ... \rangle$ should formally be defined as an ensemble average but, in practice, it is replaced by a time average by invoking the ergodic theorem, as it is easy to measure velocity at a fixed position. Structures of infrequent occurrence become increasingly important as p grows, making it difficult to measure the structure function for high p, as it requires to keep collecting data for a long time. Note that, for now, we keep the dependence on the position vector \boldsymbol{r} , the separation vector $\boldsymbol{\ell}$, and the time \mathcal{T} which represents the moment when we start collecting data (to be distinguished from the time t of the instantaneous velocity, as we are averaging over it). Later, we will postulate that the longitudinal structure function only depends on ℓ .

It is convenient to rewrite the Navier-Stokes equation in dimensionless form, so let us introduce a velocity scale U_0 and a length scale L_0 . There is more than one way to choose these scales. For example, for water flowing past an obstacle, U_0 could be the speed of the flow far from the obstacle and L_0 could be some length characterizing the obstacle (which is probably close to the energy injection scale we will discuss below). Alternatively, if turbulent structures are formed, U_0 could be the root-mean-square of the velocity variation over scale L_0 .

Dividing the Navier-Stokes equation by U_0^2/L_0 , we get

$$[\partial_{\tilde{t}}\tilde{\boldsymbol{U}} + (\tilde{\boldsymbol{U}} \cdot \tilde{\nabla})\tilde{\boldsymbol{U}}] = -\tilde{\nabla}\tilde{P} + Re^{-1}\tilde{\nabla}^{2}\tilde{\boldsymbol{U}} + \tilde{\boldsymbol{f}}, \quad Re = \frac{L_{0}U_{0}}{\nu} \sim \frac{|(\boldsymbol{U} \cdot \nabla)\boldsymbol{U}|}{|\nu\nabla^{2}\boldsymbol{U}|}, \quad (1.3)$$

where we have defined the dimensionless quantities $\tilde{\boldsymbol{U}} = \boldsymbol{U}/U_0$, $\tilde{P} = P/(\rho U_0^2)$, $\tilde{\boldsymbol{f}} = \boldsymbol{f} L_0/U_0^2$, $\tilde{\nabla} = L_0 \nabla$, and $\tilde{t} = t U_0/L_0$. We have also introduced the Reynolds number Re, which is an estimate of the strength of the nonlinear term relative to the viscous term. When $Re \ll 1$, viscous effects are strong and small perturbations in the fluid tend to be smoothed out,

leading to a very ordered flow that respects the symmetries of the Navier-Stokes equation and the boundary conditions (e.g., reflection symmetries, space- and time- translational symmetries). This is called laminar flow.

When $Re \gg 1$, viscous effects are weak and the nonlinear term dominates, leading to instabilities where small perturbations in the fluid can grow exponentially. This results in the formation of chaotic structures with a much faster dynamics than the large-scale flow. A great illustration of this transition from laminar to chaotic and, eventually, to fully turbulent flow as the Reynolds number increases can be found in the figures of the first chapter of Frisch (1995), where it can be seen how the symmetries displayed by laminar flow are broken one by one as Re grows.

Figure 1.10 in Frisch (1995) shows the turbulent wake behind two cylinders with Re = 1800. Careful visual inspection of turbulent flows like this one reveals the presence of coherent structures, or eddies, across a wide range of scales. Other features of the flow are the appearance of statistical homogeneity and, in the frame of reference that eliminates the mean (i.e., the large scale) flow, isotropy. By this we mean the following: it feels that, far from boundaries, the longitudinal structure function defined by Equation (1.2) should be the same on every point and for every direction ℓ/ℓ , so it should not depend on r or on the direction of ℓ (but it may depend on ℓ). Moreover, experimental measurements of the velocity in turbulent flows at a fixed point, over periods that start at different times, reveal that the histogram of the velocity is always the same (e.g., see Chapter 3 of Frisch (1995)), so we may drop the dependence of S_p^{\parallel} on \mathcal{T} . These are symmetries of the Navier-Stokes equation, which, after being broken by the formation of complex structures in the flow, are recovered (far from the boundaries) in this statistical sense when $Re > 10^3$. This restoration of the symmetries at high Re (formally, at $Re \to \infty$) is the defining characteristic of fully developed turbulence. From now on we will only focus on fully developed turbulence, so we will postulate that $S_p^{\parallel}(\boldsymbol{r},\boldsymbol{\ell},\mathcal{T}) = S_p^{\parallel}(\ell).$

Another symmetry of the Navier-Stokes equation that emerges when $\nu \to 0$ is that of scale

invariance. Thus, in the case of fully developed turbulence, we may postulate a hierarchy of self-similar eddies until reaching the scale where viscous dissipation becomes important (this will be better understood in later paragraphs). Mathematically, $S_p^{\parallel}(\Lambda \ell) = \Lambda^b S_p^{\parallel}(\ell)$.

Let us now describe qualitatively the dynamics of turbulence. Our picture will be based on the work of Richardson and Kolmogorov (Richardson, 1922; Kolmogorov, 1941a,b). The viscosity ν of the fluid sets a dissipation scale ℓ_d . Let us say that a force represented by f in the Navier-Stokes equation injects energy into the fluid at some scale $\ell_0 \gg \ell_d$. This can be, for example, a spoon stirring the fluid or an incoming flow hitting an obstacle, like the cylinders in Figure 1.10 of Frisch (1995)⁴. The energy should dissipate due to the presence of the viscous term in the Navier-Stokes equation, but the wide separation between the energy injection and dissipation scales results in the energy cascading through the formation of self-similar eddies spanning the full range of scales from injection to dissipation⁵, where energy flows from one scale into the next by the nonlinear interaction between eddies of similar size, given by the nonlinear term in the Navier-Stokes equation. This nonlinear interaction is said to be scale-local: only eddies of similar size can exchange energy efficiently. We can understand this with the following phenomenological argument. Let us try to visualize the interaction between two eddies whose respective sizes differ by more than an order of magnitude. The smaller eddy will perceive the larger one as a large-scale flow and is only passively advected by it, suffering no distortion (we can even eliminate this large-scale flow altogether with a simple Galilean boost). On the other hand, the small eddy cannot significantly affect the much larger one by itself, rather, multiple small eddies would have to act in coordination to distort the larger one.

If the rate of energy injection is constant, we can propose the existence of a steady state where the *mean* energy dissipation rate per unit mass, ε , equals the *mean* energy injection

³The property of self-similarity is not actually true, as we will briefly discuss later.

⁴Note that in the frame of reference where the mean flow is zero it looks like the obstacle is stirring the fluid.

⁵This cascade continues even into the dissipation range, although the eddies can no longer be postulated to be self-similar. In fact, the self-similarity breaks even before reaching the dissipation scale.

rate per unit mass. At scales ℓ satisfying $\ell_d \ll \ell \ll \ell_0$ (the so-called *inertial range*), there is neither energy injection nor dissipation, just a constant energy flux between scales as described above.

Let us now derive a formula for the longitudinal structure function of order p. We can follow Kolmogorov and postulate that the statistical properties of fully developed turbulence in the inertial range depend only on ℓ and ε . Then, dimensional analysis gives

$$S_p^{\parallel}(\ell) = C_p \varepsilon^{p/3} \ell^{p/3}, \tag{1.4}$$

where the dimensionless constants C_p were postulated to be universal (i.e., independent of the large scale mechanism that generates the turbulence) by Kolmogorov. This is the so-called K41 theory.

For p = 2 and p = 3 we get, respectively

$$S_2^{\parallel}(\ell) = C_2 \varepsilon^{2/3} \ell^{2/3}, \quad S_3^{\parallel}(\ell) = C_3 \varepsilon \ell.$$
 (1.5)

The first formula above is the famous two-thirds law. The second formula above can be derived rigorously (see Frisch (1995), Chapter 6) for homogeneous isotropic turbulence (under the additional assumption that the rate of energy dissipation satisfies $\varepsilon > 0$ when $\nu \to 0$), leading to the very important four-fifths law

$$S_3^{\parallel}(\ell) = -\frac{4}{5}\varepsilon\ell. \tag{1.6}$$

which is exact so long as the premises involved in its derivation hold true.

The universality of the coefficients C_p for $p \neq 3$ has been criticized by Lev Landau, but a better systematic derivation of (1.4) based on the four-fifths law and the self-similarity hypothesis leads to the same result without assuming universality (see Frisch, 1995, Chapter 6).

We will now re-derive the two-thirds law using a more hand-wavy argument reminiscent of those we will use in Chapters 2 and 3. Let us break up the range of scales between energy injection and dissipation into a discrete sequence of eddies of scales ℓ_1 through ℓ_N , satisfying $\ell_0 > \ell_1 > ... > \ell_N > \ell_d$, where $\ell_n = a^n \ell_0$, with $0 < a \lesssim 1$ (a is often chosen to be 0.5, but the exact number does not matter). The locality of the interaction implies that energy can only be transferred between two neighboring scales, say ℓ_n and ℓ_{n+1} . For an eddy of scale ℓ_n , the relative motion of two points on opposite sides can be characterized by velocity $\delta U_{\ell_n} \sim \sqrt{\langle (\delta \boldsymbol{U} \cdot \boldsymbol{\ell}_n/\ell_n)^2 \rangle}$. During time $\tau_{\ell_n} \sim \ell_n/\delta U_{\ell_n}$ (called turnover time) the eddy suffers a distortion comparable to its size, so this must be the energy transfer time.

In the steady state, the rate of energy dissipation per unit mass, ε , must equal the energy flux across scales, implying $\varepsilon \sim \delta U_{\ell_n}^2/\tau_{\ell_n} \sim \delta U_{\ell_n}^3/\ell_n$, so we recover the two-thirds law

$$\delta U_{\ell_n}^2 \sim (\varepsilon \ell_n)^{2/3}. \tag{1.7}$$

For completeness, we mention that by equating the viscous diffusion time $\tau_d \sim \ell^2/\nu$ to the cascade time $\tau_\ell \sim \ell/\delta U_\ell \sim (\ell^2/\varepsilon)^{1/3}$ we can obtain an estimate of the dissipation scale, $\ell_d \sim (\nu^3/\varepsilon)^{1/4}$. Experimental evidence shows that viscosity becomes important at scales about 30 times larger than this estimate.

Both the two-thirds and four-fifths laws match empirical observations rather well over a wide range of scales. However, deviations from observations become increasingly evident with growing p, showing that the hypothesis of self-similarity in the inertial range is, in fact, false, as eddies become more sparse towards smaller scales. This takes us to the concept of intermittency, but in this thesis, we will not present the existing plethora of different models of intermittency. Instead, we will introduce the relevant ideas as we need them.

We close this section with another very important result. A simple way to visualize the distribution of energy throughout scales is to look at the one-dimensional energy spectrum, E(k), where k is the magnitude of the wave vector. For an isotropic 3-dimensional fluid we

would define

$$E(k) = \frac{1}{2} \int_0^{2\pi} \int_0^{\pi} |\mathbf{U}_k|^2 k^2 \sin\theta d\theta d\phi, \qquad (1.8)$$

where U_k is the 3D Fourier transform of the velocity field U(x) at a given time.⁶

It can be proven that the energy spectrum and the second-order structure function are related in the following way (see chapter 4 of Frisch (1995))

$$S_2(\ell) \propto \ell^{\chi} \iff E(k) \propto k^{-(\chi+1)}, \quad 0 < \chi < 2.$$
 (1.9)

For the two-thirds law, this gives the famous Kolmogorov spectrum, $E(k) \propto k^{-5/3}$.

1.3 Plasma turbulence

The main topic of this dissertation is turbulence in weakly collisional plasmas with an externally imposed magnetic field that we will call guide field. This type of plasma environment is typical in space physics and astrophysics, where the guide field is imposed by a planet or a star. Another reason for the importance of magnetized plasma turbulence stems from the fact that, while there is always a frame of reference that eliminates the mean flow, there is no frame of reference that eliminates the magnetic field.⁷ This means that for a given magnetic eddy, a much larger one will look like a guide field. The presence of a guide field suggests that turbulent structures may be anisotropic, with length scale ℓ along the local magnetic field and a different length scale λ in the field-perpendicular direction.

Despite this important difference, the general mental picture of plasma turbulence is similar to the hydrodynamic case: energy is injected at some scale λ_0 and cascades to a

⁶In experiments and observations one generally has a measurement of the velocity as a function of time, rather than a velocity field for fixed time. However, the Fourier spectrum of this time signal given in terms of frequency ω can be reinterpreted as a spectrum in terms of the wavenumber k by use of the Taylor hypothesis, as we will discuss briefly in section 2.1.

⁷This is only true if the electric field is weaker than the magnetic field, as is the case in all the plasmas of interest.

much smaller dissipation scale λ_d , with the flux through scales mediated by the nonlinear interaction between coherent structures. However, this problem is notoriously more difficult. This is not only due to the formation of turbulent structures in the electric and magnetic fields, but because of the wide variety of turbulent regimes that are possible in a weakly collisional plasma. The weak collisionality pushes the dissipation scale below the plasma microscales (e.g., ion inertial d_i , ion gyro-scale ρ_i , ion-acoustic scale ρ_s), opening up a new range of scales for turbulent fluctuations. Thus, we can distinguish between the inertial range, $\lambda_0 \gg \lambda \gg d_i$, ρ_i , ρ_s , where the plasma can be approximately described as a single, magnetized charged fluid (magnetohydrodynamics, or MHD), and the sub-ion or kinetic range, $\lambda \ll d_i$, ρ_i , ρ_s , where kinetic physics that can be neglected at the MHD scale becomes important and the plasma can no longer be treated as a single fluid.

Let us review some important phenomenology of collisionless, strongly magnetized, non-relativistic plasma turbulence. Our discussion will be brief but there is no shortage of reviews discussing plasma turbulence in great detail (e.g., Biskamp, 2003; Bruno and Carbone, 2013; Tobias et al., 2013; Schekochihin, 2022). Let us say that energy is injected at some scale $\lambda_0 \gg \lambda \gg d_i, \rho_i, \rho_s$ and cascades through the inertial range, eventually reaching the sub-ion scale. Our dynamical equations for the inertial range will be those of reduced MHD, which in terms of the Elsässer fields \mathbf{Z}_{\perp}^{\pm} are (e.g., Oughton et al., 2017)

$$\partial_{t} \mathbf{Z}^{\pm} \mp v_{A} \nabla_{\parallel} \mathbf{Z}_{\perp}^{\pm} + \mathbf{Z}_{\perp}^{\mp} \cdot \nabla_{\perp} \mathbf{Z}_{\perp}^{\pm} =$$

$$-\nabla_{\perp} P + \frac{1}{2} (\eta + \nu) \nabla_{\perp}^{2} \mathbf{Z}_{\perp}^{\pm} + \frac{1}{2} (\eta - \nu) \nabla_{\perp}^{2} \mathbf{Z}_{\perp}^{\mp} + \mathbf{f}^{\pm},$$

$$\mathbf{Z}_{\perp}^{\pm} = \mathbf{U}_{\perp} \pm \mathbf{B}_{\perp}, \quad v_{A} = B_{0} / \sqrt{4\pi\rho}, \quad \nabla \cdot \mathbf{Z}^{\pm} = 0,$$

$$(1.10)$$

where U_{\perp} and B_{\perp} are the bulk velocity and magnetic fluctuations, respectively, v_A is the Alfvén speed, ρ the plasma density, B_0 is the guide field, and P is the total pressure (plasma plus magnetic). In the inertial range, the terms with the viscosity ν and the resistivity η , as well as the stirring force f^{\pm} , can be neglected. In the absence of injection and dissipation,

these equations conserve the Elsässer energies, $\langle |Z^{\pm}|^2 \rangle$.

The solutions to these equations are nondispersive Alfvén wave packets propagating either along the direction of the guide field (\mathbf{Z}^-) or opposite to it (\mathbf{Z}^+) . From the nonlinear term, we infer that only counter-propagating wave packets can interact. This interaction between counter-propagating Alfvén wave packets will give rise to the energy cascade in the inertial range.

The dynamics in the field-parallel direction, given by the linear term in Equation (1.10), has characteristic time $\tau_A \sim \ell/v_A$. The field-perpendicular dynamics, given by the nonlinear term, has characteristic time $\tau_{\rm nl}^{\pm} \sim \lambda/\delta Z_{\lambda}^{\mp}$, with $\delta Z_{\lambda}^{\pm} = \sqrt{\langle |\boldsymbol{Z}^{\pm}(\boldsymbol{x}+\boldsymbol{\lambda},t)-\boldsymbol{Z}^{\pm}(\boldsymbol{x},t)|^2\rangle}$. Three possibilities may be contemplated: $\tau_{\rm nl} \gg \tau_A$, $\tau_{\rm nl} \ll \tau_A$, and $\tau_{\rm nl} \sim \tau_A$. The first of these corresponds to the regime known as weak turbulence, where the linear term dominates and significantly deforming a wave packet takes multiple collisions. All we will say here about this case is that the turbulent cascade is only in the field-perpendicular direction and eventually reaches the regime of strong turbulence, where $\tau_{\rm nl} \sim \tau_A$. The reader who would like to know more about this regime may check the reviews cited above.

Regarding the case $\tau_{\rm nl} \ll \tau_A$, multiplying by v_A we obtain $v_A \tau_{\rm nl} \ll \ell$. This means that in the time of the energy cascade information cannot travel across the whole length ℓ of the turbulent structure, so it cannot stay coherent for long. This only leaves us with the so-called critical balance condition, $\tau_{\rm nl} \sim \tau_A$, where the linear and nonlinear terms in Equation (1.10) (in the range where energy injection and dissipation are negligible) are of the same order. This defines the regime known as strong turbulence.

From now on we will assume balanced turbulence, $\delta Z^+ \sim \delta Z^- \sim \delta U \sim \delta B$, so we will drop the \pm signs from the fields.⁸

Let us derive the scaling of the field-parallel cascade. If the mean injection and, assuming a steady state, dissipation rate per unit mass of the Elsässer energies is ε , we must have

⁸This rules out important turbulent systems that are imbalanced, like the solar wind. However, the point of this short review is just to expose the readers to the basics of plasma turbulence phenomenology and to aid them in understanding the meaning and importance of the turbulent regimes to be discussed in Chapters 2 and 3.

 $\varepsilon \sim \delta Z_\ell^2/\tau_A$, where δZ_ℓ represents a field variation along the *local* magnetic field.⁹ Using $\tau_A \sim \ell/v_A$, we easily get the scaling $\delta Z_\ell \propto \ell^{1/2}$ or $E(k_{\parallel}) \propto k_{\parallel}^{-2}$. This is a very robust scaling, as it makes no assumptions about the field-perpendicular cascade.

Let us repeat the exercise for the field-perpendicular cascade. Now we have $\varepsilon \sim \delta Z_{\lambda}^2/\tau_{\rm nl}$ and $\tau_{\rm nl} \sim \lambda/\delta Z_{\lambda}$. This gives $\delta Z_{\lambda} \propto \lambda^{1/3}$ or $E(k_{\perp}) \propto k_{\perp}^{-5/3}$. Using the critical balance condition, we also find the anisotropy of the turbulent fluctuations, $\ell \propto \lambda^{2/3}$. The results we just derived are the famous Goldreich-Sridhar 1995 (GS95) turbulence phenomenology (Goldreich and Sridhar, 1995). Interestingly, multiple numerical simulations have shown a field-perpendicular spectrum closer to $k_{\perp}^{-3/2}$ rather than $k_{\perp}^{-5/3}$ (e.g., Maron and Goldreich, 2001; Müller et al., 2003; Müller and Grappin, 2005; Mason et al., 2006, 2008; Perez and Boldyrev, 2008).

The flattening of the energy spectrum compared to GS95 suggests a weakening of the nonlinear interaction towards increasingly small λ . A possible explanation is the theory of dynamic alignment proposed in Boldyrev (2005, 2006); Perez et al. (2012), which states that magnetic and bulk velocity fluctuations tend to align the direction of their polarization in the field-perpendicular plane, resulting in a field-perpendicular anisotropy of the turbulent fluctuations defined by the alignment angle, $\theta_{\lambda} \sim \lambda/\xi \ll 1$. This reduces the nonlinear interaction by a factor θ_{λ} and increases the nonlinear time, $\tau_{\rm nl} \sim \xi/\delta Z_{\lambda} \sim \lambda/(\theta_{\lambda}\delta Z_{\lambda})$. Numerical observations show $\theta_{\lambda} \propto \lambda^{1/4}$. This gives scalings $\delta Z_{\lambda} \propto \lambda^{1/4}$, $E(k_{\perp}) \propto k_{\perp}^{-3/2}$, and $\ell \propto \lambda^{1/2}$.

A lot has been written regarding why the scaling of the alignment angle should be $\lambda^{1/4}$, but we will just refer the reader to Boldyrev (2005, 2006); Perez et al. (2012), as well as the reviews cited above and the references therein.

So much for the inertial range. As the energy keeps flowing to smaller scales, it eventually reaches the ion scales and a steepening of the spectrum is observed, with the scaling approaching $k^{-2.8}$ down to electron scales (e.g., Alexandrova et al., 2009; Kiyani et al., 2009; Chen et al., 2010, 2012; Sahraoui et al., 2013a; Chen and Boldyrev, 2017). It seems reasonable

 $^{^9}$ For a good discussion of why it has to be the local magnetic field see, for example, Schekochihin (2022). See also Equation (2.6).

to suggest that this is due to the transition from nondispersive Alfvén wave packets in the inertial range to dispersive ones in the sub-ion scale, the so-called kinetic Alfvén turbulence or simply KAW turbulence (after kinetic Alfvén waves). Kinetic Alfvén waves can be obtained as the linear solutions of dynamical equations derived from a two-fluid model; we will not discuss the derivation here, but a similar procedure can be found in Section 3.3. This leads to an energy spectrum that scales as $k_{\perp}^{-7/3}$ (e.g., Cho and Lazarian, 2004; Schekochihin et al., 2009), which is too flat. In Boldyrev and Perez (2012), the authors derive a $k_{\perp}^{-8/3}$ scaling, quite close to observations, by introducing intermittency to the KAW model (concretely, they propose that magnetic and density fluctuations tend to organize into intermittent two-dimensional structures). Interestingly, the KAW model does not predict the correct location of the spectral break observed in regions of the solar wind with low ion beta (the model predicts the transition to KAW turbulence at the ion acoustic scale but observations show the ion inertial scale). For a discussion of this problem and possible explanations of the spectral steepening alternative to KAW turbulence (e.g., Landau damping), see, for example, Chen et al. (2014); Boldyrev et al. (2015).

What comes next? In plasmas with low electron beta, $\beta_e = (\rho_e/d_e)^2 \ll 1$, the electron gyro-scale ρ_e and inertial scale d_e are well separated and the turbulent cascade can continue into the sub- d_e range down to ρ_e . This turbulent regime will be the topic of Chapter 2. In particular, Section 2.1 will be dedicated to reviewing the phenomenological derivation and some of the observational and numerical evidence of *inertial* Kinetic Alfvén turbulence (Chen and Boldyrev, 2017; Roytershteyn et al., 2019).

And what about turbulence in relativistic plasmas? This is the topic of Chapter 3. In particular, Section 3.3 is dedicated to the numerical characterization and phenomenological modeling of the energy spectrum in both the inertial and kinetic ranges (Vega et al., 2022a, 2024b).

We hope the discussion in this section has helped the reader understand where our work fits into the vast space of plasma turbulence. Let us now summarize the steps we followed to derive the scaling laws of hydrodynamic turbulence in the previous section and of MHD turbulence in this section. This is the approach we will follow in Chapters 2 and 3 as well. The general method is:

- Find approximate dynamical equations for the turbulent fluctuations (e.g., reduced MHD).
- Find the linear modes (e.g., Alfvén waves) and quantities conserved by the dynamical equations in the absence of injection and dissipation (e.g., energy).
- Assume that the conserved quantity cascades with constant flux ε to smaller scales due to the scale-local nonlinear interaction between wave packets of the modes found in the previous step.
- Find an estimate of ε . This will consist of a formula of the form $\varepsilon \sim w_{\lambda}/\tau_{\lambda}$, where w_{λ} is the amount of the conserved quantity in structures of scale λ that flows to smaller scales over cascade time τ_{λ} . w_{λ} and τ_{λ} are to be estimated in terms of the turbulent fluctuations and the scale λ .
- The formula for ε may depend on the turbulent fluctuations of more than one field. The linear solutions to the dynamical equations can tell us how the amplitudes of different fields are related to each other. Alternatively, one may guess how they are related from simple dimensional analysis. This allows us to write the formula for ε in terms of the fluctuations of a single field.
- From the formula for ε found in the previous step, find the scaling of the turbulent fluctuation, $X_{\lambda} \propto \lambda^{\chi}$, where X is the turbulent field (e.g., magnetic, bulk kinetic, electric). From this scaling, we can obtain the energy spectrum of X: $E(k_{\perp}) \propto k_{\perp}^{-(2\chi+1)}$.
- With the critical balance condition we can obtain the anisotropy of the fluctuations $\ell \propto \lambda^{\alpha}$.

One last comment before moving on to the next section. In our discussion of dynamic alignment, we hinted at the formation of increasingly thin magnetic structures towards smaller scales in the guide-field-perpendicular plane. By Ampère law, this would result in the formation of increasingly thin, field-parallel current sheets. At some aspect-ratio these structures may become unstable and break, leading to magnetic reconnection (e.g., Zhdankin et al., 2013; Loureiro and Boldyrev, 2017; Mallet et al., 2017). If the energy cascade can continue into the sub-ion range, the thin, often electron-scale structures that form may also break and lead to the so-called electron-only magnetic reconnection (e.g., Phan et al., 2018; Boldyrev and Loureiro, 2019; Vega et al., 2020, 2023b). Magnetic reconnection is believed to play a pivotal role in collisionless dissipation and nonthermal particle acceleration. We will discuss collisionless dissipation and magnetic reconnection in the next two sections, respectively.

1.4 Energy dissipation in collisionless plasmas

In the last section, we described how, in a weakly collisional turbulent plasma, energy cascades down from an injection scale and into the sub-ion range. Even in such weakly collisional environments as the solar wind and corona, significant plasma heating is observed (e.g., Matthaeus and Velli, 2011; Bruno and Carbone, 2013; Howes, 2015), so there is great interest in understanding how the cascade of electromagnetic and bulk kinetic energy eventually makes its way into the microscopic degrees of freedom of the plasma, even in the case of vanishingly small viscosity and resistivity. The electric work, $E \cdot J$, is often used as a proxy for collisionless dissipation in weakly collisional plasmas (e.g., Wan et al., 2012, 2015, 2016), but this gives the total energy exchange between the electromagnetic energy density and the plasma energy (including bulk kinetic). The energy exchange with the bulk motion can be partially removed from the electric work by computing it in the comoving frame of one particle species (e.g., the electrons), but it cannot be fully eliminated.

An alternative measure of collisionless energy dissipation is obtained in Yang et al. (2017); below we follow their derivation. Starting from the nonrelativistic Vlasov equation for the one-particle distribution function of species s (ions or electrons), $f_s(\boldsymbol{x}, \boldsymbol{v}, t)$,

$$\frac{\partial f_s}{\partial t} + \boldsymbol{v} \cdot \boldsymbol{\nabla} f_s + \frac{q_s}{m_s} \left(\boldsymbol{E} + \frac{\boldsymbol{v}}{c} \times \boldsymbol{B} \right) \cdot \frac{\partial f_s}{\partial \boldsymbol{v}} = 0, \tag{1.11}$$

and taking the zeroth, first, and second moments we get:

$$\partial_t(m_s n_s) + \nabla \cdot (m_s n_s U_s) = 0, \tag{1.12a}$$

$$\partial_t(m_s n_s \boldsymbol{U}_s) + \boldsymbol{\nabla} \cdot (n_s \boldsymbol{U}_s \boldsymbol{U}_s) = -\boldsymbol{\nabla} \cdot \boldsymbol{P}_s + n_s q_s \left(\boldsymbol{E} + \frac{\boldsymbol{U}_s}{c} \times \boldsymbol{B} \right), \tag{1.12b}$$

$$\partial_t \mathcal{E}_s + \nabla \cdot (\mathcal{E}_s \mathbf{U}_s) = -\nabla \cdot (\mathbf{P}_s \cdot \mathbf{U}_s) - \nabla \cdot \mathbf{h}_s + n_s q_s \mathbf{E} \cdot \mathbf{U}_s,$$
 (1.12c)

where m_s is the particle mass, n_s is the particle density, U_s is the bulk velocity, P_s is the pressure tensor, q_s is the electric charge, E and B are the electric and magnetic field, respectively, \mathcal{E}_s is the total (bulk plus thermal) kinetic energy density, and h_s is the heat flux vector.

The pressure tensor, kinetic energy density, and heat flux are defined in terms of the one-particle distribution function f_s :

$$\mathbf{P}_s = m_s \int (\mathbf{v} - \mathbf{U}_s)(\mathbf{v} - \mathbf{U}_s) f_s(\mathbf{x}, \mathbf{v}, t) d^3 v, \qquad (1.13a)$$

$$\mathcal{E}_s = \frac{m_s}{2} \int \mathbf{v}^2 f_s(\mathbf{x}, \mathbf{v}, t) d^3 v, \qquad (1.13b)$$

$$\boldsymbol{h}_s = \frac{m_s}{2} \int (\boldsymbol{v} - \boldsymbol{U}_s)^2 (\boldsymbol{v} - \boldsymbol{U}_s) f_s(\boldsymbol{x}, \boldsymbol{v}, t) d^3 v.$$
 (1.13c)

The kinetic energy density can be separated into the bulk or fluid kinetic energy $\mathcal{E}_s^{\mathrm{f}}$ and the thermal or internal energy $\mathcal{E}_s^{\mathrm{th}}$, which is the kinetic energy of the particles measured in

the comoving frame:

$$\mathcal{E}_s^{\mathrm{f}} = \frac{1}{2} m_s n_s \mathbf{U}_s^2, \quad \mathcal{E}_s^{\mathrm{th}} = \frac{m_s}{2} \int (\mathbf{v} - \mathbf{U}_s)^2 f_s(\mathbf{x}, \mathbf{v}, t) d^3 v, \tag{1.14a}$$

$$\mathcal{E}_s = \mathcal{E}_s^{\mathrm{f}} + \mathcal{E}_s^{\mathrm{th}}. \tag{1.14b}$$

If we take the dot product of equation (1.12b) with U_s and use $\nabla \cdot (P_s \cdot U_s) = U_s \cdot (\nabla \cdot P_s) + (P_s \cdot \nabla) \cdot U_s$, we get

$$\partial_t \mathcal{E}_s^f + \nabla \cdot (\mathcal{E}_s^f U_s) = -\nabla \cdot (P_s \cdot U_s) + (P_s \cdot \nabla) \cdot U_s + n_s q_s E \cdot U_s. \tag{1.15}$$

We note that the pressure-strain interaction, $-(\mathbf{P}_s \cdot \nabla) \cdot \mathbf{U}_s$, has just appeared. Subtracting the equation above from (1.13c), we get

$$\partial_s \mathcal{E}_s^{\text{th}} + \nabla \cdot (\mathcal{E}_s^{\text{th}} U_s) = -(P_s \cdot \nabla) \cdot U_s - \nabla \cdot h_s. \tag{1.16}$$

Taking the time derivative of the electromagnetic energy density $\mathcal{E}^{m} = (\mathbf{B}^{2} + \mathbf{E}^{2})/(8\pi)$ and using Faraday's law and Maxwell-Ampère's law, we obtain the well-known equation

$$\partial_t \mathcal{E}^{\mathrm{m}} + \frac{c}{4\pi} \nabla \cdot (\boldsymbol{E} \times \boldsymbol{B}) = -\boldsymbol{E} \cdot \boldsymbol{J}, \tag{1.17}$$

where $\boldsymbol{J} = \sum_{s} n_{s} q_{s} \boldsymbol{U}_{s}$ is the current density.

If we now average equations (1.15), (1.16), and (1.17) over the entire domain of a numerical simulation with periodic boundary conditions (as is often the case with simulations of plasma turbulence), the terms of the form $\nabla \cdot (...)$ vanish, so we obtain

$$\partial_t \langle \mathcal{E}_s^{\mathrm{f}} \rangle = \langle (\boldsymbol{P}_s \cdot \boldsymbol{\nabla}) \cdot \boldsymbol{U}_s \rangle + \langle n_s q_s \boldsymbol{E} \cdot \boldsymbol{U}_s \rangle, \tag{1.18a}$$

$$\partial_t \langle \mathcal{E}_s^{\text{th}} \rangle = -\langle (\boldsymbol{P}_s \cdot \boldsymbol{\nabla}) \cdot \boldsymbol{U}_s \rangle,$$
 (1.18b)

$$\partial_t \langle \mathcal{E}^{\mathrm{m}} \rangle = -\langle \boldsymbol{E} \cdot \boldsymbol{J} \rangle.$$
 (1.18c)

A picture of the energy exchange between particles and fields emerges from the three equations we just derived. The average electric work, $\langle n_s q_s U_s \cdot E \rangle$, mediates the energy exchange between the electromagnetic field and the bulk fluid motion, while it is the average pressure-strain interaction, $-\langle (P_s \cdot \nabla) \cdot U_s \rangle$, that is responsible for the rate of change of the internal energy by mediating its exchange with the fluid energy. Furthermore, the numerical analysis presented in Yang et al. (2017) suggests that the energy exchange between the electromagnetic field and the bulk flows takes place at large scales, with the bulk energy then cascading towards smaller scales and eventually some of it transforming into internal energy through the pressure-strain interaction. This transfer of energy toward the microscopic degrees of freedom of the plasma would result in entropy production if collisions were present, possibly even if collisionality was weak (e.g., Eyink, 2018a). Thus, this should be our measure of energy dissipation. To make the case even stronger, in Yang et al. (2022) the authors show that the pressure-strain interaction is the most appropriate estimate of dissipation by explicit comparison against other proxies commonly used, including the electric work.

Several numerical studies of different regimes of plasma turbulence have used the electric work as a proxy of energy dissipation and found it to be strongly intermittent and concentrated on intense current sheets (e.g., Wan et al., 2012, 2015, 2016; Zhdankin et al., 2013). In Section 2.3, we use the pressure-strain interaction to address the question of the intermittency of energy dissipation in a turbulent low electron beta environment (Vega et al., 2023b).

In this section, we discussed collisionless energy dissipation in general terms without looking into specific physical mechanisms that result in plasma heating and particle acceleration. In the next section, we will discuss a very important mechanism of magnetic to plasma energy conversion known as magnetic reconnection.

1.5 Magnetic reconnection

In this section, we present a short, qualitative description of magnetic reconnection, focusing on those aspects of the phenomenon that are relevant for later chapters. For detailed reviews see, for example, Zweibel and Yamada (2009); Zweibel and Yamada (2016); Guo et al. (2023b).

Magnetic reconnection is a fundamental plasma physics process in which magnetic field lines break and reconnect, releasing magnetic energy into the plasma. It is widely believed to play a role in the heating of the solar corona (e.g., Parker, 1990; Klimchuk, 2006; Parnell and De Moortel, 2012) and nonthermal acceleration to ultrarelativistic energies seen in astrophysical sources like black hole accretion disks, pulsar magnetospheres, and pulsar winds (e.g., Guo et al., 2023b). It has also been observed to be spontaneously generated in MHD turbulence (e.g., Zhdankin et al., 2013) and sub-ion scale turbulence (e.g., Phan et al., 2018; Vega et al., 2020, 2023b), and was seen to play an important role in energy dissipation in these plasma environments.

For clarity, we show in Figure 1.1 a concrete example of magnetic reconnection that we found in one of the 2.5D particle-in-cell simulations of sub-ion plasma turbulence that we will present in Chapter 2. As we will explain below, the figure shows electron-only reconnection. However, we will first explain the classical, double-layer reconnection with ion coupling, so Figure 1.1 is just meant to be illustrative.

The magnetic topology of a typical 2D reconnection event can be clearly appreciated in this example, where the in-plane magnetic field lines are shown in black and the out-of-plane current density is shown in the colormap. In a general reconnection event, magnetic field lines pointing in opposite directions approach each other; in Figure 1.1 this is happening along the red arrows labeled "Inflow". At the MHD scale, magnetic field lines are frozen to the plasma, so they drag plasma particles into the reconnection site as they get closer, generating a plasma inflow. Once magnetic field lines are closer than the ion inertial scale, ion inertial becomes important, i.e., the field lines decouple from the ions. However, electrons remain frozen to the magnetic field lines until they are closer than the electron inertial scale. It is

within this thin, electron-scale layer, that magnetic field lines break and reconnect. When this happens, the accumulated magnetic tension is released in the form of plasma energy, as the outgoing field lines drag particles along the outflow, first recoupling to the electrons and, given enough space along the outflow (about 40 times the ion inertial scale, Sharma Pyakurel et al. (2019)), to the ions.

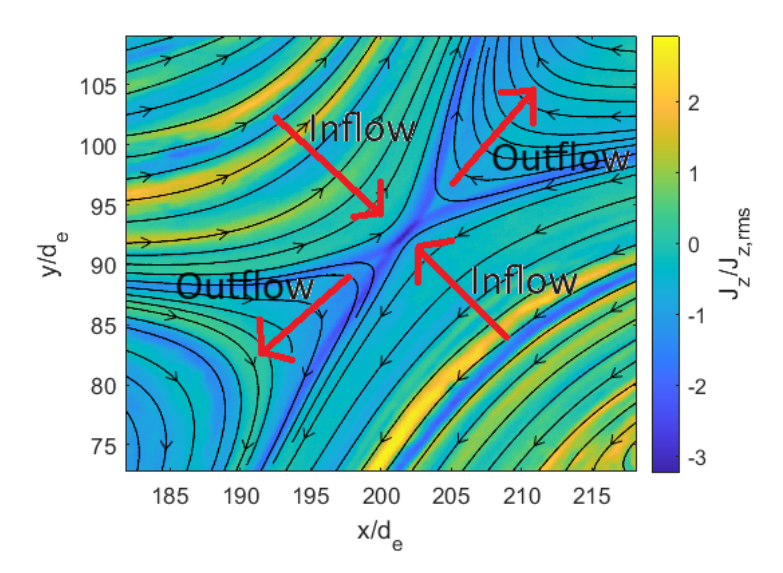


Figure 1.1: Example of electron-only magnetic reconnection site found in one of the 2.5D particle-in-cell simulations to be analyzed in Chapter 2. The color map shows the out-of-plane (and guide-field-parallel) current density, J_z , normalized to the root-mean-square out-of-plane current density computed over the whole simulation domain. The thin black lines represent the magnetic field lines. The large, red arrows exhibit the direction of the particle (electrons) inflow and outflow. On the axes, d_e refers to the electron inertial scale.

What we just described qualitatively in the previous paragraph is the classical two-fluid model of reconnection where an electron-scale diffusion layer is embedded into a thicker, ion-scale diffusion layer, and both electrons and ions move together at the exhaust at speeds close to the ion Alfvén speed computed with the in-plane magnetic field along the inflow, measured just outside the outer diffusion layer. However, as we mentioned before, this does not correspond to the example shown in Figure 1.1. The figure shows magnetic reconnection happening spontaneously in sub-ion scale turbulence, where the thin current layer is too short along the outflow for effective ion coupling. This is an example of electron-only magnetic

reconnection, similar to those observed in the magnetosheath by the Magnetospheric Multiscale (MMS) mission (Phan et al., 2018), where only Alfvénic electron jets are seen along the outflow (with the Alfvén velocity calculated with the in-plane magnetic field along the inflow, just outside the electron diffusion layer). We also note the small but intense out-of-plane (and guide-field-parallel) current sheet at the center, seen in dark blue, with a peak current of more than three times the root-mean-square value. This current sheet is less than $5d_e$ long and about $0.5d_e$ thick, with d_e the electron inertial scale. Alfvénic electron jets and a large out-of-plane current sheet are electron-only reconnection signatures that can be used to find these sites.

The topology of the magnetic field lines suggests another method to find reconnection candidates in 2.5D simulations of plasma turbulence: look for saddle points of the out-of-plane magnetic potential or X-points. This method is developed in detail in Section 2.2 and is complemented by the other reconnection signatures discussed here to identify electron-only reconnection sites spontaneously generated in a simulated 2.5D turbulent environment (Vega et al., 2020). We also look for reconnection in a 3D spectral simulation relying on signatures like Alfvénic electron jets and intense current sheets, and we analyze its role in energy dissipation (Vega et al., 2023b).

Magnetic reconnection spontaneously generated in relativistic plasma turbulence is known to play a fundamental role in turbulent particle acceleration (Comisso and Sironi, 2019). This will be discussed in more detail in the next section.

1.6 Relativistic plasma turbulence as a particle accelerator

In weakly collisional plasma turbulence, the interaction with turbulent fluctuations may remove some particles from the thermal population, creating a nonthermal tail in the particle energy probability density function (pdf). Indeed, nonthermal particle acceleration to ultrarelativistic energies has been observed in multiple simulations of relativistic plasma turbulence, with the particle energy pdf developing power-law tails (e.g., Zhdankin et al., 2017, 2019; Zhdankin, 2021; Comisso and Sironi, 2018, 2019; Wong et al., 2020; Nättilä and Beloborodov, 2021, 2022; Vega et al., 2022b, 2023a), or log-normal tails if the guide field is strong (e.g., Vega et al., 2024b,a). This makes relativistic plasma turbulence a promising acceleration candidate that may help explain the radiative signatures of nonthermal ultrarelativistic particles in astrophysical systems such as pulsar magnetospheres and winds (e.g., Bühler and Blandford, 2014), jets from active galactic nuclei (e.g., Begelman et al., 1984), and black hole accretion disks (e.g., Yuan and Narayan, 2014), complementing other known energization mechanisms like collisionless shocks (e.g., Blandford and Eichler, 1987; Marcowith et al., 2016) and magnetic reconnection (e.g., Uzdensky et al., 2011; Drake et al., 2013; Sironi and Spitkovsky, 2014; Sironi, 2022; French et al., 2023; Guo et al., 2020, 2023b), and also acting as a source that spontaneously generates intermittent structures like shocks and reconnection (e.g., Stone et al., 1998; Servidio et al., 2009; Eyink et al., 2013; Zhdankin et al., 2013; Comisso and Sironi, 2019; Vega et al., 2020, 2023b).

Numerical studies of particle acceleration in driven, moderately magnetized relativistic plasma turbulence (Zhdankin et al., 2017, 2018b) and decaying magnetically dominated plasma turbulence (Comisso and Sironi, 2018, 2019) have shown that the power-law tail developed in the particle energy pdf steepens with increasing system size, asymptotically reaching a system-size-independent value where the outer-scale of turbulence determines the high-energy cut-off of the distribution. Our numerical studies of relativistic plasma turbulence (Vega et al., 2022b,a, 2023a, 2024b,a, reproduced in Chapter 3 of this thesis) were done in this asymptotic limit, except for one small-box, strong-guide-field simulation used to study kinetic scale relativistic turbulence.

In simulations of decaying relativistic plasma turbulence, the slope is also seen to flatten

¹⁰By "magnetically dominated" we mean that the simulation was initialized with far more energy in the magnetic fluctuations than in the particles. It is observed that in such an initialization the plasma is quickly heated to a relativistic temperature (e.g., Comisso and Sironi, 2019; Vega et al., 2022b, 2023a), so we will often refer to magnetically dominated plasma turbulence as relativistic turbulence.

as the magnetization $\tilde{\sigma}_0 = \delta B_0^2/(4\pi\epsilon_0)$ increases while keeping $B_0/\delta B_0$ constant, where B_0 is the guide field, δB_0 is the initial root-mean-square magnetic fluctuation, and ϵ_0 is the initial enthalpy density, asymptotically converging to a fixed value for $\tilde{\sigma}_0 \gg 1$ (Comisso and Sironi, 2018, 2019). When $\tilde{\sigma}_0$ is kept constant and $B_0/\delta B_0$ is increased, the slope is seen to steepen until giving way to a log-normal distribution (Vega et al., 2022b, 2024b,a, and Chapter 3 here).

In Comisso and Sironi (2019), the authors identify two stages of turbulent particle energization where different mechanisms act on the particles: an initial injection phase in which a particle is quickly kicked out of the bulk population and into the relativistic tail of the distribution, and a second phase of stochastic acceleration where the particle continues to be energized as it interacts with turbulent fluctuations in the inertial range.

In the injection phase, particles are accelerated in reconnecting current sheets. Studies of relativistic plasma turbulence and relativistic reconnection show that, in simulations with guide field $B_0 \sim \delta B_0$, the main contribution to the energy injection comes from the nonideal electric field (Comisso and Sironi, 2019; Sironi, 2022; Guo et al., 2023a; French et al., 2023), while the ideal electric field dominates the energy injection when the guide field is weak (Guo et al., 2023a; French et al., 2023).

In the second stage, the energization resembles a diffusion process in energy space, with diffusion coefficient scaling as γ^2 , where γ is the particle Lorentz factor (Comisso and Sironi, 2019; Wong et al., 2020). Numerical suppression of the injection phase shows that the power-law tail in the particle energy pdf still develops but with a much smaller population of particles, showing that it is this second stage that is responsible for the development of the power-law. In contrast, the first stage supplies a population of particles with gyroradius large enough to interact efficiently with turbulent fluctuations in the inertial range (Comisso and Sironi, 2019; Vega et al., 2024a).

Although the acceleration process in relativistic plasma turbulence is not fully understood, recent analytical and numerical studies indicate that spontaneously generated turbulent

structures may indeed play an essential role in particle energization (e.g., Trotta et al., 2020; Ergun et al., 2020; Lemoine, 2021; Pezzi et al., 2022; Bresci et al., 2022; Vega et al., 2022b; Xu and Lazarian, 2023; Lemoine et al., 2023). In Section 3.4 we present our work showing how power-law tails may develop in the particle energy pdf if particles are accelerated stochastically in spontaneously generated magnetic traps until they escape by pitch angle scattering (Vega et al., 2022b), also noting that the high-energy tail of the particle energy pdf evolves into a log-normal when the guide field is strong compared to the initial magnetic fluctuations (Vega et al., 2024b,a). To understand this, we present our more recent work on acceleration, where we take a closer look at the actual acceleration mechanisms, viz., the electric field parallel to the magnetic field, curvature acceleration, and mirror acceleration, and we discuss how they depend on the properties of Alfvénic turbulence (Vega et al., 2024a).

We close Chapter 3 with our work on the observed intermittency in the spatial distribution of ultrarelativistic particles accelerated in decaying magnetically dominated plasma turbulence (Vega et al., 2023a).

2 PLASMA TURBULENCE IN ENVIRONMENTS WITH LOW

ELECTRON BETA

2.1 Inertial kinetic Alfvén turbulence

Let T_i and T_e be the ion and electron temperature, respectively. In plasma environments where the ions are much hotter than the electrons, $T_i \gg T_e$, and $\beta_i \sim 1$ (e.g., the magnetosheath (Wang et al., 2012; Chen and Boldyrev, 2017), the solar wind close to the solar corona (Shi et al., 2023)), the electron beta satisfies $\beta_e = (\rho_e/d_e)^2 \ll \beta_i = (\rho_i/d_i)^2 \sim 1$. This means that the electron gyroradius ρ_e and inertial scale d_e are well differentiated, so sub-ion scale turbulent fluctuations can cascade through the range of scales $\rho_i, d_i \gg \lambda \gg d_e$ and then continue into $d_e \gg \lambda \gg \rho_e$.

Measurements of the solar wind density and magnetic energy spectra between the ion and electron scales reveal anisotropic fluctuations elongated along the guide-field, $k_{\parallel} \ll k_{\perp}$ (Chen et al., 2010), and a $k^{-2.8}$ power-law behavior (e.g., Alexandrova et al., 2009; Kiyani et al., 2009; Chen et al., 2010, 2012; Sahraoui et al., 2013a), remarkably close to the $k_{\perp}^{-8/3}$ spectrum of kinetic Alfvén turbulence with intermittency corrections, which also predicts anisotropy $k_{\parallel} \propto k_{\perp}^{2/3}$ (Boldyrev and Perez, 2012). The frequency and polarization of the fluctuations are also seen to be consistent with a kinetic Alfvén cascade (Boldyrev et al., 2013; Chen et al., 2013b). All this strongly suggests a kinetic Alfvén turbulent cascade between the ion and electron scales.

Data collected by the Magnetospheric Multiscale (MMS) mission in regions of the magnetosheath with $\beta_e \ll \beta_i \sim 1$ revealed that the behavior of turbulence changes as it transitions into the range of scales $d_e \gg \lambda \gg \rho_e$ (e.g., increased magnetic compressibility, steeper magnetic energy spectrum), hinting at the existence of a new regime of plasma turbulence (Chen and Boldyrev, 2017). Observations are consistent with theoretical models based on new low-frequency plasma modes known as inertial kinetic Alfvén waves, or iKAW (Chen and Boldyrev, 2017; Passot et al., 2017, 2018). The existence of this regime was later confirmed in numerical simulations (e.g., Roytershteyn et al., 2019). In the remainder of this section, we will review the phenomenology and the observational and numerical evidence of iKAW turbulence.

A universal property of magnetized plasma turbulence is the emergence of intermittent magnetic structures, which manifests itself in the formation of current sheets (e.g., Karimabadi et al., 2013; Zhdankin et al., 2014; Papini et al., 2019). These coherent structures are known to play a pivotal role in the dissipation of energy in weakly collisional plasma turbulence (e.g., Wan et al., 2012, 2015, 2016; Karimabadi et al., 2013; Zhdankin et al., 2014; Camporeale et al., 2018). The availability of the sub- d_e range of scales to turbulent fluctuations should make plasmas with low electron beta a particularly fertile ground for the generation of electron-scale current sheets, and quantifying their contribution to energy dissipation is a question of considerable interest. The formation of electron-scale current sheets and their role in energy dissipation was the main topic of Vega et al. (2023b), and will be discussed in Sections 2.2 and 2.3.

Some electron-scale current sheets may be tearing unstable and undergo electron-only magnetic reconnection (Boldyrev and Loureiro, 2019), recently discovered in the magnetosphere (Phan et al., 2018). In electron-only reconnection, only Alfvénic electron jets are observed along the outflow, with ions not coupling to the electrons' motion due to the reconnecting current sheet being too short along the outflow (much shorter than the $\sim 40d_i$ necessary for effective ion coupling; see, for example, Sharma Pyakurel et al. (2019)). Electron-only reconnection was observed in a turbulent environment with properties consistent with kinetic scale turbulence (Stawarz et al., 2019), so one may ask whether it is a characteristic property of this turbulent regime, and what role it plays in energy dissipation. The first question was addressed in Vega et al. (2020) and the second in Vega et al. (2023b), and they will both be discussed in Section 2.2.

The dynamics of Alfvén modes

Here we derive a phenomenological model for the turbulence cascade in the range $d_e^{-1} \ll k_{\perp} \ll \rho_e^{-1}$ in a plasma environment with $\beta_e \ll \beta_i \sim 1$. First, we will justify the need for this calculation by showing that the dispersion relation of kinetic Alfvén waves breaks down when $k_{\perp}d_e \ll 1$. This dispersion relation is derived assuming an isotropic and Maxwellian plasma (i.e., the one-particle probability density function is a locally isotropic Maxwellian for ions and electrons), and frequency ω satisfying $\omega \ll k_{\parallel}v_{\rm th,e}$, where $v_{\rm th,e}$ is the electron thermal velocity (Schekochihin et al., 2009). One obtains

$$\omega^2 = \frac{k_{\parallel}^2 v_A^2 k_{\perp}^2 \rho_i^2}{\beta_i + 2/(1 + \beta_e/\beta_i)}.$$
 (2.1)

Using Equation 2.1 and the assumption $T_e/T_i \ll 1$ it can be shown that $\omega^2/(k_{\parallel}v_{\text{th},e})^2 \sim 1$ at scale

$$k_{\perp}^{2} d_{e}^{2} \sim (2 + \beta_{i})(\beta_{e}/\beta_{i}) < 1,$$
 (2.2)

which means that the assumption $\omega \ll k_{\parallel}v_{\mathrm{th},e}$ no longer holds for $d_e^{-1} \ll k_{\perp} \ll \rho_e^{-1}$, which is the range of scales we are interested in. Thus, we need to derive the dynamical equations of the modes with frequency $\omega > k_{\parallel}v_{\mathrm{th},e}$, implying that the electron inertia will be important.

We will assume strongly anisotropic fluctuations (i.e., $k_{\perp} \gg k_{\parallel}$), ordering k_{\parallel}/k_{\perp} , $\delta B/B_0 \sim \delta n/n_0$, $\omega/\Omega_e \ll 1$, and $k_{\parallel}v_{\rm th,e} \ll \omega \ll k_{\perp}v_{\rm th,i}$ (this excludes whistler modes, which have higher frequency). We will adopt an isotropic fluid model for electrons, so their dynamics will be dictated by the continuity equation

$$\frac{\partial n_e}{\partial t} + \nabla \cdot (n_e U_e) = 0, \tag{2.3}$$

and the momentum conservation equation

$$\frac{\partial \boldsymbol{U}_e}{\partial t} + (\boldsymbol{U}_e \cdot \boldsymbol{\nabla}) \boldsymbol{U}_e = -\frac{1}{m_e n_e} \boldsymbol{\nabla} P_e - \frac{e}{m_e} \left(\boldsymbol{E} + \frac{\boldsymbol{U}_e}{c} \times \boldsymbol{B} \right). \tag{2.4}$$

In the two equations above, n_e is the electron density, m_e is the electron mass, U_e is the electron fluid velocity, P_e is the electron pressure, and E and B are the electric and magnetic field, respectively.

There are too many variables for only two equations, but we can simplify this to a system of two equations for the density fluctuations and the field-perpendicular magnetic fluctuations.

Let us start by rewriting the continuity equation in terms of the field-parallel electron velocity, $U_{e,\parallel}$, and the field-perpendicular electron velocity, $U_{e,\perp}$,

$$\frac{\partial n_e}{\partial t} + \nabla_{\perp} \cdot (n_e U_{e,\perp}) + \nabla_{\parallel} (n_e U_{e,\parallel}) = 0, \tag{2.5}$$

where we have introduced the magnetic-field-perpendicular and -parallel differential operators ∇_{\perp} and ∇_{\parallel} , respectively. While $\delta B/B_0 \ll 1$ implies that the parallel component of the fields can be approximated by their z component, this is not the case for the ∇_{\parallel} operator. To understand this, let us write this operator in terms of ∂_z :

$$\nabla_{\parallel} = \frac{\boldsymbol{B}}{B} \cdot \boldsymbol{\nabla} = \partial_z + \frac{\delta \boldsymbol{B}_{\perp}}{B_0} \cdot \boldsymbol{\nabla}. \tag{2.6}$$

Since $k_{\parallel} \ll k_{\perp}$, the second term on the right-hand side above cannot be neglected.

Going back to the continuity equation (2.5), we can write the parallel electron velocity in terms of the field-parallel current density, $U_{e,\parallel} = -J_{\parallel}/(n_e e)$ (where we are assuming that electrons dominate in the current due to their much smaller inertia compared to the ions), and the current itself can be written in terms of the field-parallel component of the magnetic potential, A_{\parallel} , through Ampère's law (where we can neglect the displacement current for

being in the nonrelativistic regime):

$$\boldsymbol{J} = \frac{c}{4\pi} \boldsymbol{\nabla} \times \boldsymbol{B} = \frac{c}{4\pi} \boldsymbol{\nabla} \times (\boldsymbol{\nabla} \times \boldsymbol{A}) = -\frac{c}{4\pi} \nabla^2 \boldsymbol{A}, \tag{2.7}$$

where we used the Coulomb gauge, $\nabla \cdot \mathbf{A} = 0$. It is conventional to define the scalar function $\psi \equiv -A_z \approx -A_{\parallel}$, so $\delta \mathbf{B}_{\perp} = \hat{\mathbf{z}} \times \nabla \psi$. In terms of ψ , the parallel component of equation (2.7) is

$$J_{\parallel} = \frac{c}{4\pi} \nabla_{\perp}^2 \psi, \tag{2.8}$$

where we are neglecting $\nabla_{\parallel}^2 \psi$, as $k_{\perp}^2 \gg k_{\parallel}^2$. The parallel electron velocity is then

$$U_{e,\parallel} = -\frac{c}{4\pi n_e e} \nabla_{\perp}^2 \psi. \tag{2.9}$$

The perpendicular velocity can be obtained from the perpendicular component of the momentum conservation equation. Let $\mathbf{v}_E = c(\mathbf{E} \times \mathbf{B})/B^2$ be the nonrelativistic $\mathbf{E} \times \mathbf{B}$ drift. If we expand the perpendicular velocity as $\mathbf{U}_{e,\perp} = \mathbf{v}_E + \delta \mathbf{U}_{\perp}$, substitute in the momentum equation, and take the cross product with \mathbf{B} , to the next to leading order we get

$$U_{e,\perp} = v_E - \frac{m_e c}{eB^2} \mathbf{B} \times \frac{d_E}{dt} v_E, \qquad (2.10)$$

where $d_E/dt \equiv \partial/\partial t + \boldsymbol{v}_E \cdot \boldsymbol{\nabla}$. An order of magnitude estimate for the second term gives $(\omega/\Omega_e)v_E$, which is smaller than the first one by a factor ω/Ω_e , but we will keep it as the leading term will cancel out in the continuity equation.

The electric field can be separated into a potential part and a solenoidal part:

$$\boldsymbol{E} = -\boldsymbol{\nabla}\phi + \boldsymbol{E}_{\text{sol}},\tag{2.11}$$

where ϕ is the electric potential and

$$c\nabla \times \boldsymbol{E}_{\text{sol}} = -\partial_t \delta \boldsymbol{B}. \tag{2.12}$$

Thus, the $\mathbf{E} \times \mathbf{B}$ drift becomes

$$\frac{\boldsymbol{v}_E}{c} = \frac{\hat{\boldsymbol{z}} \times \boldsymbol{\nabla} \phi}{B_0} + \frac{\boldsymbol{E}_{\text{sol}} \times \hat{\boldsymbol{z}}}{B_0}.$$
 (2.13)

Substituting (2.9), (2.10), and (2.13) into the continuity equation and using (2.12) we get, to leading order

$$\partial_{t} \left(\frac{\delta n_{e}}{n_{0}} - \frac{\delta B_{z}}{B_{0}} + \frac{m_{e}c}{eB_{0}^{2}} \nabla^{2} \phi \right) + \frac{c}{B_{0}} (\hat{\boldsymbol{z}} \times \boldsymbol{\nabla} \phi) \cdot \boldsymbol{\nabla} \left(\frac{\delta n_{e}}{n_{0}} - \frac{\delta B_{z}}{B_{0}} + \frac{m_{e}c}{eB_{0}^{2}} \nabla^{2} \phi \right) - \frac{c}{4\pi n_{0}e} \nabla_{\parallel} \nabla_{\perp}^{2} \psi = 0.$$
 (2.14)

Next, we will work with the field-parallel component of the momentum conservation equation:

$$\frac{\partial U_{e,\parallel}}{\partial t} + (\boldsymbol{v}_E \cdot \boldsymbol{\nabla}) U_{e,\parallel} = -\frac{1}{m_e n_e} \nabla_{\parallel} P_e - \frac{e}{m_e} E_{\parallel}, \tag{2.15}$$

where we used $k_{\perp} \gg k_{\parallel}$ and $U_{e,\perp} \sim U_{e,\parallel}$ (this can be seen by writing the electron velocity in terms of the current density, the current density in terms of the magnetic field, and using $\delta B_{\perp} \sim \delta B_z$; see below) to approximate $(\mathbf{U}_e \cdot \nabla)U_{e,\parallel} \approx (\mathbf{v}_E \cdot \nabla)U_{e,\parallel}$. The parallel electric field can be written in terms of the electric and magnetic potentials:

$$E_{\parallel} = -\nabla_{\parallel}\phi + \frac{1}{c}\partial_t\psi. \tag{2.16}$$

The electron pressure fluctuations are negligible compared to the electric potential fluctuations, as can be seen using Equation (2.22) below and the condition $T_e \ll T_i$, so the pressure term

in (2.15) can be dropped. Then, substituting Equations (2.9) and (2.16) into (2.15) we get

$$\partial_t \left(\psi - d_e^2 \nabla_\perp^2 \psi \right) - d_e^2 (\boldsymbol{v}_E \cdot \nabla) \nabla_\perp^2 \psi = c \nabla_\parallel \phi. \tag{2.17}$$

We still have too many variables and too few equations. Let us find a way to relate the electric potential fluctuations ϕ with the magnetic fluctuations δB_z . To do this, we will return to the perpendicular momentum conservation equation, but this time we may neglect the $d\mathbf{U}_{e,\perp}/dt$ term (i.e., we only keep the lowest order of $\mathbf{U}_{e,\perp}$):

$$E_{\perp} + \frac{U_{e,\perp}}{c} \times B \approx 0.$$
 (2.18)

Writing the perpendicular velocity in terms of the current, and the current in terms of the magnetic field we get

$$U_{e,\perp} = -\frac{J_{\perp}}{n_e e} = -\frac{(\boldsymbol{\nabla} \times \boldsymbol{B})_{\perp}}{4\pi n_e e} c$$
 (2.19)

Substituting in (2.18) and using $(\nabla \times \boldsymbol{B}) \times \boldsymbol{B} = (\boldsymbol{B} \cdot \nabla) \boldsymbol{B} - (1/2) \nabla (B^2), B^2 \approx B_0^2 + 2B_0 \delta B_z$, and $k_{\perp} \gg k_{\parallel}$, we get

$$\boldsymbol{E}_{\perp} \approx \frac{c}{4\pi n_e e} [(\boldsymbol{B} \cdot \boldsymbol{\nabla}) \delta \boldsymbol{B}_{\perp} - B_0 \boldsymbol{\nabla}_{\perp} \delta B_z].$$
 (2.20)

Since $\delta B_{\perp} \sim \delta B_z$ (see Equation (2.28) below), the first term in the right-hand side in the equation above can be dropped. Then, using $\mathbf{E}_{\perp} = -\nabla_{\perp}\phi$, we get

$$\phi = \frac{cB_0}{4\pi n_e e} \delta B_z. \tag{2.21}$$

Next, we will relate ϕ with δn_e . Since for inertial kinetic Alfvén waves $\omega \ll k v_{\text{th},i}$, the ions

have time to adapt to the potential, so the Boltzmann formula for the density gives

$$\phi = -c\frac{T_i}{e}\frac{\delta n}{n_0},\tag{2.22}$$

where we also invoked quasineutrality to substitute $\delta n_i = \delta n_e \equiv \delta n$.

Combining equations (2.21) and (2.22), we get

$$\frac{\delta B_z}{B_0} = -\frac{\beta_i}{2} \frac{\delta n}{n_0}. (2.23)$$

Substituting (2.22) and (2.23) in Equations (2.14) and (2.17) we finally arrive at a system of two equations for the magnetic potential fluctuations ψ and the electron density fluctuations δn . We write the equations in terms of the dimensionless fluctuations $\tilde{\psi} = \psi/(d_e B_0)$, $\delta \tilde{n} = (\beta_i/2)(\delta n/n_0)$:

$$\frac{\partial}{\partial \tilde{t}} \left[(1 - \tilde{\nabla}_{\perp}^2) \tilde{\psi} \right] + \left[(\hat{\boldsymbol{z}} \times \tilde{\boldsymbol{\nabla}} \delta \tilde{n}_e) \cdot \tilde{\boldsymbol{\nabla}} \right] \tilde{\nabla}_{\perp}^2 \tilde{\psi} = -\tilde{\nabla}_{\parallel} \delta \tilde{n}, \tag{2.24}$$

$$\frac{\partial}{\partial \tilde{t}} \left[\left(1 + \frac{2}{\beta_i} - \tilde{\nabla}_{\perp}^2 \right) \delta \tilde{n} \right] + \left[(\hat{\boldsymbol{z}} \times \tilde{\boldsymbol{\nabla}} \delta \tilde{n}) \cdot \tilde{\boldsymbol{\nabla}} \right] \tilde{\nabla}_{\perp}^2 \delta \tilde{n} = \tilde{\nabla}_{\parallel} \tilde{\nabla}_{\perp}^2 \tilde{\psi}, \tag{2.25}$$

where $\tilde{t} = t\Omega_e$ and $\tilde{\nabla} = d_e \nabla$.

Linearizing these equations one obtains a mode we will call inertial kinetic Alfvén wave, with dispersion relation

$$\omega^2 = \frac{k_{\parallel}^2 v_A^2 k_{\perp}^2 \rho_i^2}{\beta_i (1 + k_{\parallel}^2 d_e^2) (1 + 2/\beta_i + k_{\perp}^2 d_e^2)},\tag{2.26}$$

and dimensionless amplitudes related as

$$\delta \tilde{n}_k^2 = \frac{1 + \tilde{k}_\perp^2}{1 + 2/\beta_i + \tilde{k}_\perp^2} \tilde{k}_\perp^2 \tilde{\psi}_k^2. \tag{2.27}$$

Combining equations (2.27) and (2.23) we obtain the magnetic compressibility:

$$\frac{\delta B_z^2}{\delta B_\perp^2} = \frac{1 + k_\perp^2 d_e^2}{1 + 2/\beta_i + k_\perp^2 d_e^2}.$$
 (2.28)

Equations (2.24) and (2.25) conserve the following quantity:

$$\mathcal{E} = \int \left[\delta \tilde{n} \left(1 + \frac{2}{\beta_i} - \tilde{\nabla}_{\perp}^2 \right) \delta \tilde{n} - \tilde{\nabla}_{\perp}^2 \tilde{\psi} (1 - \tilde{\nabla}_{\perp}^2) \tilde{\psi} \right] d^3 \tilde{x}. \tag{2.29}$$

In the regime of interest in this chapter, we have $\tilde{k}_{\perp}^2 = (k_{\perp}d_e)^2 \gg 1 + 2/\beta_i$, so equation (2.27) implies $\delta \tilde{n}_{\lambda} \sim \tilde{\psi}_{\lambda}/\tilde{\lambda}$, where $\delta \tilde{n}_{\lambda}$ and $\tilde{\psi}_{\lambda}$ denote the typical fluctuations of the dimensionless fields at scales $\tilde{\lambda} = \lambda/d_e$ across the guide field.

In this same limit, the nonlinear dimensionless time $\tilde{\tau}_{\lambda}$ can be estimated from Equations (2.24) and (2.25) as $\tilde{\tau}_{\lambda} \sim \tilde{\lambda}^2/\delta \tilde{n}$ by keeping only the leading order in $k_{\perp}d_e \sim \tilde{\lambda}^{-1}$. Let us say that \mathcal{E} cascades with constant flux ε , then $\varepsilon = w_{\lambda}/\tilde{\tau} \sim (\delta \tilde{n}_{\lambda}/\tilde{\lambda})^2/(\tilde{\lambda}^2/\delta \tilde{n}) \sim \delta \tilde{n}_{\lambda}^3/\tilde{\lambda}^4$, where w_{λ} was estimated from Equation (2.29). This leads to the following scaling for the density and magnetic fluctuations $\delta \tilde{n}_{\lambda} \sim \tilde{\psi}/\tilde{\lambda} \sim \varepsilon^{1/3} \tilde{\lambda}^{4/3}$, which implies density and magnetic energy spectra scaling as $S_{n,B} \propto k_{\perp}^{-11/3}$.

We can derive the anisotropy implied by the critical balance condition by balancing the linear and nonlinear terms in Equations (2.24) and (2.25), obtaining $\tilde{\psi}_{\lambda}\delta\tilde{n}_{\lambda}/\tilde{\lambda}^{4}\sim\delta\tilde{n}_{\lambda}/\tilde{\ell}$. Substituting the scaling laws derived for $\delta\tilde{n}_{\lambda}$ and $\delta\tilde{\psi}_{\lambda}/\tilde{\lambda}$, we get $\tilde{\ell}\sim\tilde{\lambda}^{5/3}$, where $\tilde{\ell}=\ell/d_{e}$ is the field-parallel scale.

For a discussion on the inertial whistler modes and the possibility that they are excited, we refer the reader to Chen and Boldyrev (2017).

Observations in the Earth's magnetosheath

Figure 2.1 is from Chen and Boldyrev (2017) and is made with data collected in the Earth's magnetosheath by the four MMS spacecraft during the period (2015 October 16,

¹We also note that if we take the limit $k_{\perp}d_e\ll 1$ we recover the $S_{n,B}\propto k_{\perp}^{-7/3}$ scaling of KAW turbulence.

09:24:11–09:25:24), when they were located 11.9 R_E from the Earth, with R_E the planet's radius. The average plasma parameters were: $B \approx 39$ nT, $n_i \approx n_e \approx 14$ cm⁻³, $U_i \approx U_e \approx 180$ km s⁻¹, $T_i \approx 210$ eV, $T_e \approx 23$ eV, with temperature anisotropies $(T_{\perp}/T_{\parallel})_i \approx 1.6$ and $(T_{\perp}/T_{\parallel})_e \approx 1.0$. This results in average betas $\beta_i \approx 0.79$ and $\beta_e \approx 0.087$. For details on the data collection and more extensive data analysis, we refer the reader to Chen and Boldyrev (2017). Here we just discuss some of their results.

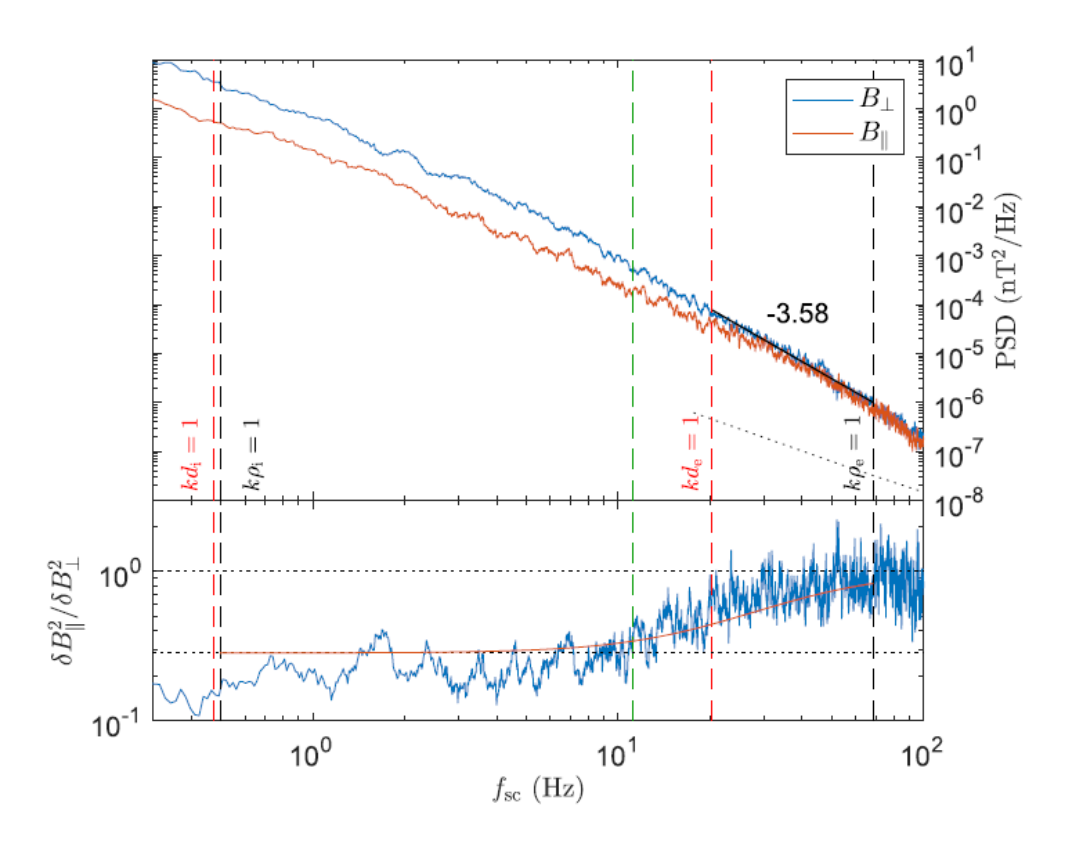


Figure 2.1: Top: Energy spectra of magnetic fluctuations. Bottom: Magnetic compressibility $\delta B_{\parallel}^2/\delta B_{\perp}^2$. The red solid line is Equation (2.28) and the black dotted lines show its asymptotic limits $1/(1+2/\beta_i)$ and 1. The green dashed line marks the scale given by Equation (2.2), where the frequency of Alfvén waves no longer satisfies $\omega \ll k_{\parallel}v_{\rm th,e}$. Figure 5 in Chen and Boldyrev (2017), copied here with the authors' permission.

Figure 2.1 shows the spectra of B_{\perp} and B_{\parallel} , and their ratio (i.e., the magnetic compressibility). $\delta |\mathbf{B}|$ was used as a proxy for δB_{\parallel} and $\delta B_{\perp}^2 = |\delta \mathbf{B}|^2 - \delta B_{\parallel}^2$. The frequency on the horizontal axis of the plots can be converted into a wavenumber k with the mean speed of the flow (i.e., the speed on a scale much larger than the turbulent fluctuations) by invoking

the Taylor hypothesis. Simply put, the Taylor hypothesis proposes that when the large-scale velocity is much larger than the turbulent fluctuations, the time measurement of the fields on a given point can be reinterpreted as a fixed-time cut across the turbulent environment as seen in the frame of reference that eliminates the large-scale flow. For a detailed analysis on the validity of the Taylor hypothesis for the spectra presented in this subsection, see Chen and Boldyrev (2017).

Understanding that the frequency is proportional to the wavenumber, the top panel of the figure shows good agreement with the predicted $k_{\perp}^{-11/3}$ scaling in the sub- d_e region. In the bottom panel, the magnetic compressibility is seen to increase from approximately $1/(1+2/\beta_i)$ to approximately 1, while following Equation (2.28) closely. We note that the increase in compressibility could not be due to noise, as random fluctuations would have the same average energy in all three components, resulting in $\delta B_{\parallel}^2/\delta B_{\perp}^2 = 0.5$, which is only seen for $f_{sc} > 200$ Hz. No hints of parallel propagating whistler waves are seen (they would appear as a bump in the magnetic energy spectrum; see, for example, Matteini et al. (2017)), so the observations are consistent with a transition to inertial kinetic Alfvén turbulence in the sub- d_e region.

Confirmation in numerical simulations

The existence of inertial kinetic Alfvén turbulence was confirmed in 2.5D (2D domain with 3-component vector fields) and 3D simulations (Roytershteyn et al., 2019). Here we will discuss some of the results in Roytershteyn et al. (2019); for more extensive data analysis we refer the reader to that paper.

The 2.5D simulation discussed in Roytershteyn et al. (2019) was run with particle-in-cell code VPIC (Bowers et al., 2008). The simulation was initialized with a uniform two-species plasma with Maxwellian velocity distributions, and the same uniform density n_0 for each species. The plasma parameters were: $\beta_e = 0.04$, $\beta_i = 0.4$, $\omega_{pe}/\Omega_{ce} = 2$, and $m_i/m_e = 100$. The simulation plane was perpendicular to the mean magnetic field B_0 ,

oriented in the z direction. The simulation domain was a double periodic $L \times L$ square with $L = 8\pi d_i = 80\pi d_e \approx 251 d_e$, resolution $n_x = n_y = 3456$ cells, and 4000 particles per cell per species. The time step was $\omega_{pe}\delta t \approx 0.05$.

Decaying turbulence was initialized by imposing randomly phased perturbations:

$$\delta \boldsymbol{B} = \sum_{k} \delta \boldsymbol{B}_{k} \cos(\boldsymbol{k} \cdot \boldsymbol{x} + \chi_{k}), \quad \delta \boldsymbol{U} = \sum_{k} \delta \boldsymbol{U}_{k} \cos(\boldsymbol{k} \cdot \boldsymbol{x} + \phi_{k}), \tag{2.30}$$

with the wave numbers $\mathbf{k} = \{2\pi m/L, 2\pi n/L\}$, with m = -2, ..., 2 and n = 0, ..., 2. The injection scale of turbulence is, thus, $k_{\perp}d_i \approx 0.7$. The amplitudes of the initial modes satisfy conditions $\mathbf{k} \cdot \delta \mathbf{B}_k = 0$, $\mathbf{B}_0 \cdot \delta \mathbf{B}_k = 0$, $\mathbf{k} \cdot \delta \mathbf{U}_k = 0$, and $|\delta \mathbf{B}_k|/B_0 = |\delta \mathbf{U}_k|/v_A$, where $\delta \mathbf{U}$ is the ion and electron bulk velocity fluctuation² and $v_A = B_0/(4\pi n_0 m_i)^{1/2}$ is the Alfvén speed. The initial root-mean-square magnetic fluctuation was $\langle \delta B^2(\mathbf{x}, t = 0) \rangle^{1/2}/B_0 = \langle \delta U^2(\mathbf{x}, t = 0) \rangle^{1/2}/v_A \approx 0.1$, so the initial average energy density of the magnetic and kinetic fluctuations together was $\mathcal{U} \approx 0.01B_0^2$.

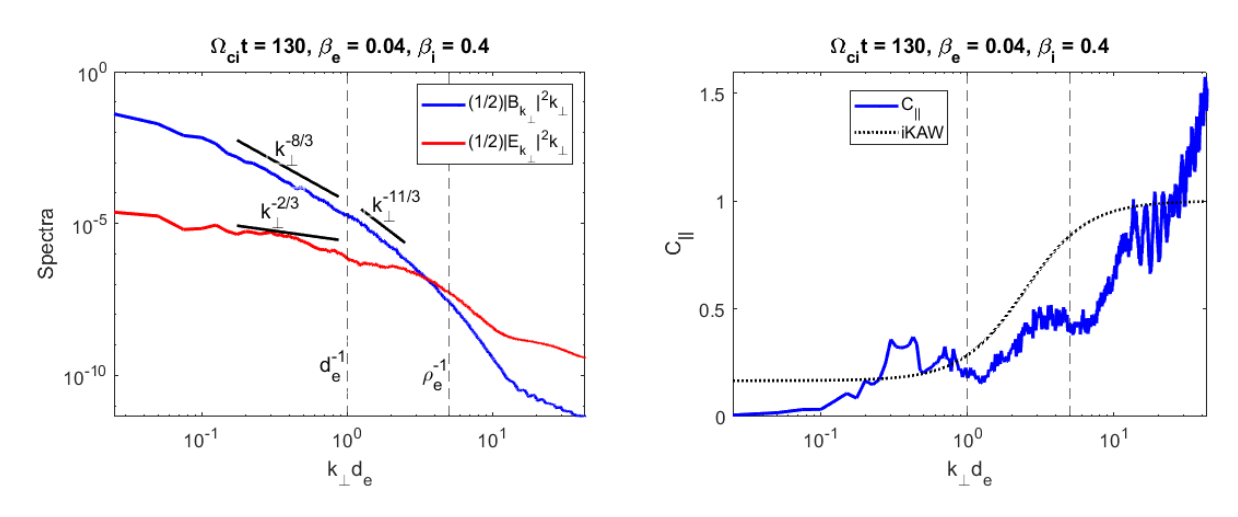


Figure 2.2: Left: Magnetic (blue) and electric (red) energy spectra. Right: Magnetic compressibility. The dashed line shows the analytic prediction of Equation 2.28. In both panels, the vertical lines mark scales corresponding to (in order of increasing k_{\perp}) $k_{\perp}d_e = 1$ and $k_{\perp}\rho_e = 1$.

The left panel of Figure 2.2 shows the magnetic and electric energy spectra at a time

²The electron velocity was slightly higher than the ion velocity to provide the current density corresponding to $\nabla \times \mathbf{B}$.

when turbulence was fully developed. Three distinct ranges of scales can be identified in the spectra. At $k_{\perp}d_e \lesssim 1$ the magnetic energy spectrum exhibits a spectral index close to the theoretical prediction of -8/3 of intermittent kinetic Alfvén turbulence (e.g., Boldyrev and Perez, 2012) and to observations of -2.8 in space plasmas (e.g., Alexandrova et al., 2009; Kiyani et al., 2009; Chen et al., 2010, 2012; Chen and Boldyrev, 2017) and other simulations (e.g., Howes et al., 2011; Boldyrev and Perez, 2012; Sahraoui et al., 2013b; Grošelj et al., 2018). Furthermore, the electric energy spectrum scales close to $k_{\perp}^2 S_B$, with S_B the magnetic energy spectrum. In the range of scales $d_e^{-1} \lesssim k_{\perp} < \rho_e^{-1}$, the magnetic energy spectrum has steepened to a slope close to the -11/3 predicted by inertial kinetic Alfvén turbulence, also observed in the magnetosheath (Chen and Boldyrev, 2017) and the 3D simulation in Roytershteyn et al. (2019). One last transition happens across $k_{\perp}\rho_e \sim 1$, where the spectrum steepens even further due to increased electron Landau damping.

The right panel of Figure 2.2 shows the magnetic compressibility $\delta B_{\parallel}^2/\delta B_{\perp}^2 \approx \delta B_z^2/(\delta B_x^2 + \delta B_y^2)$ together with the theoretical model given by Equation 2.28. The model is seen to reproduce the general trendline up to $k_{\perp} \lesssim \rho_e^{-1}$, but $\beta_e = 0.04$ gives a very small separation of scales and finite gyroradius effects would need to be considered for a better fit.

Analysis of the frequency spectrum of the magnetic fluctuations done in Roytershteyn et al. (2019) further corroborates the presence of kinetic inertial Alfvén modes.

2.2 Electron-only magnetic reconnection

Finding reconnection sites in 2.5D simulations

In this subsection, we implement a numerical method to look for electron-only magnetic reconnection in data from the 2.5D VPIC simulation discussed in the previous section and an additional 2.5D VPIC simulation with $\beta_e = \beta_i = 0.5$, resolution $n_x = n_y = 1024$, 10000 particles per cell per species, time step $\omega_{pe}\delta t \approx 0.17$, and same parameters as the low electron beta simulation otherwise. The turbulence was also initialized in the same way. In the

presentation below we closely follow Vega et al. (2020) (for other similar numerical studies of magnetic reconnection in turbulent plasmas, see Haggerty et al. (2017) and references therein).

In a 2D domain, the in-plane magnetic field can be computed from a single-component potential function:

$$\boldsymbol{B}_{\perp} = \boldsymbol{\nabla} \times (\psi \hat{\boldsymbol{z}}) = \frac{\partial \psi}{\partial y} \hat{\boldsymbol{x}} - \frac{\partial \psi}{\partial x} \hat{\boldsymbol{y}}.$$
 (2.31)

Since $\mathbf{B}_{\perp} \cdot \nabla \psi = 0$, the in-plane magnetic field is tangent to the contour lines of ψ . Moreover, since $\mathbf{B}_{\perp} = 0$ at the X-point, from Equation (2.31) we get $\nabla \psi = 0$. This and the magnetic field topology around the X-point imply that ψ has a saddle point wherever there is reconnection, so to find the reconnection candidates we start by looking for these saddle points.

To find ψ from the simulation data, we start from Ampère's law (just like in the previous section, we assume that the displacement current can be neglected):

$$\nabla \times \boldsymbol{B}_{\perp} = \frac{4\pi}{c} \boldsymbol{J}_{z}. \tag{2.32}$$

Using 2.31 and writing $J_z = J_z \hat{z}$ we get the following Poisson equation:

$$\nabla^2 \psi = -\frac{4\pi}{c} J_z,\tag{2.33}$$

or, in Fourier space

$$\psi_k = \frac{4\pi}{c} \frac{J_{zk}}{k^2}, \quad k \neq 0.$$
 (2.34)

The scalar field ψ can then be obtained by anti-transforming ψ_k . This method to solve the Poisson equation was implemented in Matlab using this program's fast Fourier transform.

The saddle points of ψ were found by numerically computing its first and second derivatives.

The numerical gradient of the potential is never exactly zero, so we looked for points where the determinant of the Hessian matrix was negative and the first derivatives were less than 1% of the standard deviation of the derivatives over the whole domain.

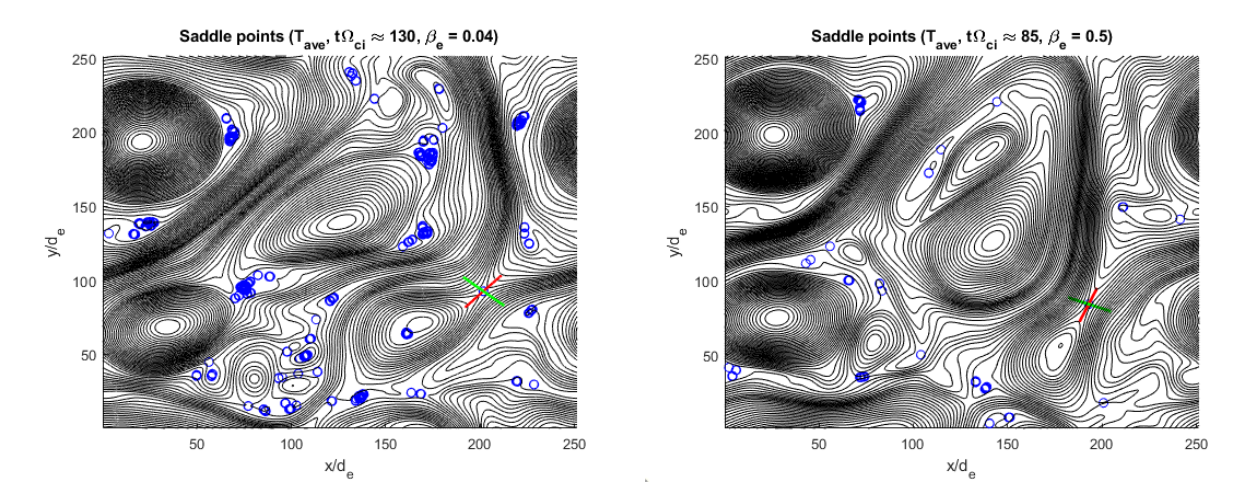


Figure 2.3: Contour lines of the magnetic potential ψ (black) and saddle points of ψ (blue). Left: $\beta_e = 0.04$. Right: $\beta_e = 0.5$. Visual inspection reveals electron-only reconnection candidates in both cases; the green-red X signs mark the specific regions analyzed in detail below. The red and green lines were traced following the direction of the (orthogonal) Hessian eigenvectors at the corresponding saddle points.

Figure 2.3 shows the contour lines of ψ and the saddle points found after several eddy turnover times (the eddy turnover time being approximately $30\Omega_{ci}^{-1}$), in both the $\beta_e = 0.04$ and $\beta_e = 0.5$ simulations. Direct inspection of the contour lines reveals a good reconnection candidate, marked in each case with an X, with the red line corresponding to the direction of the outflow and the green line to the inflow, directions given by the eigenvectors of the Hessian matrix of ψ . To confirm that this is a reconnection event, we plot in Figure 2.4 cuts of the fields along the inflow and the outflow. This figure shows the reconnecting component of the magnetic field (B_1) , the electron inflow and outflow velocities $(U_{e2}$ and $U_{e1})$, the ion inflow and outflow velocities $(U_{i2}$ and $U_{i1})$, the electron density (n_e) , and the out-of-plane current density (J_z) along the inflow and outflow directions. The velocities were normalized to the electron Alfvén velocity computed with the reconnecting magnetic field, estimated as half the jump of the magnetic field across the electron inflow layer. The magnetic field was

normalized to the guide field B_0 . The velocity plots show that in these reconnection sites the ions do not couple to the electron inflow and outflow, similar to the observational results by Phan et al. (2018).

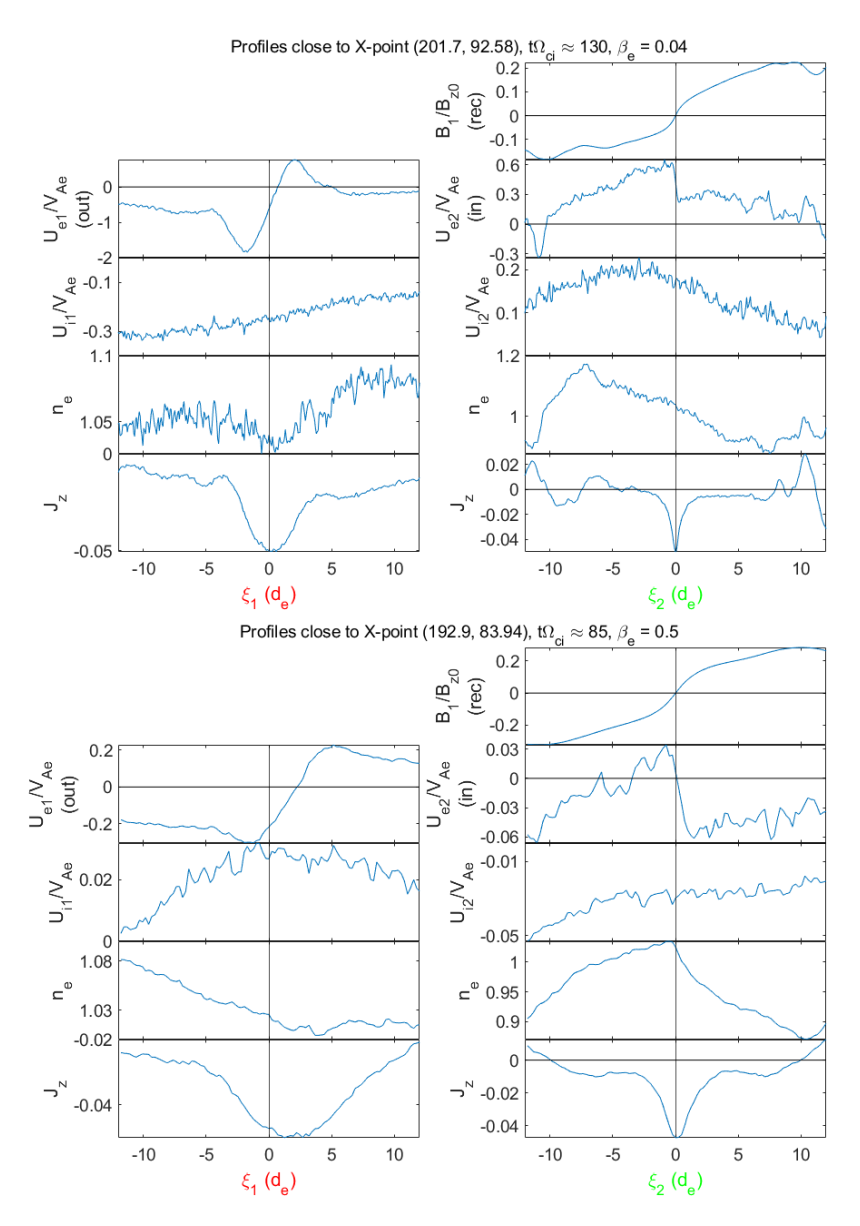


Figure 2.4: Profiles around the X-points marked on Figure 2.3. Direction ξ_1 corresponds to the Hessian eigenvector directed along the outflow, while ξ_2 is directed along the inflow. The X-point found by the Matlab algorithm is at $\xi_1 = \xi_2 = 0$. In the $\beta_e = 0.5$ example, the J_z peak and the zero of the outflow velocity deviate from the position of the X-point, which is expected since the reconnection layer is not perfectly symmetric (e.g., Cassak and Shay, 2007; Doss et al., 2015). In both cases, a large-scale plasma flow at the X-point results in nonzero mean electron and ion flows in the reconnection layer.

As explained in Section 1.5, we can understand why the ions do not couple to the electron motion by noting that in the sub- d_i scale, ion inertia becomes important, so they no longer move with the magnetic field lines the way electrons do. Indeed, studies have shown that for electron scale reconnecting current sheets only electrons participate in the reconnection event, with ions gradually coupling to the inflow and outflow as the length of the current sheet is increased up to tens of d_i , where we recover the traditional, double layer magnetic reconnection (e.g., Mandt et al., 1994; Phan et al., 2018; Sharma Pyakurel et al., 2019).

Analyzing the sizes of the out-of-plane current sheets characterized by the current density J_z , we find that in the run with $\beta_e = 0.04$ (top panel in Figure 2.4) the thickness of the current sheet is about $T \sim 0.5 d_e$, while its length is about $L \sim 4 d_e$. In the run with $\beta_e = 0.5$ (bottom panel in Figure 2.4), the current sheet dimensions are slightly larger. In both cases, however, the lengths of the current sheets and electron outflow regions are significantly smaller than the scale $\sim 40 d_i$ necessary for ion coupling.

To find more reconnection candidates, we looked for saddle points within intense current sheets. The first step in constructing the current sheets is to locate all the points of the simulation grid where the current density is above a given threshold (chosen to be 3 times the rms current density). Next, the local maxima are found among those points by looking at the current density on a square window of side 2n + 1 centered on the point of interest (we used n = 3). Points where the current density is the maximum within the window are classified as local maxima. Going through the local maxima from highest to lowest, the following procedure is performed. Starting on the point with the highest current density, its four closest neighbors are checked, and those with current density above a certain threshold (chosen to be 75% of the local maximum) are taken to be part of the current sheet. The neighbors of the new points are then checked and so on until the boundary points of the current sheet are surrounded by points with current density below the threshold (while for all the points in the current sheet it is above). When this process is completed for one local maximum, the program moves on to the next one. If this one belongs to any of the current

sheets already found, it is skipped. This algorithm, which was implemented in Matlab, is based on the algorithm previously discussed in Zhdankin et al. (2013).

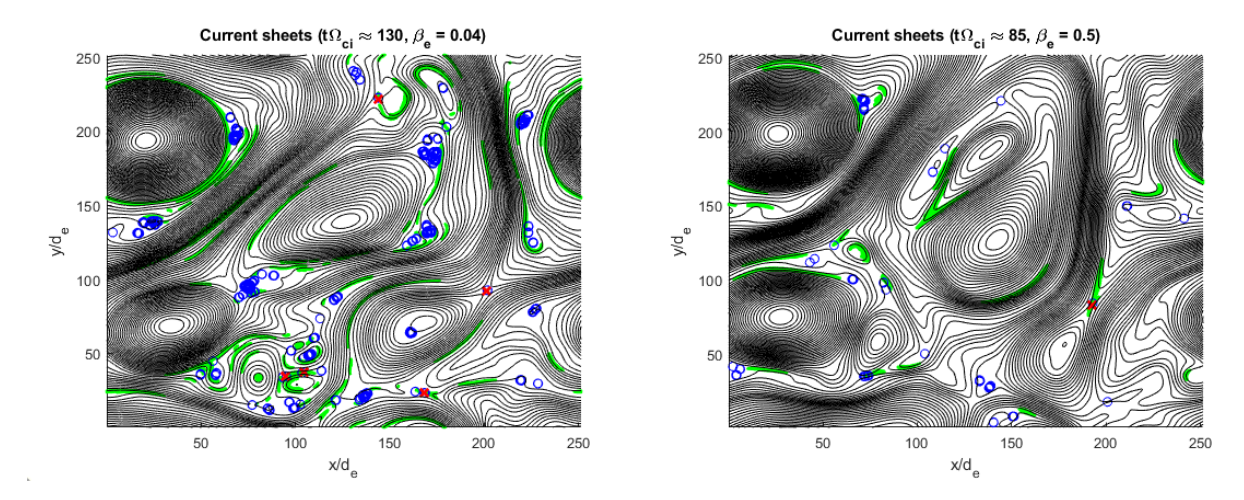


Figure 2.5: Current sheets found (in green). The red Xs are the current peaks of those sheets containing saddle points (blue circles).

For each current sheet, our program measures its length L, defined as the largest distance between any two points belonging to it, and the thickness T, defined as its size in the direction of most rapid descent from the peak. The current sheets found in both the low and high electron beta simulations at a particular time are shown in Figure 2.5. The red Xs mark the peaks of current sheets that overlap with saddle points (potential reconnection sites). Interestingly, only one current sheet containing a saddle was found in the high electron beta run, corresponding to the reconnection site discussed above. The reconnecting current sheet length determined by our algorithm was 14.6 d_e and the thickness was 1.2 d_e . In the low electron beta case, five reconnection candidates were found by our algorithm, including the example discussed previously and displayed in Figure 2.4. The lengths measured for the current sheets ranged from 3.2 d_e to 18.1 d_e , with an average of 7.9 d_e . The thicknesses ranged from 0.4 d_e to 1.0 d_e , with an average of 0.6 d_e .

³To understand how generic such a situation is, the algorithm was applied to a few other randomly selected snapshots in both the low and high electron beta simulations, finding from 5 to 8 reconnection sites per snapshot in the former case and from 1 to 3 in the latter. This suggests that electron-only reconnection events are easier to generate in the low electron beta environment.

We checked that, out of the five reconnection candidates found by the algorithm in the low electron beta case, the profiles corresponding to the X-points with coordinates $(x/d_e, y/d_e) = (104.4, 37.4)$ and $(x/d_e, y/d_e) = (143.9, 221.7)$ have a structure qualitatively similar to the example shown in Figure 2.4. For the remaining two points, with coordinates $(x/d_e, y/d_e) = (94.7, 34.2)$ and $(x/d_e, y/d_e) = (168.4, 23.7)$, it is harder to clearly identify an electron inflow and outflow due to the strongly asymmetric structures of the current sheets, as can be seen in Figure 2.5.

Finally, we estimated the reconnection rate of the electron-only reconnection sites in both the low and high electron beta simulations. Several traditional methods were considered. First, one can define a local reconnection rate by using the magnetic and electric fields on the scale of the electron layer (e.g., Cassak et al., 2017). However, we found that in the low electron beta case, the electron inflow velocity $U_{e,2}$ does not agree with the $E \times B$ velocity, E_z/B_2 (the subscript '2' refers to the inflow direction as labeled in Figure 2.4). The latter, measured at distance $\pm T$ from the midplane of the reconnection layer, produces a value several times larger than the electron inflow velocity measured directly. This may be related to the presence of strong gradients of the electric field, gradients of pressure, and electron inertial effects inside the structure. Another way of measuring the reconnection rate is by finding the ratio of the electron inflow velocity to the electron outflow velocity. This method was also found to be unreliable, giving in some cases reconnection rates above unity. This may be due to the difficulties in identifying the right points to measure the inflow and outflow velocities in the case of asymmetric current sheets.

On the other hand, if we assume that there is no accumulation of electric charge on the reconnection sites (i.e., a steady state), for each of them we must have $U_{e,inflow}L \sim U_{e,outflow}T$ (all the electrons flowing in must also flow out), implying $U_{e,inflow}/U_{e,outflow} \sim T/L$. Thus, the current sheet aspect ratio, T/L, which can be reliably measured by our algorithm, can be used as a proxy for the reconnection rate. In this way, the average reconnection rate obtained in the low electron beta case was 0.093, while in the high electron beta case, it was

0.084. The aspect ratio T/L was also calculated for other values of the threshold used to define the current sheets, producing similar results. Rather interestingly, the results are close to 0.1, which may suggest that the previously established result on collisionless magnetic reconnection (e.g., Birn et al., 2001; Comisso and Bhattacharjee, 2016; Cassak et al., 2017) also applies to the novel electron-only reconnection regime.

Finding reconnection sites in 3D simulations

Finding reconnection candidates in 3D is significantly harder than in 2.5D, as one cannot rely on looking for X-points. In previous studies, reconnection was found in 3D simulations by identifying sites where numerous reconnection signatures were present simultaneously (e.g., large current density, particle heating, fast ions and electrons; see, for example, Agudelo Rueda et al. (2021)). Closely following Vega et al. (2023b), we take a similar approach and find candidates for electron-only reconnection by searching for large values of the pressure-strain interaction (a signature of particle heating (Yang et al., 2017, 2022, and Section 1.4)) and large variations in the electron fluid velocity (a signature of fast electron outflows) in the vicinity of strong current peaks.

Our 3D simulation, analyzed in Vega et al. (2023b), was run with spectral code SpectralPlasmaSolver (SPS), developed at Los Alamos National Laboratory. SPS solves the kinetic equations for all plasma species by expanding the particle distribution function in Hermite functions (akin to a moment expansion). It results in a truncated set of three-dimensional partial differential equations (PDEs) for the expansion coefficients whose expressions can be explicitly found in Delzanno (2015); Roytershteyn et al. (2018).

The simulation was initialized with a uniform two-species plasma with Maxwellian velocity distributions corresponding to $\beta_e = 0.1$, $\beta_i = 1$, and the same uniform density n_0 for each species, embedded into a uniform magnetic field of strength B_0 oriented in the z direction. The ratio of the plasma electron frequency to the electron cyclotron frequency was $\omega_{pe}/\Omega_{ce} = 100$, and the ion-to-electron mass ratio was $m_i/m_e = 100$. The dimensions of the simulation

domain were $L_x = L_y = 10d_i = 100d_e$ and $L_z = 60d_i = 600d_e$, and periodic boundary conditions were used. The spatial domain was decomposed into $511 \times 511 \times 63$ Fourier modes and the velocity domain in $4 \times 4 \times 4$ Hermite modes. The reduced spatial resolution in the z-direction reflects the fact that in the presence of a strong guide field, turbulent fluctuations are anisotropic, approximately satisfying the critical balance condition, $k_z/k_{\perp} \sim \delta B/B_0$ (e.g., Boldyrev and Perez, 2012; TenBarge and Howes, 2012; Boldyrev et al., 2021). The use of reduced resolution in the parallel direction excludes the possibility of describing fluctuations with very short parallel wavelengths. At present, there is little evidence to suggest that coupling to such fluctuations is an important process in the turbulent regime considered. Consequently, the resolution was chosen to reduce the numerical cost of the simulation. The model utilized here can be thought of as an advanced two-fluid model retaining 128 fluid moments (64 per species) and utilizing a closure at the level of heat flux tensor (see, e.g., discussion in Delzanno, 2015; Roytershteyn et al., 2018). The artificial collisional operator had collisionality $\nu = 0.01\omega_{pe}$ (Delzanno, 2015). The time step was $\Omega_{ce}\delta t = 1$. We emphasize that the implicit time discretization used in SPS allows us to study a regime with rather large ω_{pe}/Ω_{ce} , which is extremely challenging for algorithms based on explicit time discretization, such as those used in many production PIC codes.

Decaying turbulence was seeded by imposing randomly phased initial perturbations of the magnetic and velocity fields of the type

$$\delta \boldsymbol{B} = \sum_{k} \delta \boldsymbol{B}_{k} \cos(\boldsymbol{k} \cdot \boldsymbol{x} + \chi_{k}), \quad \delta \boldsymbol{U} = \sum_{k} \delta \boldsymbol{U}_{k} \cos(\boldsymbol{k} \cdot \boldsymbol{x} + \phi_{k}), \quad (2.35)$$

with the wave numbers $\mathbf{k} = \{2\pi l/L_x, 2\pi m/L_y, 2\pi n/L_z\}$, where l, m = -2, ..., 2 and n = 0, ..., 2. Since we initialize $k_z = 0$ modes, certain modes are included in the sum twice (e.g., $(k_x, k_y, 0)$ and $(-k_x, -k_y, 0)$), so the sum is further restricted to make sure that each \mathbf{k} is sampled only once. The injection scale of turbulence is thus $k_{\perp}d_i \approx 2$. In (2.35) $\delta \mathbf{U}$ refers to the ion and electron velocities (just like in the 2.5D case, electrons are a bit faster than ions

to generate the current required by the initial magnetic field). The amplitudes of the initial modes satisfy conditions $\mathbf{k} \cdot \delta \mathbf{B}_k = 0$, $\mathbf{B}_0 \cdot \delta \mathbf{B}_k = 0$, $\mathbf{k} \cdot \delta \mathbf{U}_k = 0$, and $|\delta \mathbf{B}_k|/B_0 = |\delta \mathbf{U}_k|/V_A$, where $V_A = B_0/(4\pi n_0 m_i)^{1/2}$ is the Alfvén speed. The initial root-mean-square fluctuation was $\langle \delta B^2(\mathbf{x}, t = 0) \rangle^{1/2}/B_0 = \langle \delta U^2(\mathbf{x}, t = 0) \rangle^{1/2}/V_A \approx 0.071$, implying that the initial average energy density of the magnetic and kinetic fluctuations together was $\mathcal{U} \approx 0.005 B_0^2$.

We applied the algorithm described in the previous subsection to generate 2D current sheets on each guide-field-perpendicular 2D layer of the 3D simulations (we note that different 2D current sheets found this way are actually part of the same 3D current ribbon). We looked for current peaks that were at least twice the rms current in the whole domain and defined the current sheets around each peak as those points where the current density was at least 50% of the peak. In the next section, we will analyze the statistics of the current sheets and their role in energy dissipation. Here we will look at one particular current sheet that stands out for displaying the highest energy dissipation rate \mathcal{R} of any site in the whole domain in any of the time slices analyzed, where we used the pressure-strain interaction $\mathcal{R} = -[(P_e \cdot \nabla) \cdot U_e + (P_i \cdot \nabla) \cdot U_i]$ as a measure of dissipation (see Yang et al. (2017, 2022) and Section 1.4). P_s and U_s are the pressure tensor and fluid velocity of species s, respectively.

Closer inspection of this site reveals multiple signatures of electron-only magnetic reconnection. The top-left panel in Figure 2.6 shows the electron fluid velocity U_{ey} normalized to the electron Alfvén speed, with the in-plane electron streamlines in black. Inflow and outflow patterns are clearly present. The corresponding profiles of the in-plane electron and ion fluid velocities, the in-plane magnetic field, and the out-of-plane current density along the inflow and outflow directions are shown in the bottom-left panel of Figure 2.6. The direction of the outflow cut (marked by the green line) was chosen so that it connects the maxima of the y-component of the electron fluid velocity. The inflow direction (red line) was chosen along the x-direction. All the fluid velocities are normalized to the electron Alfvén speed computed with the rms in-plane magnetic field. We note that, unlike the case of 2D reconnection, nearly Alfvénic velocities are seen not only along the outflow but also along the inflow. Similar

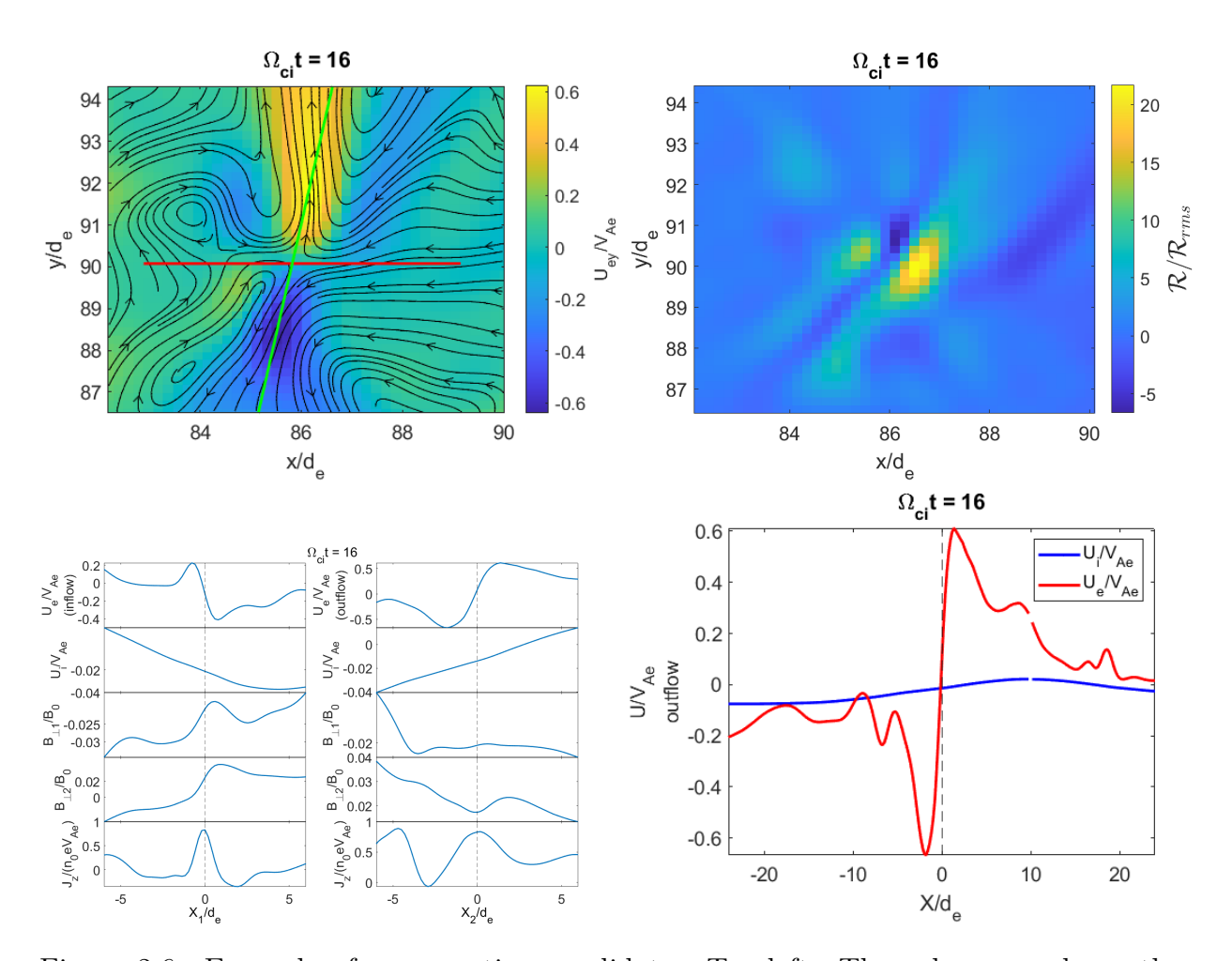


Figure 2.6: Example of reconnection candidate. Top-left: The color map shows the y component of the electron flux and the arrows show the electron fluid velocity. Bottom-left: Profiles of different fields along the inflow (direction X_1 ; red line in top panel) and the outflow (direction X_2 ; green line in top panel). Top-right: Color map of pressure-strain interaction. Bottom-right: Ion (blue) and electron (red) velocities along outflow. The horizontal scale spans about $5d_i$, or half the domain length in the field-perpendicular plane. There is no ion coupling to the electron motion.

enhanced inflows were also observed in 3D reconnection simulations in Pyakurel et al. (2021), where it was attributed to a significant mass outflow along the guide field.

The top-right panel of Figure 2.6 shows the large peak in \mathcal{R} that was found around the reconnection site. The bottom right panel displays the ion and electron outflows in an enlarged region spanning half the field-perpendicular domain. As can be seen in the figure, ion flows are significant (relative to the ion Alfvén speed, which for the given mass ratio is ten times smaller than the electron Alfvén speed) and do exhibit a reversal around the reconnection site. At the same time, ion and electron motions remain decoupled until outflows begin to interact with other turbulent structures on the scales comparable to the ion gyroradius (recall that here $\beta_i \approx 1$ and hence $\rho_i \approx d_i \approx 10d_e$). In this sense, it is appropriate to interpret the presented reconnection event as electron-scale reconnection.

The reconnection site shown in Figure 2.6 is part of a 3D current structure elongated along the background field, with a field-parallel length of approximately $300d_e$. Its average half-thickness and half-length are $0.77d_e$ and $7.5d_e$, respectively. The in-plane length was defined the same way as in the 2.5D case, but due to the complex topology displayed by many current sheets, for the thickness we used the medial axis transform, originally introduced in Blum (1967).

Before we continue characterizing this reconnection site, let us briefly discuss the medial axis transform. The medial axis transform defines the so-called skeleton (or medial axis) of an object (e.g., a current sheet) as the locus of points that have more than one closest point on the boundary of the object. In 2D, the skeleton consists of the centers of circles that are tangent to the contour at two points at least. The skeleton preserves the topology of the original shape so the method is well-suited for defining the thickness of current sheets with complex shapes. The left panel of Figure 2.7 shows an example of the "skeletonization" of a 2D current sheet. The boundary of the current sheet is shown in red and the skeleton is shown in a color map representing the distance of each point of the skeleton to the boundary

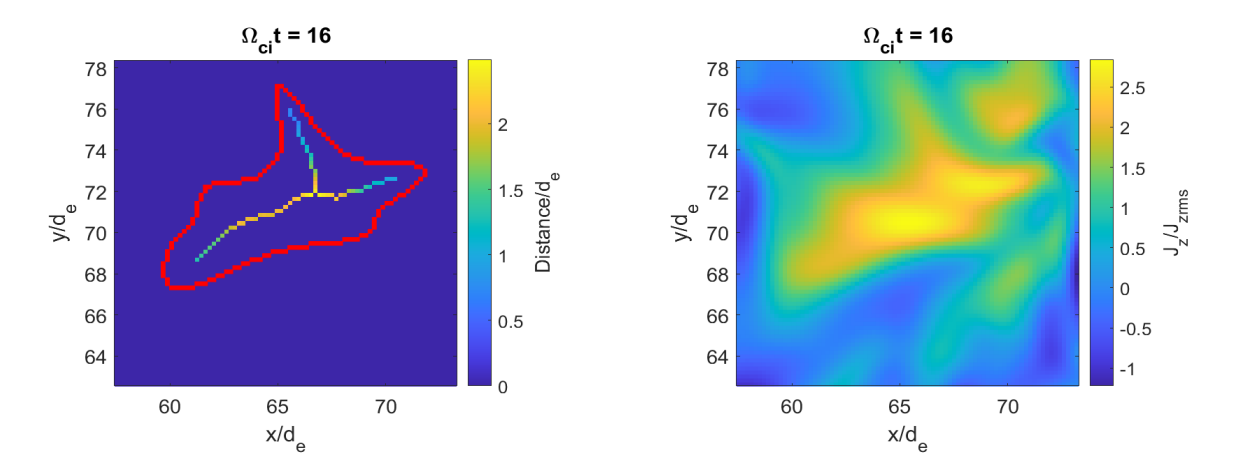


Figure 2.7: Left panel: Example of skeletonization of a current sheet. The red curve traces the boundary of the current sheet as defined in the text. The curve within is the skeleton obtained with the medial axis transform, with the color code representing the shortest distance to the red boundary. Right panel: Color map of the same current sheet.

(that is, the radius of the corresponding inscribed circle).⁴ For comparison, the right panel of Figure 2.7 shows a color map of the current sheet.

The skeleton (or medial axis) and the distance of each point on it to the boundary of the current sheet (the radius function) were obtained using the Matlab Image Processing Toolbox functions "bwskel" and "bwdist", respectively. The half-thickness, T, was then estimated by averaging the radius function over the points of the skeleton.

Going back to the 3D reconnecting structure, to estimate its value of \mathcal{R} we consider the 2D areas made of $2.5d_e \times 2.5d_e$ windows centered on each point of the skeleton of each 2D current sheet that spans the 3D structure over 30 field-perpendicular planes, and we compute \mathcal{R} within these areas. The size of the windows was chosen to enclose peaks in \mathcal{R} as observed in the top-left panel of Figure 2.6. \mathcal{R} computed this way, for this particular 3D structure, turns out to contribute 25% of the total pressure-strain interaction in the whole domain, in only 0.26% of the total volume.

We have also examined other metrics typically associated with reconnection for the structure discussed above. It was found that this structure corresponds to one of the largest

⁴The skeleton together with the corresponding radius function constitute the medial axis transform.

values of magnetic shear in the simulation, which was analyzed by studying the mapping of the field lines between two xy planes of the simulation located at different z (e.g., Daughton et al., 2014, and references therein). It also corresponds to large electron agyrotropy (Scudder and Daughton, 2008), which signals departures of the electron velocity distribution function from cylindrical symmetry about the local magnetic field.

2.3 Role of current sheets in energy dissipation

Statistics of current sheets

In the previous section, we explained how we identified and measured 2D current sheets on each field-perpendicular cut of the 3D SPS simulation. Figure 2.8 shows the distributions of the measured thicknesses and lengths, as well as the aspect ratios of the current sheets (Vega et al., 2023b). These distributions show that these are electron-scale current sheets, as expected given the low electron beta.⁵

Figure 2.8 also contains a similar analysis performed for two specific subsets of the 2D current sheets. The first subset is characterized by large values of the pressure-strain interaction, which may indicate strong energy dissipation. The second subset is characterized by large changes in the velocity of the electron flow, which may indicate the presence of outflows expected in electron-only reconnection. The distributions of both subsets and their intersection, shown in purple, follow a similar trend. However, since only 16 current sheets satisfy both the pressure-strain interaction and electron bulk velocity criteria, this subset of current sheets has limited statistical significance.

We placed a 2D current sheet into the large pressure-strain interaction subset if there existed a point within a window of $2.5d_e \times 2.5d_e$ centered on its skeleton where \mathcal{R} was at least ten times its root-mean-square (rms) value over the whole domain. The window size was

⁵It should be noted that the lack of ion scale current sheets is due to the choice of energy injection scale and box size. However, the relevant observation is that kinetic scale turbulence indeed creates electron scale current sheets.

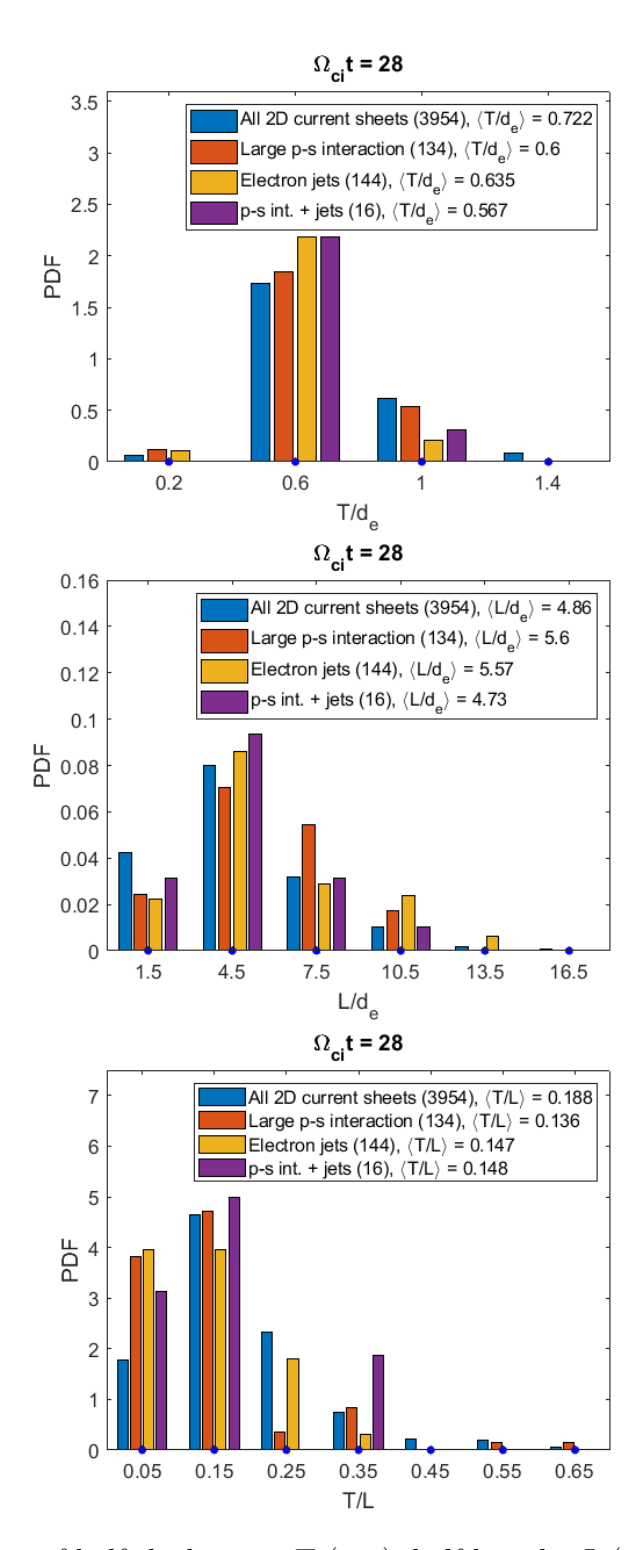


Figure 2.8: Histograms of half-thicknesses T (top), half-lengths L (middle), and aspect ratios T/L (bottom) of the 2D current sheets, with different sets shown in different colors. The number of 2D current sheets in each case is shown in parentheses. The blue dots mark the centers of the bins. The data denoted by different colors belong to the same bins but are shifted for clarity.

chosen to pick up peaks in \mathcal{R} , similar to the ones seen in the top-right panel of Figure 2.6. Such peaks are typically found around a current sheet skeleton but they do not overlap with it.

Similarly, we placed a 2D current sheet into the large-electron-outflow subset if it contained a large variation of the electron velocity U_e in the vicinity of its skeleton. Specifically, we looked for variations in the in-plane electron fluid velocity larger than 95% of the electron Alfvén velocity V_{Ae} within $5d_e \times 5d_e$ windows centered on the skeletons. (Here V_{Ae} is defined with the rms value of the in-plane magnetic field.) Such structures are of interest because the presence of electron outflows is one of the signatures (but not a guarantee) of magnetic reconnection, and also because velocity gradients explicitly enter the expression for \mathcal{R} . The distributions of current sheet sizes corresponding to different subsets look similar and have comparable averages. However, more intense energy dissipation and/or electron outflows seem to favor more anisotropic current sheets.

Intermittency of energy dissipation

To illustrate the intermittency of energy dissipation (i.e., a significant contribution to the dissipation coming from a small fraction of the domain; see, for example, Wan et al. (2012); Zhdankin et al. (2016); Camporeale et al. (2018); here we follow Vega et al. (2023b)), we consider the relation between current density and energy dissipation in the 2D current sheets. The left panel of Figure 2.9 shows the average \mathcal{R} computed within $2.5d_e \times 2.5d_e$ windows centered on those points of current sheet skeletons where the current density is above a given threshold. This figure demonstrates that, indeed, the average \mathcal{R} is higher in the vicinity of intense current sheets, reaching values that are over a hundred times the average where the current densities are four times the rms.

The right panel of Figure 2.9 shows, in blue, \mathcal{R} integrated over the corresponding vicinities of the skeletons, normalized to \mathcal{R} integrated over the whole domain. In red, we show the corresponding areas (2D volumes) over which \mathcal{R} was integrated, normalized to the volume

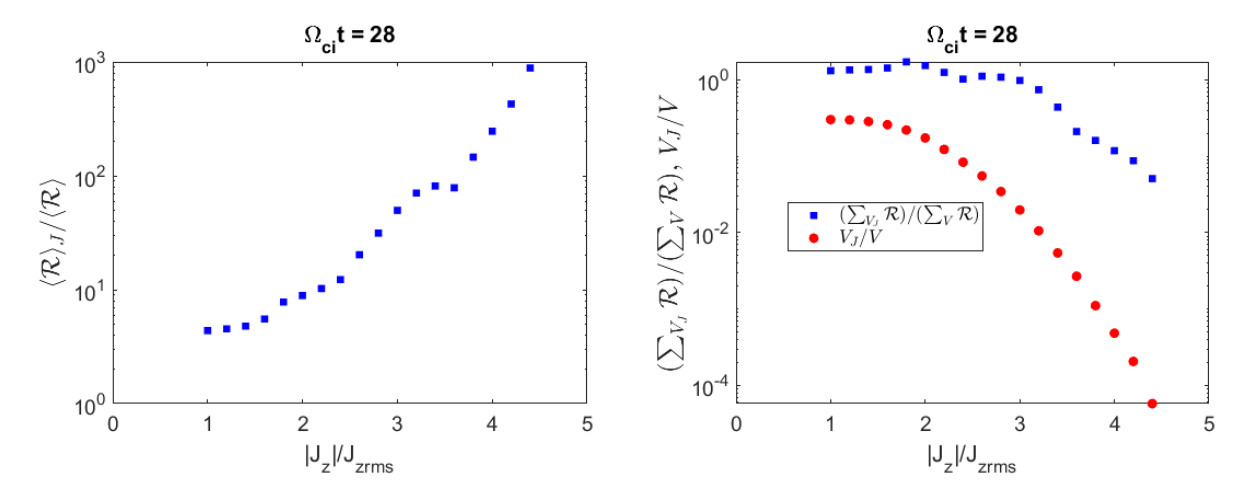


Figure 2.9: Left: Average pressure-strain interaction around points of the current sheet skeletons where the current density is above the threshold shown on the horizontal axis. The pressure-strain interaction is normalized to its average over the whole domain and the current density is normalized to its rms value. Right: Fraction of the overall pressure-strain interaction contributed by the vicinity of points of current sheet skeletons (in blue). The fractional volume occupied by the region around skeletons where pressure-strain interaction was computed (in red).

of the whole domain. This plot illustrates the intermittency of intense energy dissipation. Notably, \mathcal{R} computed in regions where the current density exceeds twice its rms value, adds up to more than the total \mathcal{R} over the whole domain while occupying about 20% of the volume of the whole domain (this is possible due to partial cancellation with sites where $\mathcal{R} < 0$). Thus, energy dissipation in this low electron beta turbulent environment is seen to be strongly intermittent, similar to what has been observed in simulations of other collisionless plasma environments (e.g., Wan et al., 2012, 2015; Camporeale et al., 2018).

2.4 Discussion

Observations of the Earth's magnetosheath (Chen and Boldyrev, 2017) and numerical simulations (Roytershteyn et al., 2019) reveal the existence of a new regime of plasma turbulence in the range of scales $d_e^{-1} \ll k_{\perp} \ll \rho_e^{-1}$ in environments with $\beta_e \ll \beta_i \sim 1$. This sub- d_e turbulence is well differentiated from the typical sub- d_i turbulence by its statistical

properties (e.g., magnetic energy spectrum, compressibility). Observations of the magnetic energy spectrum are fit well by theoretical models that describe the turbulence in terms of nonlinear interactions of inertial kinetic Alfvén modes (Chen and Boldyrev, 2017; Passot et al., 2018). However, there was not much separation between d_e and ρ_e in the simulations analyzed and finite gyroradius effects may need to be accounted for to get a better fit with the mangetic compressibility, although the model did reproduce the general trendline. To better study iKAW turbulence, new simulations with lower β_e would be highly desirable.

Our numerical study of this regime of plasma turbulence shows that electron-scale current sheets are naturally generated in this low electron beta environment and a few of them undergo electron-only magnetic reconnection (Vega et al., 2020, 2023b). A comparison between 2.5D simulations with $\beta_e \ll 1$ and $\beta_e \sim 1$ suggests that electron-only reconnection is generated more efficiently in the former (Vega et al., 2020).

In the 3D simulation, the energy dissipation as measured by the pressure-strain interaction was seen to be strongly intermittent, with current sheets representing about 20% of the volume of the whole domain contributing more than 100% of it. One particular reconnection site stood out for representing the most intense dissipation event found in the time slices analyzed, having a peak in the pressure-strain interaction approximately equal to 22 times the rms value at that particular time. This reconnection site was a current structure spanning about 30 field-perpendicular layers and contributed 25% of the pressure-strain interaction in 0.26% of the volume (Vega et al., 2023b). This finding aligns with previous studies that have also demonstrated strong intermittency in energy dissipation in various plasma regimes (e.g., Wan et al., 2012, 2015; Camporeale et al., 2018), highlighting the ubiquity of intermittent structures and dissipation in turbulent plasmas.

3.1 What is a relativistic plasma and why is it important?

It seems pertinent to open this chapter by discussing the meaning of "relativistic plasma". The term can refer to plasmas where the bulk motion is relativistic or where the microscopic particle motion is relativistic (i.e., a relativistically hot plasma). In the simulations of decaying magnetically dominated plasma turbulence without radiation cooling that we analyze here, magnetic fluctuations with energy far exceeding the particle energy are seeded at the initialization and the system is allowed to evolve. We observe that the resulting bulk motion is only mildly relativistic, with root-mean-square velocity $U_{\rm rms} \lesssim c/2$, while the microscopic particle motion is strongly relativistic, with average Lorentz factor $\langle \gamma \rangle \sim 10$ (Vega et al., 2022a,b, 2023a, 2024b).

In the astrophysics community, there is significant interest in relativistic plasma turbulence for its potential as an efficient particle accelerator, but a proper theoretical study of the properties of this turbulent regime is often neglected. However, understanding the properties of relativistic plasma turbulence is an interesting problem in its own right, and is the topic of Vega et al. (2022a) and Vega et al. (2024b), where we use a two-fluid model to derive dynamical equations for the turbulent fluctuations in a relativistic plasma with strong guide field. The model is then compared to the energy spectrum measured in numerical simulations, both in the inertial and kinetic range. We present this work in Section 3.3.

Recent numerical simulations have shown that relativistic plasma turbulence leads to efficient particle energization, which results not only in thermal plasma heating but also in nonthermal acceleration to ultrarelativistic energies, a process manifested in either power-law

¹This situation may be different when radiation loses are present, as part of the kinetic energy of particles is converted into radiation, reducing their relativistic mass and, as a consequence, the inertia of the fluid elements, making it easier to accelerate the latter to highly relativistic speeds.

or log-normal tails of the particle energy distribution function, depending on the strength of the guide field (Zhdankin et al., 2017, 2018b,a, 2019, 2021; Comisso and Sironi, 2018, 2019, 2021; Wong et al., 2020; Nättilä and Beloborodov, 2021; Demidem et al., 2020; Vega et al., 2022b, 2023a, 2024b,a; Chernoglazov et al., 2021; Nättilä and Beloborodov, 2021). In this respect, relativistic plasma turbulence can be considered as a mechanism of particle acceleration complementary to previously studied particle acceleration by collisionless shocks or magnetic reconnection events (e.g., Marcowith et al., 2016; Guo et al., 2020). This regime of plasma turbulence may be present in astrophysical objects, such as jets from active galactic nuclei (e.g., Begelman et al., 1984), pulsar-wind nebulae (e.g., Bühler and Blandford, 2014), and accretion discs (e.g., Yuan and Narayan, 2014), so it may help explain the ubiquitous radiative signatures of nonthermal ultrarelativistic particles in these systems.

In Vega et al. (2022b), we propose a model of stochastic particle energization where particles are accelerated inside spontaneously generated magnetic traps until they escape by pitch angle scattering. The model produces power-law solutions for the tail of the particle energy probability density function (pdf) and the formula derived for the spectral index is a good fit for our numerical simulations with guide field of the same order as the magnetic fluctuations, in the asymptotic limit of strong magnetization (see Comisso and Sironi (2019) and Section 1.6). In Vega et al. (2024b) and Vega et al. (2024a), we show with numerical simulations that in relativistic plasma turbulence with a guide field much stronger than the magnetic fluctuations, particle acceleration leads to a log-normal distribution rather than a power-law in the particle energy pdf. In Vega et al. (2024a), we discuss curvature drift and mirror acceleration as possible energization mechanisms and suggest that which one dominates is what determines what type of distribution the particle energy pdf will evolve into. In view of our analysis of acceleration mechanisms, we offer a reinterpretation of the formula for the power-law spectral index derived in Vega et al. (2022b). We present our work on particle acceleration in Sections 3.4 and 3.5.

In Vega et al. (2023a), we study the spatial distribution of particles in simulations of rela-

tivistic plasma turbulence and observe that ultrarelativistic particles are highly intermittent in space. This could potentially explain the radiation flares observed in astrophysical sources (e.g., Abdo et al., 2011; Tavani et al., 2011) and simulations (e.g., Nättilä and Beloborodov, 2021; Grošelj et al., 2024). This will be the topic of Section 3.6.

3.2 Numerical simulations

We performed simulations of decaying turbulence in an electron-positron plasma with uniform guide field $\mathbf{B_0} = B_0 \hat{\mathbf{z}}$ with the fully relativistic particle-in-cell code VPIC (Bowers et al., 2008), both in 2.5D (two-dimensional domain and three-component vector fields) and in 3D. Let us now define the two magnetization parameters related to the guide field B_0 and the root-mean-square (rms) magnetic fluctuations δB :

$$\sigma = \frac{B_0^2}{4\pi n_0 w m_e c^2}, \quad \tilde{\sigma} = \frac{\delta B^2}{4\pi n_0 w m_e c^2}.$$
 (3.1)

where n_0 denotes the unperturbed number density of electron or positron species, and $n_0wm_ec^2$ is the corresponding enthalpy density. Assuming that the plasma particle distribution is an isotropic Maxwell-Jüttner function with temperature T, the enthalpy per particle is calculated as $w = K_3(1/\theta)/K_2(1/\theta)$, where K_{ν} is the modified Bessel function of the second kind. In this formula, $\theta = k_B T/m_e c^2$ is the normalized temperature.

Denoting the rms value of the *initial* magnetic perturbations as $\delta B_0 = \langle \delta B^2(\boldsymbol{x}, t=0) \rangle^{1/2}$ and the initial enthalpy per particle as w_0 , we define the magnetization parameters at t=0 in our simulations as:

$$\sigma_0 = \frac{B_0^2}{4\pi n_0 w_0 m_e c^2}, \quad \tilde{\sigma}_0 = \frac{\delta B_0^2}{4\pi n_0 w_0 m_e c^2}.$$
 (3.2)

The particle distribution function is initialized with an isotropic Maxwell-Jüttner distribution, with the temperature parameter $\theta_0 = 0.3$. For such an initialization, $w_0 =$

$$K_3(1/\theta_0)/K_2(1/\theta_0) \approx 1.88.$$

Table 3.1 summarizes the parameters of the simulations. The 2.5D simulation domains were double periodic $L \times L$ squares with 100 particles per cell per species. The simulation plane was normal to the mean magnetic field. The 3D domains were triple periodic $L \times L \times L$ cubes with 16 particles per cell per species. However, for the data analysis of the 3D simulations, reduced resolution data was used, with each of the lower resolution cells being eight of the full-resolution cells, leaving the average number of particles per cell at $8 \times 16 = 128$, which is approximately the same as in the 2.5D cases.

Turbulence was seeded by randomly phased magnetic fluctuations of the Alfvénic type

$$\delta \boldsymbol{B}(\boldsymbol{x}) = \sum_{\boldsymbol{k}} \delta B_{\boldsymbol{k}} \hat{\boldsymbol{\xi}}_{\boldsymbol{k}} \cos(\boldsymbol{k} \cdot \boldsymbol{x} + \chi_{\boldsymbol{k}}), \tag{3.3}$$

where χ_k are the random phases and the wave numbers are chosen in the interval $\mathbf{k} = \{2\pi n_x/L, 2\pi n_y/L\}$, with $n_x, n_y = 1, ..., n_{\text{max}}$ for the 2.5D runs, and $\mathbf{k} = \{2\pi n_x/L, 2\pi n_y/L, 2\pi n_y/L\}$, with $n_x, n_y = 1, ..., n_{\text{max}}$, $n_z = 1, 2$ for the 3D runs. The field polarizations correspond to the shear-Alfvén modes (e.g., Lemoine et al., 2016; Demidem et al., 2020), $\hat{\xi}_k = \mathbf{k} \times \mathbf{B}_0/|\mathbf{k} \times \mathbf{B}_0|$, and all the amplitudes δB_k are chosen to be the same.

The simplified 2.5D setup allows us to afford a relatively high numerical resolution of kinetic-range turbulence. Since all the vector components of the electromagnetic field and particle momenta are preserved, it is expected to capture some essential nonlinear interactions existing in the 3D case. Numerical studies involving 2.5D and 3D runs seem to produce similar energy spectra of fields and particles (e.g., Zhdankin et al., 2017, 2018a; Comisso and Sironi, 2018, 2019; Vega et al., 2023a).

Throughout this chapter, time is normalized to the large-scale crossing time l/c, where c is the speed of light and the outer scale of turbulence is evaluated as $l = 2\pi/k (n_{\text{max}}) = L/n_{\text{max}}$, with $n_{\text{max}} = 8$ in the 2.5D runs I through VII and with $n_{\text{max}} = 4$ in small-box 2.5D run VIII and 3D runs IX and X.

Run	Dimension	L/d_e	Resolution (# of cells)	$n_{\rm max}$	σ_0	$\tilde{\sigma}_0$	$(B_0/\delta B_0)^2$	$\omega_{pe}\delta t$
I	2.5D	2010	16640^2	8	0.63	10	1/16	0.04
II	2.5D	2010	16640^2	8	2.5	40	1/16	0.04
III	2.5D	2010	16640^2	8	10	10	1	0.04
IV	2.5D	2010	16640^2	8	40	40	1	0.02
V	2.5D	2010	16640^2	8	90	10	9	0.02
VI	2.5D	2010	16640^2	8	360	40	9	0.02
VII	2.5D	1600	23552^{2}	8	4000	40	100	0.012
VIII	2.5D	200	16640^2	4	4000	40	100	3.5×10^{-4}
IX	3D	1005	2048^{3}	4	40	40	1	0.03
X	3D	1005	2048^{3}	4	80	80	1	0.03

Table 3.1: Summary of the runs.

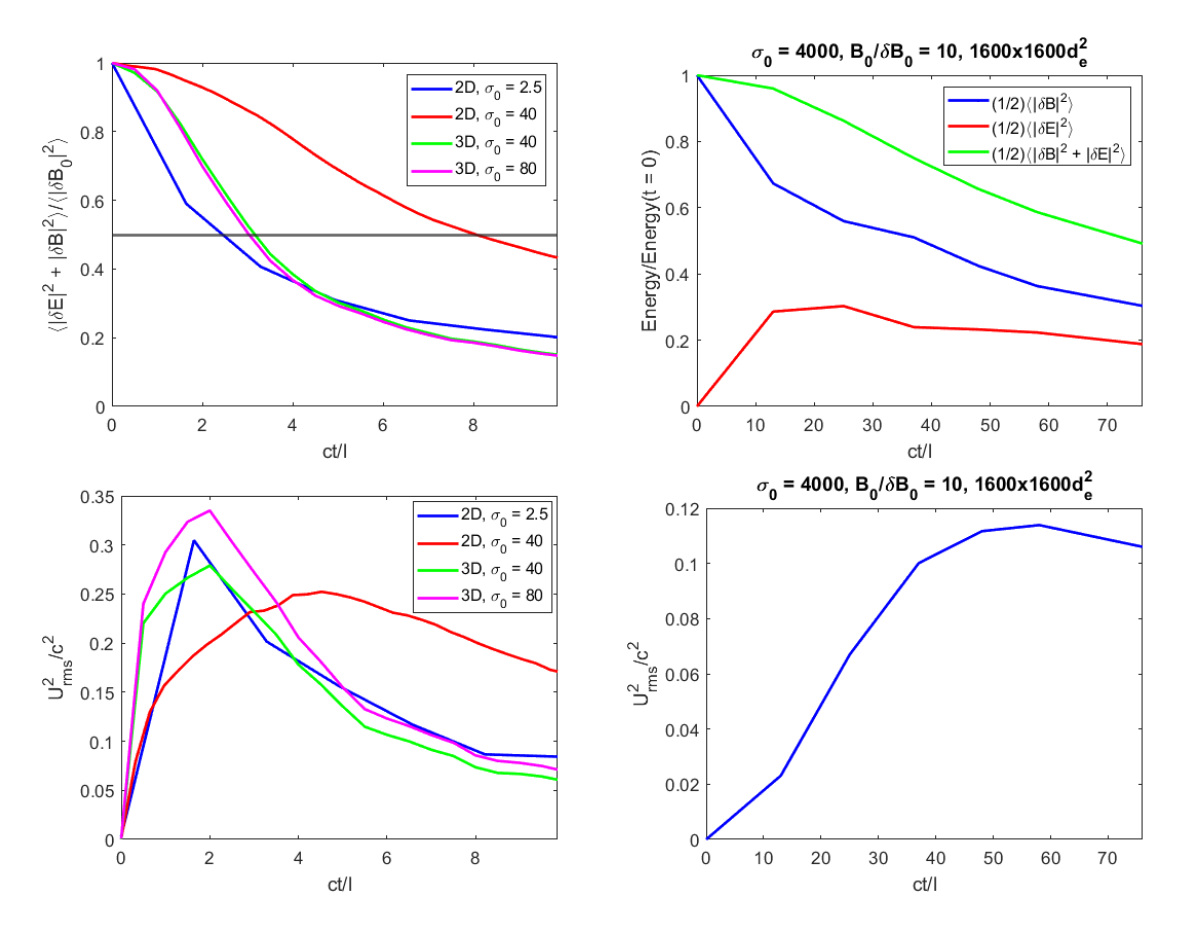


Figure 3.1: Top left: Time evolution of energy in electromagnetic fluctuations normalized to its initial value for runs II, IV, IX, and X, with guide field satisfying $B_0 \lesssim \delta B_0$. The horizontal line is at half the initial energy. Top right: Time evolution of energy in electromagnetic fluctuations normalized to its initial value for run VII, with guide field satisfying $B_0 \gg \delta B_0$. Bottom left: Time evolution of root-mean-square velocity of bulk plasma fluctuations for runs II, IV, IX, and X. Bottom right: Time evolution of root-mean-square velocity of bulk plasma fluctuations for run VII.

Figure 3.1 shows the time evolution of the energy of electromagnetic fluctuations (top row) and of the plasma bulk velocity fluctuations (bottom row) in runs II, IV, VII, IX, and X, spanning cases with strong and weak guide field, as well as 2.5D and 3D. As turbulence evolves, the initial energy of magnetic fluctuations is transferred to the plasma particles. Since in our numerical setup the initial magnetic energy significantly exceeds the kinetic energy of the particles, by the time the field energy declines by half, the particles become significantly heated and their kinetic energy becomes comparable to the energy of electromagnetic fluctuations. At approximately the same time, the bulk plasma fluctuations relax to the subsonic velocities $U_{\rm rms} \lesssim c/\sqrt{3}$, in agreement with the phenomenological discussion in Section 3.6, and the turbulence reaches a quasi-steady state described by universal statistical characteristics such as fluctuations spectra and particle energy distribution functions. We perform our statistical analysis after this initial relaxation is completed.

3.3 Turbulence in strongly magnetized relativistic plasmas

The discussion in this section will be largely based on Vega et al. (2022a, 2024b). We will consider a strongly magnetized, magnetically dominated electron-positron plasma, $1 \ll \tilde{\sigma} \ll \sigma$. As turbulence evolves, electromagnetic fluctuations efficiently heat the plasma, so the temperature becomes ultrarelativistic while, simultaneously, $\tilde{\sigma}$ decreases. This reflects the fact that relativistic turbulent motion is inherently compressible, which allows colliding fluid elements to convert their kinetic energy into heat rapidly (Zhdankin et al., 2018a; Nättilä and Beloborodov, 2021; Vega et al., 2022b, 2023a). We will therefore analyze the case when plasma bulk fluctuations are nonrelativistic, while plasma temperature is ultrarelativistic.²

²While the idealized assumption of the ultrarelativistic equation of state simplifies the formulae, it is not crucial for our analytic discussion. For mildly relativistic particle distributions, $\theta \sim 1$, such as, for instance, those obtained as pair-creation-annihilation equilibria (Svensson, 1982), one needs to add the rest-mass term to the normalized enthalpy, $w \to w + 1$, in the expression for the relativistic inertial scale $d_{\rm rel}$, and use the general equation of state in the expression for the acoustic velocity, v_S .

Dynamical equations of Alfvén modes

Consider the nonrelativistic bulk motion of a relativistically hot collisionless plasma with temperature $T_s \gg m_s c^2$, where $s = \{e, i\}$ denotes the particle species. The momentum equation takes the form (e.g., Mihalas and Mihalas, 1999):

$$\frac{\partial \boldsymbol{U}_s}{\partial t} + (\boldsymbol{U}_s \cdot \boldsymbol{\nabla}) \, \boldsymbol{U}_s = \frac{-\boldsymbol{\nabla} \cdot \boldsymbol{P}_s}{\epsilon_s/c^2} + \frac{n_s q_s}{\epsilon_s/c^2} \left[\boldsymbol{E} + \frac{\boldsymbol{U}_s}{c} \times \boldsymbol{B} \right], \tag{3.4}$$

where $\epsilon_s = n_s m_s c^2 + u_s + 2P_{s,\perp} + P_{s,\parallel}$ is the enthalpy density, n_s is the particle number density, u_s is the internal energy density, and $P_s \approx \operatorname{diag}(P_{s,\perp}, P_{s,\perp}, P_{s,\parallel})$ is the pressure of the particles. If we assume isotropic pressure, $P_{s,\perp} = P_{s,\parallel} = P_s$, the enthalpy is $\epsilon_s \approx u_s + P_s \approx (4/3)u_s$, where we used that for ultrarelativistic temperature the energy-momentum tensor is traceless, so $u_s = 3P_s$. In our simulations with $\tilde{\sigma} \ll \sigma$ (or $B_0/\delta B \gg 1$) we saw strong pressure anisotropy, $P_{s,\parallel} \gg P_{s,\perp}$, so $u_s = P_{s,\parallel}$ and $\epsilon_s \approx 2u_s$. In addition, one can assume some equation of state, for instance, the adiabatic law of relativistically hot plasma, $P_s \propto n_s^{4/3}$ for isotropic pressure and $P_{s,\parallel} \propto n_s^2$ if $P_{s,\parallel} \gg P_{s,\perp}$.

We are interested in Alfvénic plasma fluctuations that are relatively low frequency as compared to cyclotron frequencies, $\omega \ll \Omega_s/\gamma_s$, where γ_s is the typical gamma factor of particle thermal motion and Ω_s is the nonrelativistic gyrofrequency. We also impose a self-consistent assumption that the Fourier spectra of the fields are anisotropic in the Fourier space with respect to the background magnetic field \mathbf{B}_0 , $k_{\parallel} \ll k_{\perp}$, and the fluctuations obey the critical balance condition $\delta B/B_0 \sim k_{\parallel}/k_{\perp} \ll 1$ (e.g., Goldreich and Sridhar, 1995).

The following derivation is analogous to the procedure developed for the nonrelativistic case (e.g., Chen and Boldyrev, 2017; Loureiro and Boldyrev, 2018; Boldyrev et al., 2021; Milanese et al., 2020). As follows from the field-perpendicular component of the momentum equation, to the leading order in the small parameter $\omega \gamma_s/\Omega_s$ the particle motion is the $\mathbf{E} \times \mathbf{B}$ drift, while to the next order it is the polarization drift (compare to the nonrelativistic case,

formula (2.10),

$$U_{s,\perp} = v_E + \frac{\epsilon_s}{n_s q_s B^2 c} B \times \frac{d_E}{dt} v_E, \qquad (3.5)$$

where $\mathbf{v}_E = c(\mathbf{E} \times \mathbf{B})/B^2$ and the time derivative is $d_E/dt \equiv \partial/\partial t + \mathbf{v}_E \cdot \nabla$. The field-parallel component of the velocity field is expressed through the parallel electric current, $U_{s,\parallel} = J_{s,\parallel}/(n_s q_s)$. Moreover, \mathbf{v}_E can be written

$$\frac{\mathbf{v}_E}{c} = \frac{\hat{\mathbf{z}} \times \nabla \phi}{B_0} + \frac{\mathbf{E}_{\text{sol}} \times \hat{\mathbf{z}}}{B_0},\tag{3.6a}$$

$$c\nabla \times \mathbf{E}_{\text{sol}} = -\partial_t \delta \mathbf{B}. \tag{3.6b}$$

where $\boldsymbol{E} = -\boldsymbol{\nabla}\phi + \boldsymbol{E}_{\mathrm{sol}}$ and ϕ is the electric potential (see Section 2.1).

Substituting (3.5) and (3.6) into the continuity equation,

$$\frac{\partial n_s}{\partial t} + \nabla_{\perp} \cdot (n_s U_{s,\perp}) + \nabla_{\parallel} (n_s U_{s,\parallel}) = 0, \tag{3.7}$$

we obtain, to the leading order in magnetic, electric, and density fluctuations

$$\frac{\partial}{\partial t} \left(\frac{\delta n_s}{n_0} - \frac{\delta B_z}{B_0} - \frac{\epsilon_{s,0}}{n_0 q_s B_0^2} \nabla_{\perp}^2 \phi \right)
+ \frac{1}{B_0} \left(\hat{\boldsymbol{z}} \times \boldsymbol{\nabla} \phi \right) \cdot \boldsymbol{\nabla} \left(\frac{\delta n_s}{n_0} - \frac{\delta B_z}{B_0} - \frac{\epsilon_{s,0}}{n_0 q_s B_0^2} \nabla_{\perp}^2 \phi \right) + \frac{1}{n_0 q_s} \nabla_{\parallel} J_{s,\parallel} = 0.$$
(3.8)

In this equation, n_0 is the unperturbed density of each species and $\delta n_s = n_s - n_0$ is the corresponding density perturbation. The parallel gradient is taken along the direction of the magnetic field, $\nabla_{\parallel} = \partial/\partial z - \frac{1}{B_0}(\hat{z} \times \nabla A_z) \cdot \nabla$, where the field-perpendicular magnetic perturbation is expressed as $\delta \mathbf{B}_{\perp} = -\hat{z} \times \nabla A_z$.

In order to find the electric current, we turn to the magnetic-field-parallel component of

³We did not include the diamagnetic drift proportional to $\hat{z} \times \nabla \cdot P_s$ in the perpendicular velocity (3.5), since such a drift does not lead to particle transport and should not contribute to the continuity equation.

the momentum equation:

$$\frac{\partial U_{s,\parallel}}{\partial t} + (\boldsymbol{v}_E \cdot \boldsymbol{\nabla}_{\perp}) \, \boldsymbol{U}_{s,\parallel} = -\frac{\nabla_{\parallel} P_{\parallel}}{\epsilon_s / c^2} + \frac{n_s q_s}{\epsilon_s / c^2} E_{\parallel}. \tag{3.9}$$

We now multiply each of the Equations (3.8) and (3.9) by n_0q_s and sum over particle species. As a result, Equation (3.8) turns into the charge conservation law:

$$\frac{\partial}{\partial t} \left(\rho - \frac{2\epsilon_0}{B_0^2} \nabla_{\perp}^2 \phi \right) + \frac{1}{B_0} \left(\hat{\boldsymbol{z}} \times \boldsymbol{\nabla} \phi \right) \cdot \boldsymbol{\nabla} \left(\rho - \frac{2\epsilon_0}{B_0^2} \nabla_{\perp}^2 \phi \right) + \nabla_{\parallel} J_{\parallel} = 0, \tag{3.10}$$

where $\rho = q_i \delta n_i + q_e \delta n_e$ is the electric charge density, $J_{\parallel} = J_{e,\parallel} + J_{i,\parallel}$ is the parallel current, and $\epsilon_0 = (\epsilon_{i,0} + \epsilon_{e,0})/2$ is the mean unperturbed enthalpy. To simplify the formulae, we have assumed without loss of generality that $q_i = |q_e| \equiv q$. We may also assume that in the ultrarelativistic case, the unperturbed enthalpy is the same for both species, $\epsilon_{i,0} = \epsilon_{e,0} = \epsilon_0$. In the ultrarelativistic limit with $P_{\parallel}/P_{\perp} \gg 1$, $\epsilon_0 = 2P_{\parallel,0}$, where $P_{\parallel,0} = (P_{i\parallel,0} + P_{e\parallel,0})/2$. We will assume that the unperturbed pressure is the same for both species, so $P_{\parallel,0} = P_{i\parallel,0} = P_{e\parallel,0}$. The parallel momentum equation (3.9) then leads to

$$\frac{\partial J_{\parallel}}{\partial t} + (\boldsymbol{v}_E \cdot \boldsymbol{\nabla}_{\perp}) J_{\parallel} = \frac{-q n_0 c^2}{\epsilon_0} \nabla_{\parallel} \delta P_{\parallel} + \frac{2 n_0^2 c^2 q^2}{\epsilon_0} E_{\parallel}, \tag{3.11}$$

where $\delta P_{\parallel} = \delta P_{\parallel,i} - \delta P_{\parallel,e}$ denotes the pressure imbalance.

We note that the terms containing the electric charge density ρ and pressure imbalance δP_{\parallel} in Equations (3.10) and (3.11) reflect deviation of plasma fluctuations from quasineutrality, that is, from the condition $\delta n_i = \delta n_e$. It is easy to see by using Gauss's law, $-\nabla^2 \phi = 4\pi \rho$, that these terms are relatively small in the case of weak magnetization, that is, when $\sigma \sim B_0^2/(8\pi\epsilon_0) \ll 1$. In the opposite case of strong magnetization that we consider in this work, the deviation from quasineutrality is essential and as a result, both the electric charge and pressure imbalance become dynamically significant. In the case of a nonrelativistic electron-proton plasma, we need to replace $\epsilon_0 \to n_0 m_i c^2/2$, and the magnetization parameter

turns into the so-called quasineutrality parameter, $\Omega_i^2/\omega_{pi}^2 = \lambda_i^2/\rho_i^2$. Here, λ_i is the ion Debye scale, ρ_i is the gyroscale, and ω_{pi} is the ion plasma frequency. Therefore, Ω_i^2/ω_{pi}^2 is the nonrelativistic analog of relativistic magnetization σ .

To close system (3.10)-(3.11), we replace the charge density by using Gauss's law, $\rho = -(1/4\pi)\nabla_{\perp}^2\phi$, express the parallel electric current as $J_{\parallel} = -(c/4\pi)\nabla_{\perp}^2A_z$, and use the adiabatic law for each particle species to evaluate the pressure gradients:

$$\nabla_{\parallel} \delta P_{\parallel} = \left(1 + \frac{v_S^2}{c^2}\right) \frac{P_{\parallel,0}}{n_0} \nabla_{\parallel} \left(\delta n_i - \delta n_e\right) = -\frac{v_S^2}{c^2} \frac{\epsilon_0}{n_0} \frac{1}{4\pi q} \nabla_{\parallel} \nabla_{\perp}^2 \phi. \tag{3.12}$$

where we have introduced the speed of sound $v_S^2 = c^2 \partial P_{\parallel}/\partial u|_0$. Finally, we introduce the new variables for the scalar and vector potentials, $\tilde{\phi} = \phi c/B_0$, $\tilde{A}_z = A_z c/\left(B_0\sqrt{1+2/\sigma}\right)$. Substituting these expressions into Equations (3.10) and (3.11), we finally obtain the system of equations describing Alfvén dynamics of a relativistic plasma in both magnetohydrodynamic and inertial regimes:

$$\frac{\partial}{\partial t} \nabla_{\perp}^{2} \tilde{\phi} + \left(\hat{z} \times \nabla_{\perp} \tilde{\phi}\right) \cdot \nabla_{\perp} \nabla_{\perp}^{2} \tilde{\phi} = -v_{A} \nabla_{\parallel} \nabla_{\perp}^{2} \tilde{A}_{z}, \tag{3.13}$$

$$\frac{\partial}{\partial t} \left(\tilde{A}_z - d_{\text{rel}}^2 \nabla_{\perp}^2 \tilde{A}_z \right) - \left(\hat{z} \times \nabla_{\perp} \tilde{\phi} \right) \cdot \nabla_{\perp} d_{\text{rel}}^2 \nabla_{\perp}^2 \tilde{A}_z = -v_A \nabla_{\parallel} \left(\tilde{\phi} - \frac{v_S^2}{c^2} d_{\text{rel}}^2 \nabla_{\perp}^2 \tilde{\phi} \right), \quad (3.14)$$

where

$$v_A = \frac{c}{\sqrt{1 + 2/\sigma}} \approx c \tag{3.15}$$

is the relativistic Alfvén speed in a pair plasma,

$$d_{\rm rel}^2 = \frac{\epsilon_0 c^2}{2\omega_{pe}^2} = \frac{\epsilon_0 m_e c^2}{8\pi n_0 e^2}$$
 (3.16)

⁴Note that if $P_{s,\parallel} \propto n_s^a$, then $a=1+v_S^2/c^2$. For an isotropic plasma, $v_S^2/c^2=1/3$, so a=4/3. If $P_{s,\parallel} \gg P_{s,\perp}$, $v_S^2/c^2=1$ and a=2.

is the relativistic inertial scale, and the magnetic-field-parallel gradient is given by

$$\nabla_{\parallel} = \partial/\partial z - \frac{1}{v_A} (\hat{z} \times \nabla_{\perp} A_z) \cdot \nabla_{\perp}. \tag{3.17}$$

Except for the very last term in Equation (3.14) describing the relativistic pressure contribution, the system of equations (3.13) and (3.14) is analogous to the nonrelativistic case. The nonrelativistic electron-ion case is recovered by replacing the Alfvén speed and the inertial length by their nonrelativistic counterparts using the substitutions $\epsilon_0 \to n_0 m_i c^2/2$ in the Alfvén velocity and $\epsilon_0 \to 2n_0 m_e c^2$ in the inertial length. It may also be instructive to compare the dispersion relation (3.18) with the dispersion relation of nonrelativistic inertial kinetic Alfvén waves (e.g., Streltsov and Lotko, 1995; Lysak and Lotko, 1996; Boldyrev et al., 2021, Equation 19), where, similarly, the kinetic correction coming from thermal particle motion enters the numerator, while the inertial correction appears in the denominator. In our relativistic case, these two corrections are necessarily of the same order. We also note that, similarly to the previous study (TenBarge et al., 2021), at large scales $k_{\perp}^2 d_{\rm rel}^2 \ll 1$, Equations (3.13) and (3.14) describe shear Alfvén waves in a relativistically hot plasma and they are mathematically analogous to the equations of reduced magnetohydrodynamics. Available fluid and first-principle particle-in-cell kinetic simulations of relativistic turbulence at such scales (e.g., Zrake and MacFadyen (2012); Zhdankin et al. (2018a); Chernoglazov et al. (2021); Vega et al. (2022b,a); see also next subsection) indeed produce the energy spectra consistent with the spectrum of nonrelativistic Alfvén turbulence (e.g., Boldyrev, 2006; Boldyrev et al., 2009; Mason et al., 2006, 2012; Perez et al., 2012; Tobias et al., 2013; Chandran et al., 2015; Chen, 2016; Kasper et al., 2021).

The dispersion relation of the linear waves described by Equations (3.13) and (3.14) is

$$\omega^2 = k_z^2 v_A^2 \frac{1 + (v_S^2/c^2) k_\perp^2 d_{\text{rel}}^2}{1 + k_\perp^2 d_{\text{rel}}^2},$$
(3.18)

which can be termed relativistic inertial Alfvén waves. Similarly to the kinetic-Alfvén waves,

the numerator of this expression involves the contribution of the thermal effects. Similarly to the inertial Alfvén waves, the denominator includes the contribution of the electron (and positron) inertia. This is somewhat analogous to the inertial kinetic-Alfvén modes in a nonrelativistic plasma (e.g., Streltsov and Lotko, 1995; Lysak and Lotko, 1996; Chen and Boldyrev, 2017; Roytershteyn et al., 2019; Loureiro and Boldyrev, 2018; Boldyrev et al., 2021). In contrast with the nonrelativistic case, however, in a relativistic plasma, we have $v_S \sim c$, so that the thermal contribution in the numerator is never negligible. Rather, the thermal and inertial effects in Equation (3.18) are necessarily of the same order. Since $v_A \approx c$, the phase velocity of relativistic inertial Alfvén waves is close to the speed of sound, itself comparable to the thermal speed, so Landau damping of the linear modes is also generally strong at $k_\perp^2 d_{\rm rel}^2 \gtrsim 1$. As discussed in Appendix A, the applicability of the linear dispersion relation in Equation (3.18) depends on the particle distribution function, which is strongly nonthermal.

Finally, as can be checked directly, Equations (3.13) and (3.14) conserve two quadratic integrals:

$$\mathcal{E} = \frac{B_0^2}{8\pi v_A^2} \int \left[\left(\nabla_\perp \tilde{A}_z \right)^2 + d_{\text{rel}}^2 \left(\nabla_\perp^2 \tilde{A}_z \right)^2 + \left(\nabla_\perp \tilde{\phi} \right)^2 + \frac{v_s^2}{c^2} d_{\text{rel}}^2 \left(\nabla_\perp^2 \tilde{\phi} \right)^2 \right] d^3 x, \qquad (3.19a)$$

$$H = \frac{\sqrt{\epsilon_0}}{c} \int \nabla_{\perp}^2 \tilde{\phi} \left(\tilde{A}_z - d_{\text{rel}}^2 \nabla_{\perp}^2 \tilde{A}_z \right) d^3 x.$$
 (3.19b)

Turbulence in the inertial range

In the hydrodynamic range of scales, $k_{\perp}^2 d_{\rm rel}^2 \ll 1$, the energy integral becomes:

$$\mathcal{E} = \frac{B_0^2}{8\pi v_A^2} \int \left[(\nabla_\perp \tilde{A}_z)^2 + (\nabla_\perp \tilde{\phi})^2 \right] d^3 x = \int \left[\frac{(\delta B)^2}{8\pi} + \frac{E^2}{8\pi} + \epsilon_0 \frac{v_E^2}{c^2} \right] d^3 x, \tag{3.20}$$

where in the second expression, we have restored the corresponding physical fields. The term $\epsilon_0 \frac{v_E^2}{c^2}$, which came from the $2/\sigma$ term hidden in the $1/v_A^2$ factor, can be interpreted as the kinetic energy. We see that the ratio of the electric to kinetic energy is given by the parameter $\frac{E^2}{8\pi} / \left(\epsilon_0 \frac{v_E^2}{c^2}\right) = B_0^2/(8\pi\epsilon_0) \sim \sigma$. In both relativistic and nonrelativistic cases, when $\sigma \gg 1$,

the charge fluctuations are significant and the electric energy dominates the kinetic energy. Therefore, the energy of fluctuations is mostly contained in magnetic and electric fields. This had already been hinted at in the previous subsection, where significant deviations from quasineutrality were noted. Figure 3.2 illustrates how the electric fluctuations gradually approach the magnetic fluctuations as σ_0 increases until the two are in approximate energy equipartition.

In this limit, the system of Equations (3.13) and (3.14) is mathematically analogous to the equations of nonrelativistic reduced magnetohydrodynamics, with the only difference that in the magnetically dominated case, the field ϕ in these equations should be associated with the intensity of electric rather than kinetic fluctuations. Based on this analogy, we may conjecture that the spectrum of the total energy of relativistic magnetically dominated plasma turbulence, the spectrum of its residual energy, and the alignment angle of turbulent fluctuations, should be similar to their reduced MHD counterparts when reinterpreted in terms of magnetic and electric fields. Here, we compare these predictions against runs V and VI in Table 3.1.

In Figure 3.3, we present the spectra of magnetic and electric fluctuations as well as the total energy spectrum, $W_{k_{\perp}} = |B_{k_{\perp}}|^2 + |E_{k_{\perp}}|^2$. The phase-volume compensated scaling of the energy spectrum in the magnetohydrodynamic interval of scales $k_{\perp}^2 d_{\rm rel}^2 \ll 1$ is close to $W_{k_{\perp}} 2\pi k_{\perp} \propto k_{\perp}^{-3/2}$. Such a spectrum is expected in nonrelativistic magnetohydrodynamic turbulence (e.g., Boldyrev, 2006; Boldyrev et al., 2009; Mason et al., 2006, 2012; Perez et al., 2012; Tobias et al., 2013; Chandran et al., 2015; Chen, 2016; Kasper et al., 2021), where the energy is contained in magnetic and kinetic fluid fluctuations. We see that it also holds in relativistic collisionless plasma turbulence dominated by magnetic and electric fields. Our result is also consistent with the recent relativistic MHD studies (TenBarge et al., 2021; Chernoglazov et al., 2021). The kinetic scale cascade will be discussed in the next subsection.

In nonrelativistic magnetohydrodynamic turbulence, the magnetic energy is known to exceed the energy of kinetic fluctuations. Phenomenological and numerical considerations

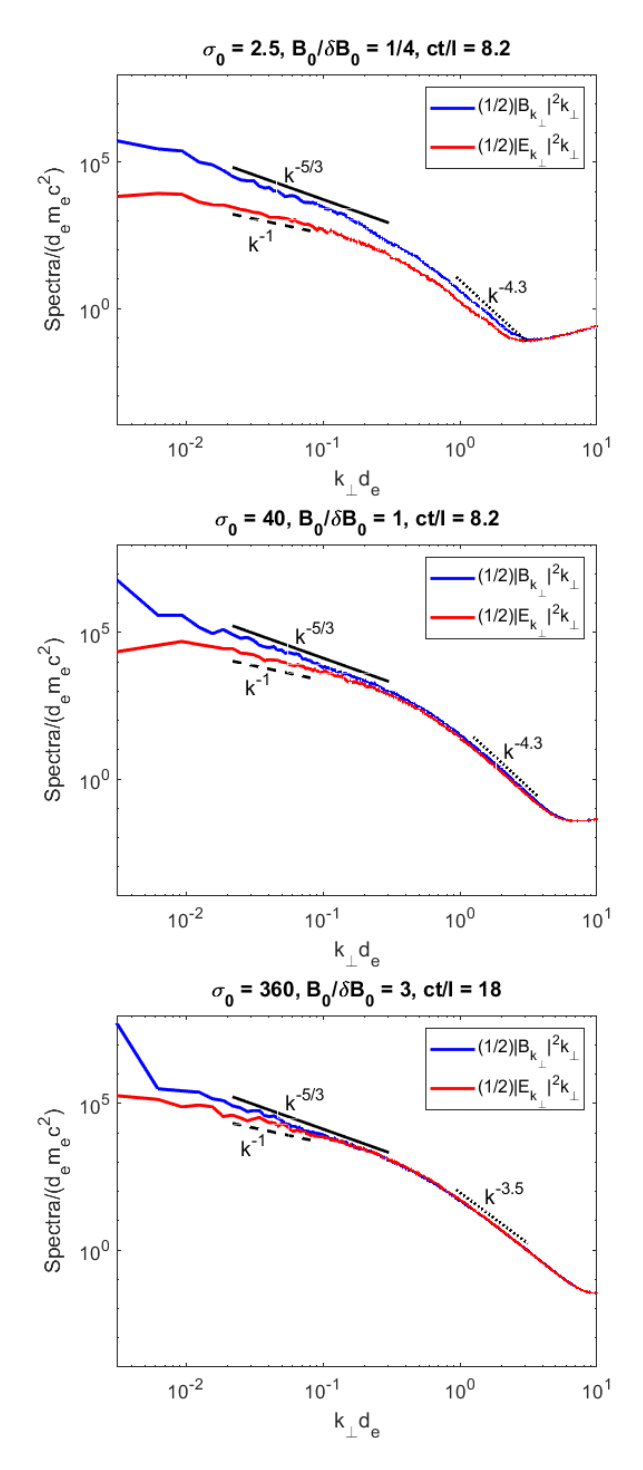


Figure 3.2: Electric and magnetic energy spectra of runs II (top), IV (middle), and VI (bottom). The sequence from the top to the bottom illustrates the growing deviation from quasineutrality as σ_0 increases.

demonstrated that the difference between the magnetic and kinetic energies, the so-called residual energy, is positive and has a spectral index close to -2 (e.g., Boldyrev et al., 2011,

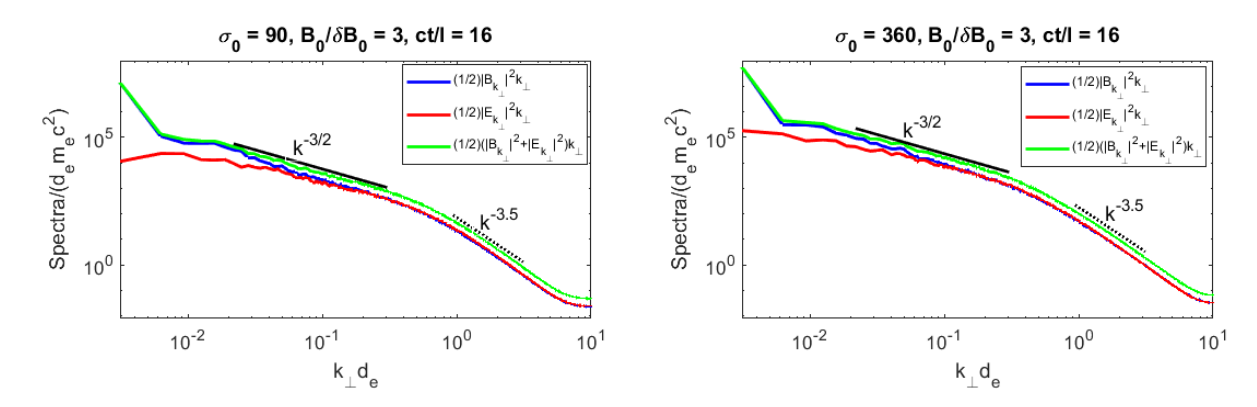


Figure 3.3: The magnetic and electric spectra, and the total electromagnetic energy spectrum, for two different magnetizations. The total energy spectrum approaches a $k^{-3/2}$ power-law at $k_{\perp}d_{e} \ll 1$, and a $k^{-3.5}$ power-law at $k_{\perp}d_{e} \gg 1$.

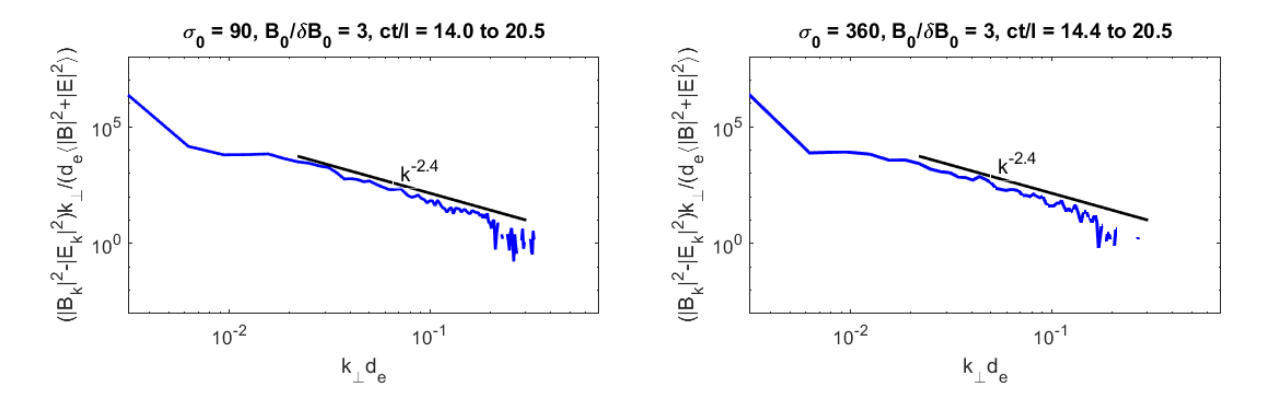


Figure 3.4: The spectra of the normalized residual energy for two different magnetizations, averaged over nine data cubes covering the indicated intervals of turn-over times. The solid lines are shown for the reader's reference.

2012; Chen et al., 2013a). In the relativistic magnetically dominated case, we may introduce the analog of residual energy as the difference between the magnetic and electric energies, $R_{k_{\perp}} = |B_{k_{\perp}}|^2 - |E_{k_{\perp}}|^2$. This quantity is measured in Figure 3.4. To compensate for the overall energy decline in decaying turbulence we have normalized the residual energy by the total energy of fluctuations and then averaged over several data cubes. A power-law spectrum is indeed observed, but the scaling is slightly steeper than in its nonrelativistic counterpart, more consistent with $R_{k_{\perp}} 2\pi k_{\perp} \propto k_{\perp}^{-2.4}$.

Finally, a characteristic feature of nonrelativistic plasma turbulence in the presence of a strong guide field, is the dynamic alignment between the shear-Alfvén magnetic and velocity

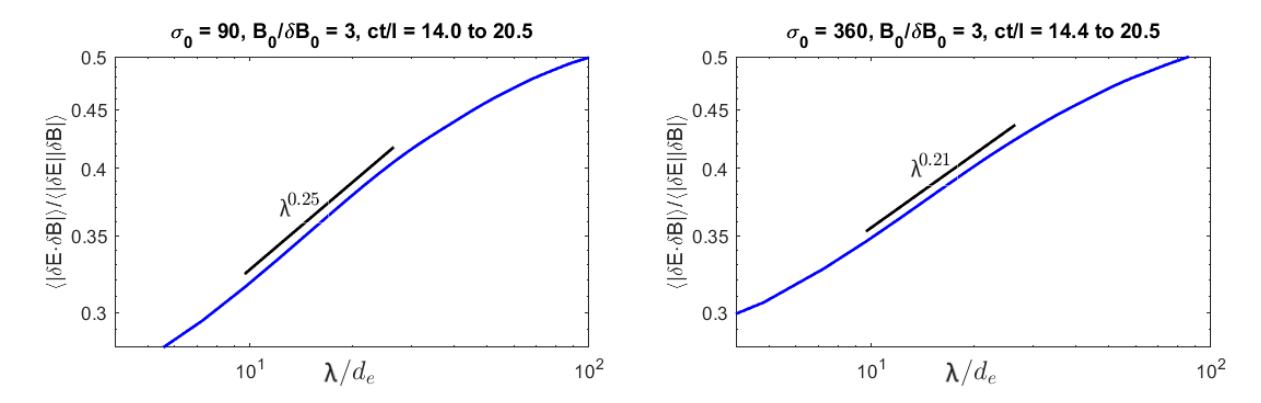


Figure 3.5: The cosine of the alignment angle φ_{λ} between the magnetic and electric fluctuations in numerical simulations. The results are averaged over nine data cubes covering the indicated time intervals. The straight lines are shown for reference.

fluctuations. As mentioned in Section 1.3, such fluctuations become spontaneously aligned in a turbulent cascade, with the alignment angle scaling as $\sin \theta_{\lambda} \propto \lambda^{1/4}$, where λ is the field-perpendicular scale, (e.g., Boldyrev, 2006; Podesta et al., 2009; Chen et al., 2011; Perez et al., 2012). Such an alignment progressively reduces the strength of nonlinear interaction at small scales, which arguably explains the shallower-than-Kolmogorov spectrum of turbulent energy, $k_{\perp}^{-3/2}$. In the case of magnetically-dominated turbulence, one may similarly expect a scale-dependent dynamic alignment between the electric and magnetic field fluctuations,

$$\cos \varphi_{\lambda} = \frac{\langle |\delta \mathbf{E} \cdot \delta \mathbf{B}| \rangle}{\langle |\delta \mathbf{E}| |\delta \mathbf{B}| \rangle}, \tag{3.21}$$

where λ is the scale of the fluctuations in the field-perpendicular plane, e.g., $\delta \mathbf{B} \equiv \mathbf{B}(\mathbf{x} + \mathbf{\lambda}) - \mathbf{B}(\mathbf{x})$ where $\mathbf{\lambda} \perp \mathbf{B}_0$. To see whether a similar alignment exists in our numerical simulations of collisionless relativistic turbulence, we plot the cosine of the angle φ_{λ} vs scale λ in Figure 3.5. We observe a scaling close to that of the nonrelativistic case, and also to the relativistic MHD case (Chernoglazov et al., 2021). We however notice that the scaling varies slightly with the plasma magnetization parameter σ_0 ; it is slightly shallower in the case of stronger magnetization, possibly reflecting a shorter inertial range due to a larger relativistic inertial scale.

Kinetic scale turbulence

At kinetic scales, $1/d_{\rm rel}^2 \ll k_\perp^2 \ll 1/\rho_e^2$, the inertial Alfvén waves are transformed into $\omega^2 = \frac{v_S^2}{c^2} k_z^2 v_A^2$, while the integral (3.19a) takes the form:

$$\mathcal{E} = \frac{B_0^2 d_{\text{rel}}^2}{8\pi v_A^2} \int \left[\left(\nabla_\perp^2 \tilde{A}_z \right)^2 + \frac{v_S^2}{c^2} \left(\nabla_\perp^2 \tilde{\phi} \right)^2 \right] d^3 x. \tag{3.22}$$

This quantity is expected to cascade in a Fourier space toward large wavenumbers, somewhat analogously to the enstrophy cascade in 2D incompressible hydrodynamic turbulence (Kraichnan, 1967). Such a cascade is however only marginally local, so it depends on the conditions at the low-k boundary of the inertial interval. For a given field-perpendicular length λ , the amplitude of the linear modes of equations (3.13) and (3.14) satisfy $\tilde{A}_{z,\lambda} \sim \tilde{\phi}_{\lambda}$, and the nonlinear interaction time can be estimated from these equations as $\tau_{\lambda} \sim \lambda^2/\tilde{\phi}_{\lambda}$. The condition of constant flux of \mathcal{E} then reads $\tilde{\phi}_{\lambda}^2/(\lambda^4\tau_{\lambda}) = \text{const}$, which gives for the scaling of fluctuations $\tilde{\phi}_{\lambda} \propto \lambda^2$ and for the electromagnetic energy spectrum of relativistic inertial Alfvén waves

$$W_{k_{\perp}} 2\pi k_{\perp} \propto k_{\perp}^{-3}. \tag{3.23}$$

The nonlinear interaction time for such modes turns out to be independent of scale, which implies that for the critically balanced cascade, $\omega \propto 1/\tau_{\lambda}$, we have $k_z \propto \text{const}$, that is, the cascade proceeds in the field-perpendicular direction.

Similarly to the hydrodynamic case, the energy cascade is expected to have intermittency corrections that lead to a steeper energy spectrum,

$$W_{k_{\perp}} dk_{\perp} \propto k_{\perp}^{-3} \ln^{-1/3}(k/k_0) dk_{\perp}.$$
 (3.24)

Here, k_0 is the large-scale boundary of the spectrum, which approximately corresponds to the inverse electron inertial scale. The intermittency correction reflects the non-locality of turbulence. The electromagnetic energy spectrum close to k_{\perp}^{-3} implies that vorticity and current structures at scales $k_{\perp} \gg k_0$ are strained most efficiently by turbulent eddies at scales k_0 (e.g., Boffetta and Ecke, 2012).

As we mentioned before, significant Landau damping may affect relativistic Alfvén turbulence at kinetic scales. We, however, conjecture that as a consequence of the non-locality of turbulence, the spectrum should exhibit a near power-law behavior, close to that given by Equations (3.23) and (3.23). Indeed, the Kraichnan spectrum is established due to gradient-stretching of small-scale structures by turbulent eddies of the scale $k_0 \sim 1/d_{\rm rel}$. As a result, all small-scale modes have the same evolution time and the same parallel phase velocity. A particle resonating with structures of scales $k_{\perp} \gg 1/d_{\rm rel}$ then essentially resonates with an entire eddy of scale $k_0 \sim 1/d_{\rm rel}$. Landau damping may therefore regulate the overall intensity of kinetic-scale fluctuations, while not significantly affecting their spectrum. Our numerical results analyzed below seem to be consistent with this prediction.

Since the kinetic range of scales is not well resolved in runs V and VI (only 8 cells per nonrelativistic d_e), to better study the kinetic cascade we performed simulations VII and VIII. Run VII is a large-box, high-resolution simulation that spans both hydrodynamic and kinetic scales, with about 15 cells per nonrelativistic d_e . Run VIII is a small-box simulation where the number of cells per nonrelativistic d_e was increased to 80, drastically improving the resolution of the sub- d_e fluctuations while decreasing the hydrodynamic range.

In the large-box run VII, an initial plasma current is also added to the system to compensate for the curl of the initial magnetic perturbations, $J_z = (c/4\pi)\nabla \times \delta B_0$. This helps to avoid the generation of high-frequency ordinary modes with non-zero E_z in addition to the low-frequency Alfvén modes. To add the current, the initial plasma density n_0 is kept uniform, and velocity $U_z^s = J_z/(2q_sn_0)$ is added to each particle of species s with charge $q_s = \pm e$ (positrons and electrons) sampled from the Maxwell-Jüttner distribution, provided $|v_z^s + U_z^s| < c$. The distribution is unchanged in the region where $|v_z^s + U_z^s| > c$. The addition of such a current does not change the core of the particle distribution function but modifies

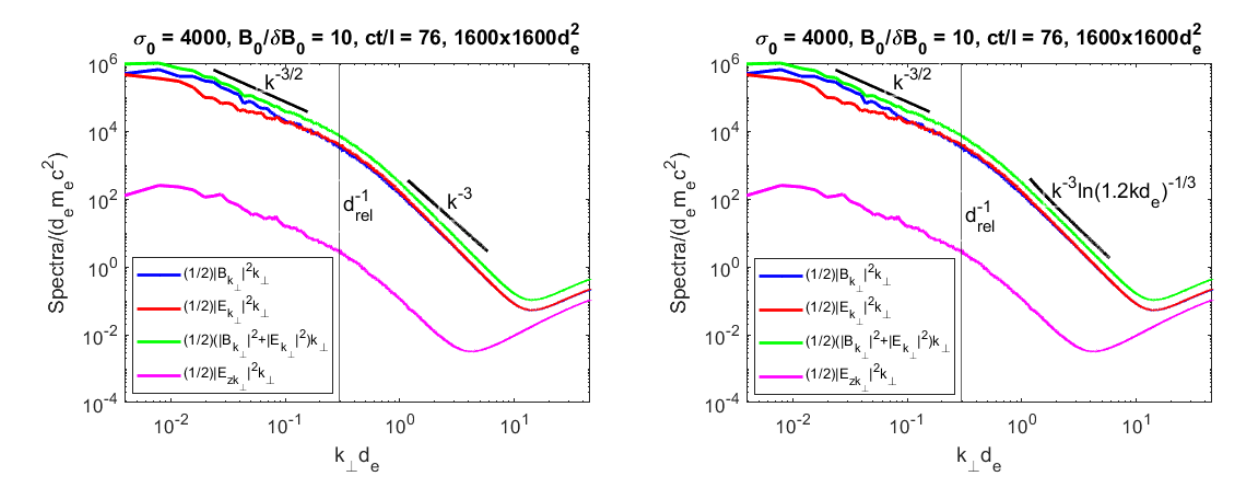


Figure 3.6: Spectra of electric and magnetic fluctuations in the large-box run VII. The total energy spectrum is slightly steeper than k^{-3} , but is consistent with the spectrum including a logarithmic intermittency correction, cf. Equations (3.23) and (3.24).

its high-energy tail, as will be seen in the next section.

In the small-box run VIII, the addition of a compensating current is less practical, since it would formally require the electron velocities to exceed the speed of light in more cells. We do observe the generation of a weak ordinary mode in this case. The presence or absence of the initial compensating current, however, does not qualitatively affect the particle distribution function and the spectra of Alfvénic fluctuations eventually generated by the developed turbulence.

The energies of electric and magnetic fluctuations in the large-box run are shown in Figure 3.6. The total energy spectrum is slightly steeper than k_{\perp}^{-3} , however, it is consistent with the Kraichnan spectrum of turbulence including a logarithmic intermittency correction, in agreement with Equation (3.24). We find that $k_0^{-1} = 1.2 d_e$ provides a good match. Also, as we mentioned before, Landau damping may play a role in the steepening of the spectrum.

The electric and magnetic energy spectra for the small-box run VIII are shown in Figure 3.7. The visible bump in the energy spectrum at the nonrelativistic inertial scale (left panel) warrants a discussion. As the initial field-perpendicular magnetic perturbations relax, they drive turbulence at large scales. In a magnetically dominated plasma, the excited large-scale fluctuations can be a combination of the two modes whose magnetic polarizations are normal

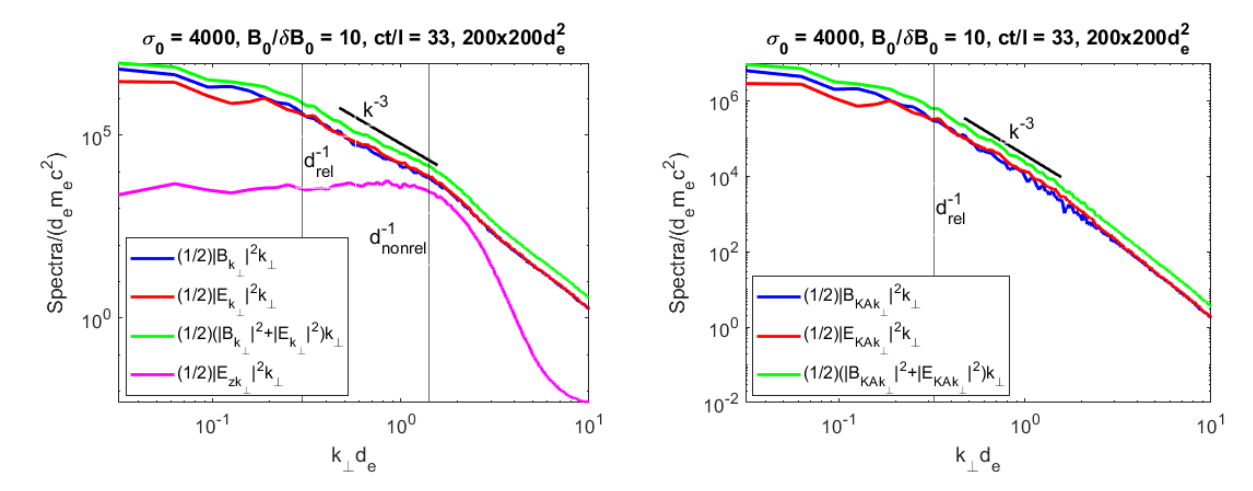


Figure 3.7: The electric and magnetic spectra for the small-box run VIII. The left panel shows the spectra of the perpendicular components of electric and magnetic fields, as well as the spectrum of E_z . The E_z -spectrum is concentrated at the nonrelativistic inertial scale defined in Equation (3.26) and corresponds to the ordinary mode produced by the initial magnetic perturbations. The right panel shows the kinetic-Alfvén spectra where the fluctuations associated with the ordinary mode have been removed. The spectra indicated by the solid lines are given for the reader's orientation.

to the background field: the shear-Alfvén mode and the ordinary mode. The frequency of the ordinary mode is given by

$$\omega^2 = \omega_p^2 + k^2 c^2, (3.25)$$

where $\omega_p^2 = 2\omega_{pe}^2 \langle 1/\gamma^3 \rangle$, see Equations (A.12) and (A.15) in Appendix A. This mode is excited in our setup with a relatively low amplitude, contributing only a small fraction of the total turbulent energy. Such a mode is not important at the hydrodynamic scales.

In the small-box run, the imposed magnetic fluctuations at t=0 are relatively strong at small scales; their decay leads to the production of a weak ordinary mode. Such a mode is most strongly generated at the smallest scale available for Aflvénic fluctuations since the current is largest there. This is the inertial scale of a nonrelativistic pair plasma, expressed as

$$d_{\text{nonrel}} = d_e / \sqrt{2}. \tag{3.26}$$

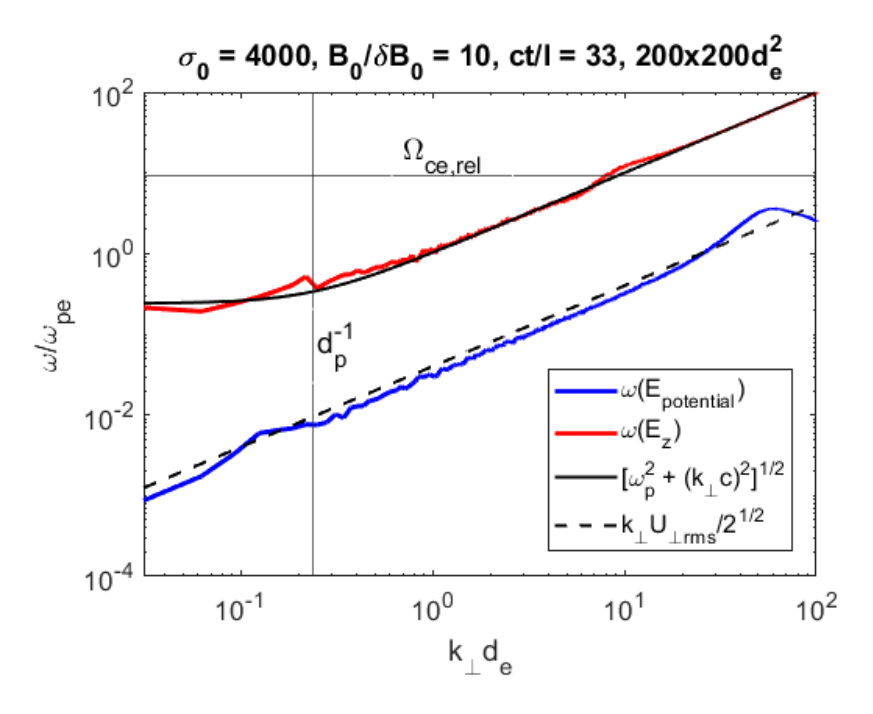


Figure 3.8: Frequencies of the ordinary fluctuations and the potential fluctuations measured in Run VIII according to Equations (A.15) and (3.28). Here, we denote $d_p \equiv c/\omega_p$, where the relativistic plasma frequency ω_p is defined in Equation (3.25), and $\Omega_{\text{ce,rel}} \equiv \Omega_{\text{ce}}/\langle \gamma \rangle$, where Ω_{ce} is the nonrelativistic electron cyclotron frequency and $\langle \gamma \rangle$ is given in Table 3.2.

The left panel of Figure 3.7 shows that the energy of the ordinary modes is indeed concentrated at these kinetic scales that are the focus of our study. Since the phase velocity of the ordinary mode exceeds the speed of light (see Equation (3.25)), such fluctuations are not significantly damped. Therefore, we need to make sure that in our statistical analysis, the fluctuations associated with such a mode are separated from the Alfvénic fluctuations.

The ordinary mode can be detected in simulations if we observe that its electric field is polarized in the z direction, while the electric polarization of the shear-Alfvén mode is normal to the z direction. The frequency of the E_z fluctuations can be numerically found by taking the Fourier transform of the z-component of the Maxwell-Ampere law $\nabla \times \mathbf{B} = (4\pi/c)\mathbf{J} + (1/c)\partial \mathbf{E}/\partial t$, obtaining

$$\omega^2 = \frac{\left| (\boldsymbol{\nabla} \times \boldsymbol{B})_{z,k} - \frac{4\pi}{c} J_{z,k} \right|^2}{\left| \frac{1}{c} E_{z,k} \right|^2}.$$
 (3.27)

Figure 3.8 shows this frequency calculated for the small-box run. The frequency indeed agrees with the analytic dispersion relation given by Equation (3.25). Since $k_{\perp} \gg k_z$, the frequency of the ordinary mode is much larger than the frequency of shear-Alfvén fluctuations. The oblique shear-Alfvén fluctuations are characterized by a mostly potential electric field. The frequency of the potential electric fluctuations can be measured by substituting Gauss's law $\nabla \cdot \mathbf{E} = 4\pi \rho$ into the charge conservation equation $\partial \rho / \partial t + \nabla \cdot \mathbf{J} = 0$ and taking the Fourier transform, obtaining

$$\omega^2 = \frac{\left|\frac{4\pi}{c} \, \boldsymbol{k} \cdot \boldsymbol{J}_k\right|^2}{\left|\frac{1}{c} \, \boldsymbol{k} \cdot \boldsymbol{E}_k\right|^2}.\tag{3.28}$$

This formula can also be obtained by taking the divergence of the Maxwell-Ampère law. Figure 3.8 illustrates that it is indeed much smaller than the frequency of the ordinary mode. We also note that the frequency calculated in Equation (3.28) coincides with the frequency of electric charge fluctuations.

Run	$U_{z,\mathrm{rms}}^e$	$U_{\perp,\mathrm{rms}}^e$	$U_{z,\mathrm{rms}}$	$U_{\perp,\mathrm{rms}}$	$\langle \tilde{\gamma}^e \rangle$	$\langle \gamma \rangle$
VII	0.47c	0.070c	0.32c	0.053c	1.25	11.3
VIII	0.61c	0.079c	0.39c	0.056c	1.73	9.5

Table 3.2: Parameters of the velocity fluctuations for the electron fluid, and for the bulk plasma motion, $\mathbf{U} = (n_i \mathbf{U}^i + n_e \mathbf{U}^e)/(n_i + n_e)$. Here, $\tilde{\gamma}^e$ is the Lorenz factor associated with the electron fluid velocity and γ to the particle velocity. The measurements are made at ct/l = 76 for run VII and ct/l = 33 for run VIII.

The nearly linear scaling of the measured frequency of potential fluctuations with the wavenumber can result from two independent effects. First, it may reflect the almost linear dispersion relation of the Alfvén mode given by Equation (3.18). Indeed, in our 2.5D runs, the magnetic-field direction deviates from the z-axis by a small angle, $\sin \theta \sim \delta B_{\perp}/B \sim 0.05$. By the critical balance condition, Alfvén fluctuations with the wavenumber k_{\perp} then correspond to the field-parallel wavenumber $k_{\parallel} \sim k_{\perp} \sin \theta$. According to Equation (3.18), this gives the frequency of linear Alfvén mode, $\omega \sim k_{\perp}c \sin \theta \sim 0.05 k_{\perp}c$, which is not far away from the measurements in Figure 3.8. Second, it may correspond to the linear "Doppler shift"

of the frequency provided by the passive advection of the small-scale plasma structures by large-scale Alfvén fluctuations, $U_{\perp,\text{rms}}$. Since $U_{\perp,\text{rms}} \sim 0.05 \, c$ in our runs (see Table 3.2), the corresponding angle-averaged frequency shift, $\omega \sim k_{\perp} U_{\perp,\text{rms}}/\sqrt{2}$, is also consistent with the measurements in Figure 3.8.

The magnetic-field spectrum associated with the ordinary mode is found from Faraday's law:

$$|\mathbf{B}_{\perp,k_{\perp}}|^2 = \frac{k_{\perp}^2 c^2}{\omega^2} |E_{z,k_{\perp}}|^2,$$
 (3.29)

where the frequency should be substituted from Equation (3.27). Since the frequency of the ordinary fluctuations is much larger than that of the Alfvén mode, we may average high-frequency ordinary fluctuations independently of the low-frequency Alfvén fluctuations. We may then obtain the electromagnetic spectrum associated with the Alfvén modes by subtracting the spectrum of the ordinary mode (3.29) from the total spectrum of magnetic fluctuations. The right panel of Figure 3.7 shows the spectra of the electric and magnetic fields where the fluctuations associated with the ordinary mode have been removed. The observed spectrum is close to k^{-3} , which is consistent with the scaling expected for the kinetic-Alfvén modes.

3.4 Particle energization in relativistic plasma turbulenece

Stochastic particle energization in magnetic traps

To explain the origin of the power-laws observed in the particle energy pdfs, we follow Vega et al. (2022b) and propose a model where a fraction of particles may be trapped locally by spontaneously generated magnetic structures where the particles get accelerated until they escape the trap due to pitch angle scattering. The pitch angle width of the trapped

population depends on the so-called magnetic compressibility of turbulence, and it defines the power-law exponent of the resulting particle energy distribution function. Below, we present our phenomenological model for particle acceleration and then compare our predictions with runs I through VI, and IX and X.

We will base our discussion on the two key numerical observations related to the stochastic acceleration process. First, the particle energization resembles a diffusion process in the energy space, with the diffusion coefficient scaling with the particle energy as γ^2 at $\gamma \gg 1$. This may indicate that the particles experience a second-order Fermi acceleration (e.g., Fermi, 1949; Teller, 1954; Kulsrud and Ferrari, 1971), where scattering events are provided by moving magnetic mirrors (e.g., turbulent eddies or magnetic structures advected by turbulence (Achterberg, 1984; Selkowitz and Blackman, 2004; Yan et al., 2008; Pongkitiwanichakul and Chandran, 2014; Demidem et al., 2020)). An individual scattering event then randomly changes the particle energy as $\Delta \gamma \propto \pm \gamma$, see, e.g., the discussion in Blandford and Eichler (1987); Zhdankin et al. (2018a). It is also consistent with particle interactions with wave turbulence since, as was elucidated in Demidem et al. (2020), the quasilinear diffusion coefficient of ultrarelativistic particles in strong Alfvénic turbulence is also proportional to γ^2 . Second, numerical simulations indicate the presence of an exponentially strong regular dissipation process at large energies (e.g., Figure 4 in Wong et al., 2020), which is crucial for establishing a power-law distribution of ultrarelativistic particles.

We propose that a power-law particle energy distribution may be understood based on the following phenomenological dynamical model that incorporates both observed diffusion and dissipation. Consider an ultrarelativistic particle with momentum $p \equiv |\mathbf{p}| \approx p_0$, and describe particle interactions with nonrelativistic randomly moving fluid elements by a stochastic dynamical equation (Langevin equation):

$$d\mathbf{p}/dt = p\,\mathbf{\eta}(t),\tag{3.30}$$

with an isotropic Gaussian white random noise

$$\langle \eta^i(t)\eta^j(t')\rangle = 2D\delta^{ij}\delta(t-t'),$$
 (3.31)

$$\langle \eta^i(t) \rangle = 0, \tag{3.32}$$

where D is a constant normalization coefficient. Such an equation satisfies the required diffusion scaling $\langle (\Delta p)^2 \rangle \propto p^2$, while the random vector $\boldsymbol{\eta}$ mimics the velocity of the scatterers. The corresponding Fokker-Planck equation for the probability density function $F(\boldsymbol{p})$, can then be easily derived (e.g., Øksendal, 2003):

$$\frac{\partial F}{\partial t} = D \frac{\partial}{\partial p^i} p \frac{\partial}{\partial p^i} (pF) , \qquad (3.33)$$

where we sum over repeated indices. As there is a local mean magnetic field in a region where particles get accelerated, we may rewrite Equation (3.33) in the spherical coordinates with respect to the direction of the field. Introducing the phase-space-volume compensated function $g(p, \mu) = F(p, \mu)4\pi p^2$, we get

$$\frac{\partial g(p,\mu)}{\partial t} = D \frac{\partial}{\partial p} p^3 \frac{\partial}{\partial p} \left(\frac{g}{p}\right) + D \frac{\partial}{\partial \mu} \left(1 - \mu^2\right) \frac{\partial}{\partial \mu} g. \tag{3.34}$$

Here, $\mu = \cos \theta$ is the cosine of the angle between the particle momentum and the magnetic field.

We now assume that a particle gets accelerated locally when it can be trapped by a turbulent structure. We can estimate the trapping angles using the conservation of the magnetic moment, $M=p_{\perp}^2/B$. If a typical trap has minimum and maximum magnetic fields B_{\min} and B_{\max} , respectively, for marginally trapped particles with energy pc we have $p^2=p_{\parallel}^2+MB_{\min}=MB_{\max}$, so $\mu^2<\mu_0^2=cos^2\theta_0=p_{\parallel}^2/p^2=\Delta B/B_{\max}$. The particles "leak"

⁵Note that this derivation assumes energy conservation, so it should only be valid in the rest frame of the magnetic mirror. Since we are assuming nonrelativistic bulk motion, we will neglect the transformation of the magnetic field and the angle and take the result as valid in the laboratory frame.

from the acceleration region due to pitch angle scattering when their pitch angle cosines exceed μ_0 (note that pitch angle scattering breaks the conservation of the magnetic moment).

To find the steady-state solution of Equation (3.34), we use separation of variables to write $g(p, \mu) = f(p)h(\mu)$, obtaining

$$0 = h \frac{\partial}{\partial p} p^3 \frac{\partial}{\partial p} \left(\frac{f}{p} \right) + f \frac{\partial}{\partial \mu} \left(1 - \mu^2 \right) \frac{\partial}{\partial \mu} h. \tag{3.35}$$

Next, we calculate the lowest eigenvalue of the pitch angle diffusion operator (the second term in the equation above) 6 ,

$$-\frac{\partial}{\partial\mu}\left(1-\mu^2\right)\frac{\partial}{\partial\mu}h = \lambda h. \tag{3.36}$$

In general, it should be supplemented by a boundary condition of the form $(h + a \partial h/\partial \mu)_{|\mu|=\mu_0}$ = 0, ensuring that the distribution function matches at the boundary the distribution function of non-accelerated particles.⁷ As the contrast between the accelerated and non-accelerated particles is expected to increase at larger γ , the parameter a may in principle vary (slowly decline) with γ . For our simplified treatment, we choose $h_{|\mu|=\mu_0}=0$, which we expect to be valid asymptotically at large γ . The eigenvalue can then be found perturbatively in the small parameter μ_0^2 , which gives, up to the first order:

$$\lambda = \frac{\pi^2}{4\mu_0^2} - \frac{1}{2} - \frac{\pi^2}{12}.\tag{3.37}$$

The momentum diffusion equation now takes the form

$$\frac{\partial f}{\partial t} = D \frac{\partial}{\partial p} p^3 \frac{\partial}{\partial p} \left(\frac{f}{p} \right) - D\lambda f. \tag{3.38}$$

⁶More generally, one may propose a linear combination of eigenfunctions with different eigenvalues, but the one with smallest eigenvalue dominates at high energies. We also note that the eigenfunction with the lowest eigenvalue is the only one that is positive definite.

⁷For $a \to 0$ this transforms into the Dirichlet boundary condition, while for $a \to \infty$ into the Neumann boundary condition.

The last term on the right-hand side describes the loss of particles from the acceleration region of the phase space, while the first term describes the particles supply into this region and their acceleration (we remind that Equations (3.33) and (3.38) are valid only for ultrarelativistic energies, $p \approx \gamma mc$ and $\gamma \gg 1$). The steady-state solution of Equation (3.38) can then be found as $f(p)dp \propto p^{-\alpha}dp$, where

$$\alpha = \sqrt{\lambda + 1} = \sqrt{\frac{\pi^2}{4} \frac{B_{\text{max}}}{\Delta B} + \frac{1}{2} - \frac{\pi^2}{12}}.$$
 (3.39)

The particle distribution function is, therefore, non-universal in our model, in that it depends on the ratio $\frac{B_{\text{max}}}{\Delta B}$ for a given magnetic trap.

Numerical results

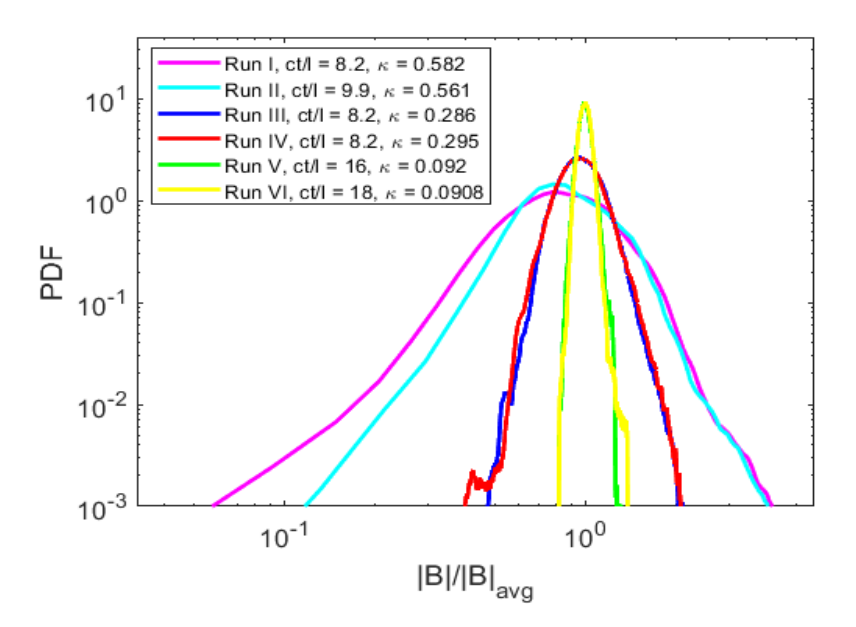


Figure 3.9: The magnetic-field strength distribution functions and the corresponding magnetic compressibilities κ . The distribution is independent of the magnetization parameter but depends on the relative strength of the applied magnetic field.

In the previous subsection, we derived a power-law formula for the particle energy pdf f(p) within a magnetic trap where, in our model, particles are accelerated. We will now

compare our model with our numerical results. Let f_{global} the ultrarelativistic tail of the particle energy pdf for the entire simulation domain and let $f_{\text{trap},j} \propto \gamma^{-\alpha_j}$ be the particle energy pdf of ultrarelativistic particles accelerated by magnetic trap j, where we are using the particle Lorentz factor $\gamma = p/(mc)$ instead of p as it is more convenient to use a dimensionless parameter in the calculation that follows. We may write

$$f_{\text{global}} = \sum_{j} f_{\text{trap},j} = \sum_{j} a_j \gamma^{-\alpha_j},$$
 (3.40)

where the coefficients a_j are normalization constants for each magnetic trap, renormalized by some constant factor to define the global distribution. Let α_{\min} be the smallest α_j (i.e., $\alpha_j - \alpha_{\min} \geq 0$ for every j). Then

$$f_{\text{global}} = \sum_{j} f_{\text{trap},j} = \gamma^{-\alpha_{\min}} \sum_{j} a_{j} \gamma^{-(\alpha_{j} - \alpha_{\min})} \sim \gamma^{-\alpha_{\min}}, \quad \text{for } \gamma \gg 1.$$
 (3.41)

From Equation (3.39) and writing $\frac{B_{\text{max}}}{\Delta B} = 1/(1 - B_{\text{min}}/B_{\text{max}})$ we see that α_{min} corresponds to the trap with the smallest $B_{\text{min}}/B_{\text{max}}$ ratio (or, to be more correct, the traps with the smallest $B_{\text{min}}/B_{\text{max}}$ will tend to dominate in the summation (3.40)). To compute a proxy for the smallest $B_{\text{min}}/B_{\text{max}}$ that is easy to calculate with the simulation data we will define $B_{\text{min}} = \langle B \rangle - (\delta B)_{\text{rms}}$ and $B_{\text{max}} = \langle B \rangle + (\delta B)_{\text{rms}}$, where B is the magnitude of the magnetic field, $(\delta B)_{\text{rms}}$ is the root-mean-square magnetic fluctuation, and the average $\langle ... \rangle$ is over the whole domain. In this way, we imagine a hypothetical magnetic trap with a very strong B_{max} (one standard deviation above the mean) and a very weak B_{min} (one standard deviation below the mean). Now we can estimate α_{global} by defining the global magnetic compressibility $\kappa = \Delta B/B_{\text{max}}$, with $\Delta B = 2(\delta B)_{\text{rms}}$. The magnetic field strength distribution functions and corresponding turbulent magnetic compressibilities for runs I to VI are presented in Figure 3.9. Note that the magnetic compressibilities are very similar in different runs with the same $\delta B_0/B_0$, but they depend on $\delta B_0/B_0$.

Finally, we can estimate the power-law spectral index α of the global particle energy pdf

as

$$\alpha = \sqrt{\frac{\pi^2}{4} \frac{1}{\kappa} + \frac{1}{2} - \frac{\pi^2}{12}}.$$
 (3.42)

Figure 3.10 shows the corresponding particle energy distribution functions for 2.5D runs I to VI and 3D runs IX and X. The energetic tails of the distribution functions exhibit approximate power-law behavior. As seen in Table 3.3, the power-law exponents are in very good agreement with the prediction given by Equation (3.42), especially in the cases of strong magnetization $\tilde{\sigma}_0 \gtrsim 40$ and guide field $B_0 \leq \delta B_0$. These exponents also agree well with the exponents reported by Comisso and Sironi (2018, 2019) for even stronger magnetization, corresponding to $\tilde{\sigma}_0 = 80$ in our notation.⁸ This means that our simulations have reached the universal asymptotic regime of strong magnetization mentioned in Section 1.6. In the regime of weak magnetization, $\tilde{\sigma}_0 = 10$, our model underestimates the power-law exponents in the limit of weak guide field, $(B_0/\delta B_0)^2 \ll 1$. This may indicate that the assumptions of the model, such as the isotropy of the random noise in Equation (3.31), the relation of the global magnetic compressibility κ to the local trapping angles μ_0 , and simplified boundary conditions in Equation (3.36), need to be modified for the low magnetization, weak guide field cases.

We note that in the case of the 3D runs, the measurements were made at an earlier time compared to the 2.5D runs with similar σ_0 and $\tilde{\sigma}_0$ due to the faster decay of the electromagnetic energy with time (see top-left panel of Figure 3.1).

Strong-guide-field runs V and VI $(B_0/\delta B_0 = 3)$ are still evolving at t = 8 l/c; they start approaching quasisteady states only at about t = 16 l/c. Although run VI does seem to display a power-law behavior, we note that, as can be seen in the middle-right panel, its

⁸Note that our definition of fluctuation magnetization $\tilde{\sigma}_0$ is a factor of two different from the corresponding definition in (Comisso and Sironi, 2018, 2019). For instance, our $\tilde{\sigma}_0 = 40$ corresponds to $\sigma_0 = 20$ in Comisso & Sironi simulations.

⁹This case belongs to the asymptotic regime of weak magnetization, as it agrees with the cases of even smaller magnetization studied in Zhdankin et al. (2018a).

high-energy tail may be better described by a log-normal distribution ¹⁰:

$$f(\gamma) d\gamma = \frac{A}{\gamma} \exp\left[-\frac{(\ln \gamma - \mu)^2}{2\sigma_s^2}\right] d\gamma, \tag{3.43}$$

where A is a normalization constant.

Run	Dim.	ct/l	α (pred.)	α (meas.)
I	2.5D	8.2	2.0	2.7
II	2.5D	9.9	2.0	2.1
III	2.5D	8.2	2.9	3.0
IV	2.5D	8.1	2.8	2.7
V	2.5D	25	5.1	_
VI	2.5D	26	5.2	4.8
IX	3D	4	3.0	2.7
X	3D	4	3.0	2.6

Table 3.3: Parameters of the runs and the corresponding predicted and measured exponents of the particle distribution function, $f(\gamma)d\gamma \propto \gamma^{-\alpha}d\gamma$. The middle column states the time when both the magnetic compressibility and observed slope were measured.

Going to even higher guide field, Figure 3.11 shows the particle energy pdf of runs VII and VIII $(B_0/\delta B_0 = 10)$, which takes even longer to stabilize than runs V and VI. Unlike the other simulations with $\tilde{\sigma}_0 = 40$, no power-law tail is observed. However, a log-normal distribution is a very good fit for both cases. Moreover, the particle distribution in momentum space $(p_{\parallel}, p_{\perp})$, shown in Figure 3.12, is seen to be strongly anisotropic with respect to the background magnetic field. The electrons are energized mostly in the field-parallel direction, leading to a nearly one-dimensional particle distribution function. The anisotropy is also reflected in the energy-momentum tensor, with $T_{\perp}/T_{zz} \approx 0.02$ for both run VII and VIII.

The absence of well-defined power-law tails in runs V and VI or their absence altogether in runs VII and VIII, where a log-normal particle energy distributions in seen instead, may indicate that different particle acceleration mechanisms operate in the weak and strong guide

¹⁰We note that both the plasma magnetization and the statistical standard deviation are conventionally denoted by the same letter σ . We therefore denote the standard deviation by σ_s ; it should not be confused with the plasma magnetization parameter.

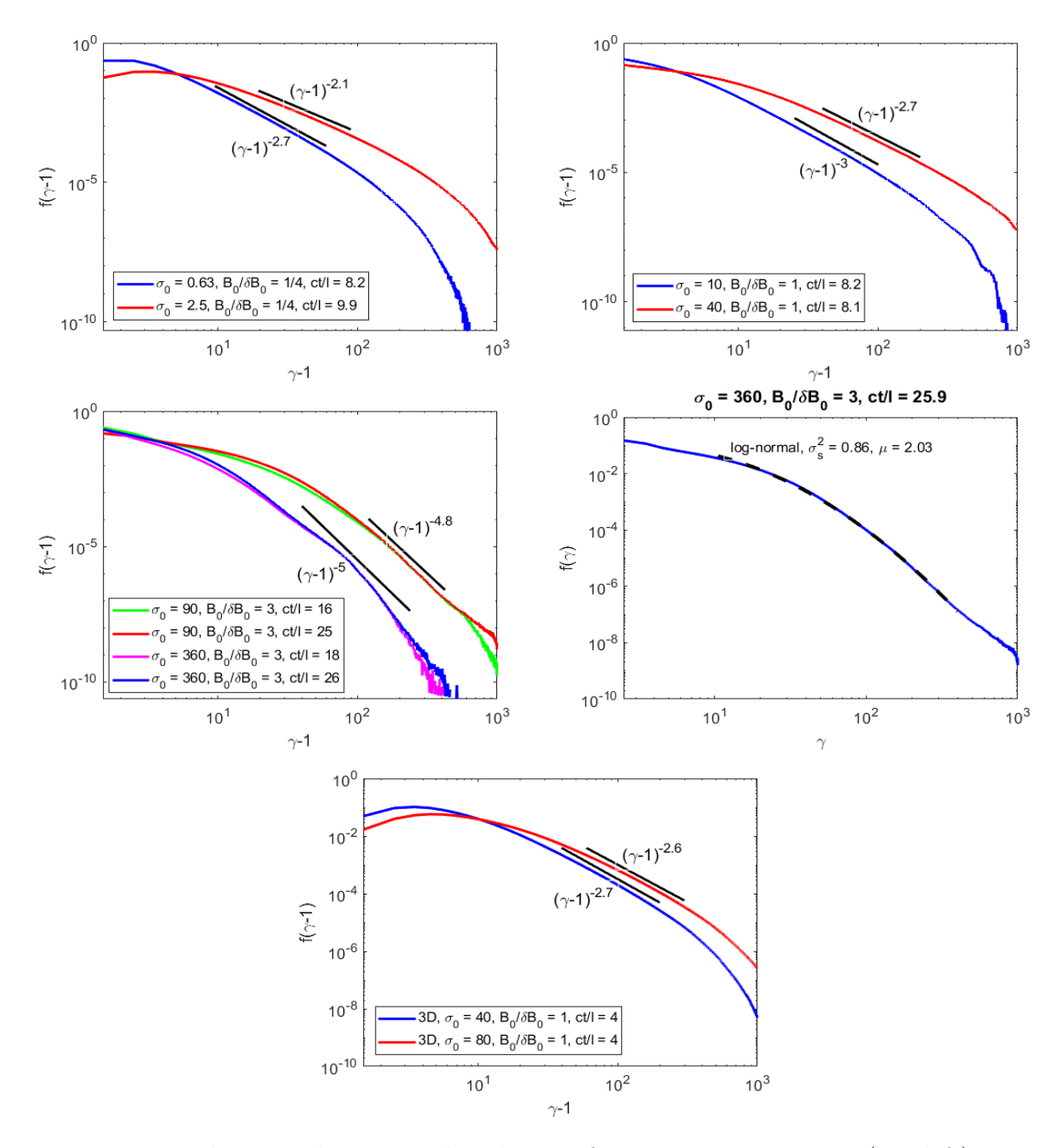


Figure 3.10: The particle energy distribution functions in runs I, II (top-left), III, IV (top-right), V, VI (middle row), IX, and X (bottom). The lines indicating power-law slopes are given for reference. The middle-right panel shows a log-normal fit on run VI, $f(\gamma) \propto \gamma^{-1} \exp[-(\ln \gamma - \mu)^2/(2\sigma_s^2)]$.

field regimes. In the next section, we delve deeper into the possible acceleration mechanisms; our analysis will lead us to a reinterpretation of our model of magnetic traps.

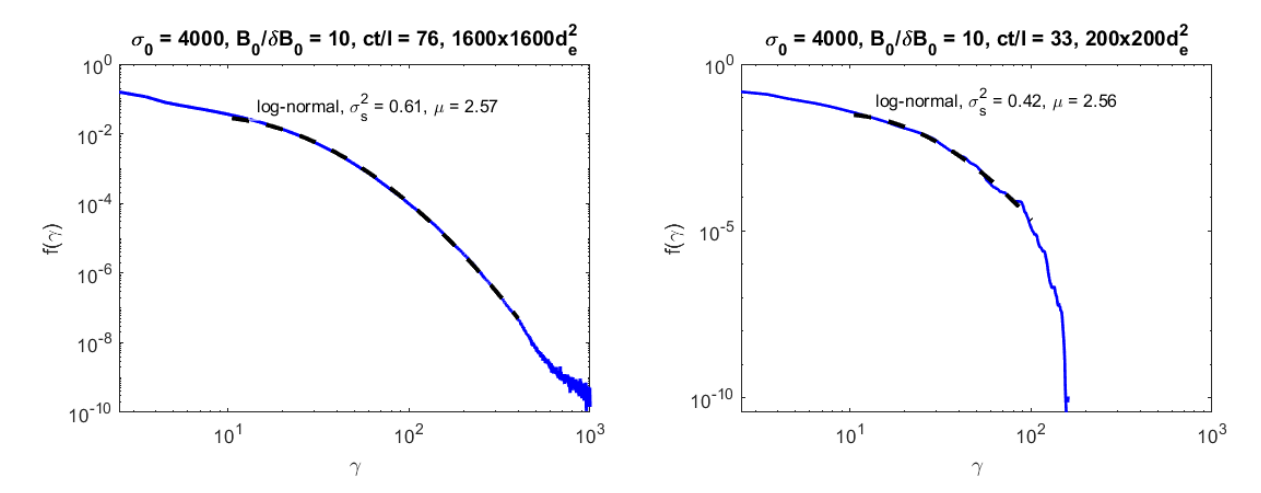


Figure 3.11: Electron energy distribution functions. The black dashed lines show log-normal fits, $f(\gamma) \propto \gamma^{-1} \exp[-(\ln \gamma - \mu)^2/(2\sigma_s^2)]$.

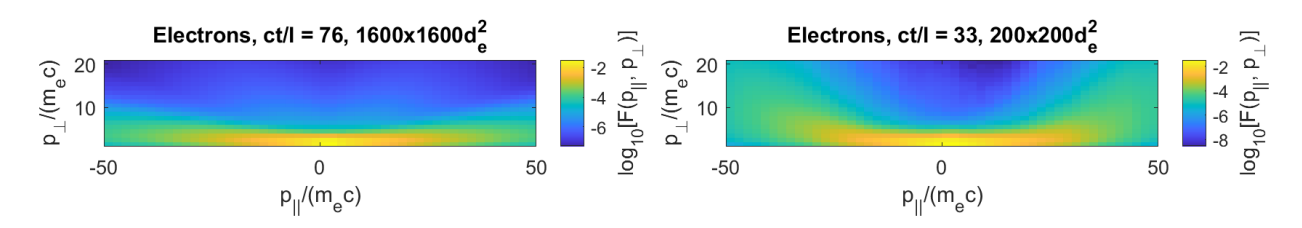


Figure 3.12: The electron distribution functions. Here, p_{\parallel} and p_{\perp} are particle momenta in the directions parallel and perpendicular to the background magnetic field \mathbf{B}_0 . The functions are strongly anisotropic. The anisotropy at very large energies is slightly less pronounced in run VIII, which is likely a consequence of the smaller box size.

3.5 A closer look at acceleration by Alfvénic turbulence

In this section, we will follow Vega et al. (2024a). A relativistic particle whose gyroradius is much smaller than the typical scale of magnetic field variations preserves its first adiabatic invariant, the magnetic moment. Such a particle can be accelerated by turbulent fluctuations in several different ways. These can be divided into three categories. First is the acceleration by a parallel electric field, that is, the electric field component parallel to the magnetic field. Second is the acceleration due to magnetic curvature drifts. And third is the acceleration by magnetic mirror forces. In all the cases, a particle is, of course, accelerated by an electric

field. The proposed division into the three categories helps to associate the acceleration mechanisms with turbulent structures. Below, we analyze these cases concentrating on an ultrarelativistic pair plasma.

Acceleration by parallel electric field

The parallel electric field fluctuations are relatively weak in Alfvénic turbulence with a strong guide field. For instance, in a magnetically dominated ultrarelativistic plasma, the linear wave analysis in Appendix A yields for the parallel and perpendicular electric fluctuations at scales $\lambda \gtrsim d_{\rm rel}$:

$$\frac{E_{\parallel}}{E_{\perp}} \approx \frac{1}{w_0^2} k_{\parallel} k_{\perp} d_{\text{rel}}^2,$$
 (3.44)

see Equation (A.25) in Appendix A. Here, $k_{\perp} \sim 1/\lambda$ is the field-perpendicular wave number of the electric field, k_{\parallel} the field-parallel wavenumber, w_0 is the enthalpy per particle associated with the (relativistic) distribution function of the bulk electrons, and $d_{\rm rel}$ is the corresponding relativistic inertial scale. In the ultrarelativistic case, $w_0 \gg 1$, the parallel electric field remains relatively weak even for the strongest current sheets of thickness $\lambda \sim d_{\rm rel}$ and field variations $E_{\perp} \sim \delta B_{\perp}$. As a relativistic electron propagates through such a structure, its energy gain is

$$m_e c^2 \Delta \gamma = q E_{\parallel} \ell \sim q \, d_{\rm rel} \, \delta B_{\perp} / w_0^2, \tag{3.45}$$

which is equivalent to

$$\Delta \gamma \sim \sqrt{\tilde{\sigma}}/w_0. \tag{3.46}$$

When $\tilde{\sigma}$ is initially large, as is the case in the numerical setups of decaying turbulence analyzed in Chapter 3 of this thesis and elsewhere (e.g., Comisso and Sironi, 2018, 2019),

the parallel particle heating and acceleration are initially strong. However, as the magnetic perturbations relax and release energy to plasma particles, plasma magnetization $\tilde{\sigma}$ decreases while (in the absence of significant radiative cooling) the particle enthalpy w_0 increases. As a result, parallel electric heating by Alfvén modes becomes progressively less significant. Moreover, the parallel electric acceleration is linear (or algebraic) in time, as opposed to the exponential acceleration due to curvature and mirror effects discussed below. Finally, we note that parallel heating and acceleration increase the field-parallel momentum of a particle, but not its field-perpendicular momentum. Therefore, the particle's pitch angle decreases as a result of such a process.

Curvature acceleration

When the parallel electric field effects are negligible and the particle magnetic moment is conserved, the dominant acceleration is provided by the curvature and polarization drifts. Indeed, these drifts do not vanish in the limit of small pitch angles and, therefore, they remain efficient when the particle's parallel momentum increases. In a turbulent state, curvature fluctuations are related to fluctuations of the electromagnetic field strength. One can show that in Alfvénic turbulence, curvature and polarization drifts provide similar contributions to particle energization. In our phenomenological treatment, we, therefore, broadly place both mechanisms in the same category, and as an illustration, consider curvature acceleration in detail.

To discuss the curvature acceleration, assume that a uniform component of the magnetic field is in the z-direction. The Alfvénic magnetic perturbation $\delta \mathbf{B}_{\perp}$ is then in the x-y plane. A sketch of the projection of a curved magnetic-field line onto the x-y plane is given in Figure 3.13. We assume that such a magnetic structure is moving with the velocity $\boldsymbol{\beta} = \boldsymbol{v}_E/c$, as shown in the figure. Here, the $\boldsymbol{E} \times \boldsymbol{B}$ velocity, $\boldsymbol{v}_E = c\boldsymbol{E} \times \boldsymbol{B}/B^2$, describes the bulk velocity fluctuations of the plasma. As we discussed before, such fluid fluctuations are typically only mildly relativistic (also seen in other studies; see, for example, Zhdankin

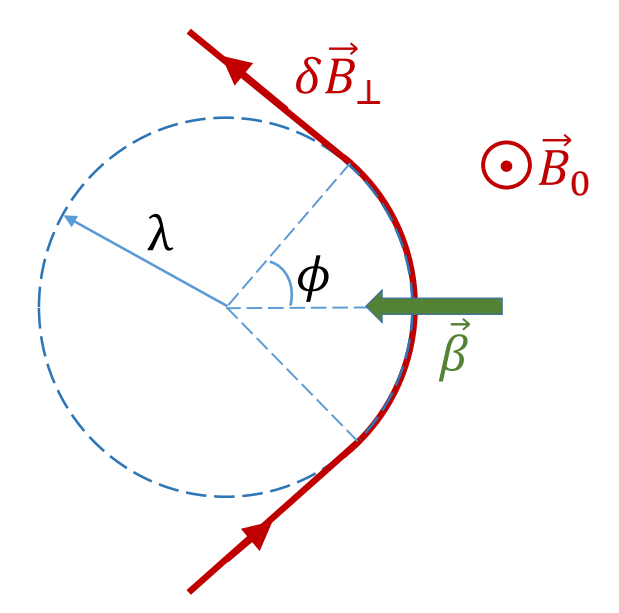


Figure 3.13: Sketch of a curved magnetic field line. The projection of the line on the plane normal to the background magnetic field B_0 is shown. For simplicity, it is assumed that the magnetic structure moves with velocity β in the direction parallel to the field-line curvature. An electron propagating along the curved line, experiences curvature acceleration.

et al., 2018a), so for simplicity, we can neglect relativistic factors associated with the fluid motion. A relativistic electron propagating along the magnetic field line experiences curvature acceleration. When the pitch angle is small, the electron moves along the line at nearly the speed of light. As the electron passes the curved part of the line, its energy changes according to (e.g., Northrop, 1963):

$$\Delta \ln(\gamma) \sim \beta \frac{S}{R_c},$$
 (3.47)

where R_c is the curvature radius of the total magnetic field line (which is not its projection in Figure 3.13) and S is the corresponding length of the curved path. Here, $\beta = \beta \cdot \mathbf{R}_c/R_c$ is the projection of the velocity β onto the direction of the curvature vector, that is, the vector connecting the point on the trajectory with the curvature center. For the collision shown in Figure 3.13, the particle gains energy, $\beta > 0$. Such collisions are more probable, so the particle gains energy on average.

A standard geometric calculation gives for the curvature radius

$$R_c = \lambda \left[1 + \left(\frac{B_0}{\delta B_\perp} \right)^2 \right], \tag{3.48}$$

and for the path length

$$S = 2\phi\lambda \left[1 + \left(\frac{B_0}{\delta B_\perp} \right)^2 \right]^{1/2},\tag{3.49}$$

where fore an estimate, one can assume $2\phi \lesssim \pi$. Substituting these expressions into Equation (3.47), we obtain

$$\Delta \ln(\gamma) \sim 2\phi\beta \left[1 + \left(\frac{B_0}{\delta B_\perp} \right)^2 \right]^{-1/2}.$$
 (3.50)

We note that this result does not depend on the magnitude of the curvature given by the structure's scale, λ . Indeed, a smaller curvature radius would provide a stronger acceleration, however, the propagation path would be shorter, resulting in the same energy gain.

The calculation can be advanced further if the magnetic fluctuations are relatively weak, $\delta B_{\perp}/B_0 \ll 1$. In this case, we approximate:

$$\Delta \ln(\gamma) \sim 2\phi \beta \frac{\delta B_{\perp}}{B_0}.$$
 (3.51)

As we saw in Section 3.3, in strong magnetically dominated Alfvénic turbulence the electric and magnetic fluctuations are nearly in equipartition, $E_{\perp} \sim \delta B_{\perp}$. Therefore, at small field-parallel scales, $\ell \ll \ell_0$, the plasma velocity fluctuations can be evaluated as

$$\beta(\ell) \sim \frac{\delta B_{\perp}(\ell)}{B_0} \sim \frac{\delta B_{\perp,0}}{B_0} \left(\frac{\ell}{\ell_0}\right)^{1/2},\tag{3.52}$$

where $\delta B_{\perp,0}$ represents the magnetic fluctuations on the outer scale of turbulence, ℓ_0 , and we used the field-parallel scaling of magnetic fluctuations characteristic of Alfvénic turbulence, $\delta B_{\perp} \sim \delta B_{\perp,0} (\ell/\ell_0)^{1/2}$; see our discussion on RMHD turbulence in Section 1.3. We then estimate the contribution of a structure of scale ℓ to the energy gain as

$$\Delta \ln(\gamma) \sim 2\phi \left(\frac{\delta B_{\perp}(\ell)}{B_0}\right)^2 \sim 2\phi \left(\frac{\delta B_{\perp,0}}{B_0}\right)^2 \frac{\ell}{\ell_0}.$$
 (3.53)

We see that the acceleration rate is sensitive to the relative strength of the turbulent fluctuations; it rapidly decreases as $\delta B_{\perp,0}/B_0$ decreases. We also notice that larger-scale fluctuations provide stronger acceleration, suggesting that the process may be dominated by the particle interactions with the largest, outer-scale turbulent eddies. However, interactions with small-scale fluctuations may be more frequent. Indeed, in one parallel crossing time, the particle would experience $N_{\ell} \sim \ell_0/\ell$ interactions with structures of scale ℓ . Therefore, structures of all scales may provide comparable contributions to the particle acceleration.

We may assume that the motion of small-scale structures is not correlated with the motion of the large ones, so their contributions to particle acceleration can be counted independently. A more detailed estimate (see Equation (B.6) in Appendix B) then suggests that the particle energy gain in one parallel crossing time would include a logarithmic correction,

$$\Delta_0 \ln(\gamma) \sim 2\phi A_{\parallel} \ln\left(\frac{\ell_0}{\ell_*}\right) \left(\frac{\delta B_{\perp,0}}{B_0}\right)^2,$$
(3.54)

where ℓ_* is the parallel scale of the smallest eddy contributing to the curvature drift. Here, A_{\parallel} is a numerical coefficient of order unity. In Alfvénic turbulence, the field-parallel and field-perpendicular scales of nonlinear fluctuations are related by the critical balance condition, $\ell/\ell_0 \sim (\lambda/\lambda_0)^{\kappa}$, where, for simplicity, one can assume the Goldreich and Sridhar (1995) scaling, $\kappa \approx 2/3$. The precise value of κ is not crucial for our discussion. We can then

alternatively express Equation (3.54) through the field-perpendicular scale:

$$\Delta_0 \ln(\gamma) \sim 2\phi A_\perp \ln\left(\frac{\lambda_0}{\lambda_*}\right) \left(\frac{\delta B_{\perp,0}}{B_0}\right)^2,$$
(3.55)

with $A_{\perp} = \kappa A_{\parallel}$. Obviously, eddies that are smaller than the particle gyroradius, cannot contribute to the particle drift. Therefore, λ_* should be the larger of the two parameters: the inner scale of the turbulence and the particle gyroradius,

$$\lambda_* = \max(d_{\text{rel}}, \rho_\perp). \tag{3.56}$$

One can demonstrate that the choice of λ_* depends on the energy of the particle. As shown in Appendix C, one can introduce an important parameter, the critical energy, that characterizes the process of particle acceleration in Alfvénic turbulence. The critical energy depends on the parameters of turbulence and of the plasma as follows:

$$\gamma_c = \frac{B_0}{\delta B_{\perp,0}} \frac{d_{\rm rel}}{\rho_0} \left(\frac{\lambda_0}{d_{\rm rel}}\right)^{1/3},\tag{3.57}$$

where $\rho_0 = c/\Omega_{ce} = m_e c^2/(qB_0)$. For the energies below the critical value, $\gamma < \gamma_c$, the particle's gyroradius is smaller than the plasma inertial scale, and one should use $\lambda_* = d_{\rm rel}$. However, for energies exceeding the critical value, $\gamma > \gamma_c$, the gyroradius becomes larger than the inertial scale, $d_{\rm rel}$. In this case, one needs to use $\lambda_* = \rho_{\perp}$, where the gyroradius is given by

$$\rho_{\perp} = \rho_0 \left(\frac{\delta B_{\perp,0}}{B_0}\right)^{3/2} \left(\frac{\rho_0}{\lambda_0}\right)^{1/2} \gamma^{3/2}.$$
 (3.58)

In the latter case, the logarithmic factor in Equation (3.55) can be rewritten as

$$\ln\left(\frac{\lambda_0}{\lambda_*}\right) = \frac{3}{2}\ln\left(\frac{\gamma_0}{\gamma}\right),\tag{3.59}$$

where γ_0 is the Lorenz factor corresponding to the largest, outer-scale eddies, $\rho_{\perp} = \lambda_0$. Due to the dependence of the logarithmic factor on γ , the particle acceleration deviates from the exponential law and vanishes when the particle's gyroradius approaches the outer scale of turbulence, $\gamma \sim \gamma_0$; see a more detailed calculation in Appendix C.

Formulae (3.53) and (3.54) or (3.55) are our main result for the curvature acceleration in magnetically dominated Alfvénic turbulence. They have several important consequences. First, in contrast with the linear acceleration provided by a parallel electric field, the curvature acceleration is exponentially fast. Given long enough acceleration time (say, running time of numerical simulations), it would dominate over the energization provided by the parallel electric field. If we allow β to attain both positive and negative values with certain probabilities, Equation (3.50) would lead to a logarithmic random walk. It would result in log-normal energy distributions of accelerated particles.

Second, in the limit of a strong guide field, $\delta B_0 \ll B_0$, the electron magnetic moment is conserved even when the electron interacts with intense intermittent structures. Therefore, as the electron accelerates, its field-perpendicular momentum does not significantly change, while the field-parallel momentum increases. We, therefore, propose that in magnetically dominated strong-guide-field Alfvénic turbulence, the acceleration is provided by curvature drifts, particles are accelerated along the magnetic field lines, and they attain log-normal energy distributions. Due to the quadratic dependence of the acceleration rate on the intensity of turbulent fluctuations, the acceleration time increases significantly when $\delta B_0/B_0$ decreases. These results are consistent with the observations of the time evolution of the electromagnetic energy in Section 3.2 and particle energy distributions in Section 3.4.

Mirror acceleration

Curvature acceleration does not significantly depend on the pitch angle in that it remains efficient even when the pitch angle is small. In contrast, the mirror acceleration depends crucially on the value of the pitch angle. Figure 3.14 shows a head-on interaction of an

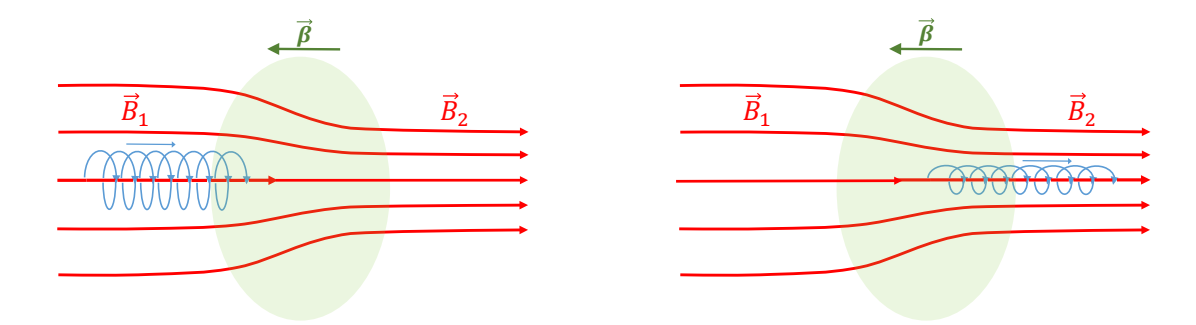


Figure 3.14: Sketch of an electron-mirror interaction for *small* pitch angles. For simplicity, velocity β is directed along the magnetic mirror axis.

electron with a magnetic mirror when the electron pitch angle is small, $\sin^2 \theta < 1 - (\Delta B/B_2)$. Here, $\Delta B = B_2 - B_1 > 0$ is the variation of the magnetic field strength, as shown in the figure. In this case, the electron is not reflected by the mirror but rather propagates through the mirror throat. For simplicity, assume that the electron is ultrarelativistic and the mirror is moving at a relatively lower speed. When the electron passes through the mirror, its energy increases approximately as

$$\Delta \ln(\gamma) \sim \frac{1}{2} \beta \left(\frac{\Delta B/B_2}{1 - \Delta B/B_2} \right) \sin^2 \theta,$$
 (3.60)

where we assumed $\sin^2 \theta \ll 1$. We see that for small pitch angles, the mirror acceleration given by Equation (3.60) is much less efficient than the acceleration by curvature. Due to the conservation of magnetic moment in Alfvénic turbulence with a strong guide field, $\delta B_0 \ll B_0$, particle acceleration decreases the pitch angle even further, $\sin^2 \theta \sim 1/\gamma^2$. Therefore, the mirror acceleration becomes even less relevant.

The situation changes drastically in the case of a moderate guide field, $B_0 \sim \delta B_0$. In this case, collisions with intermittent structures with thickness $d_{\rm rel}$ and magnetic-field variations δB_0 provide significant pitch angle scattering to particles whose gyroradius exceeds $d_{\rm rel}$. As discussed in the previous section and in Appendix C, these are the particles with energies exceeding the critical energy, $\gamma \geq \gamma_c$. Therefore, energetic particles can have large pitch

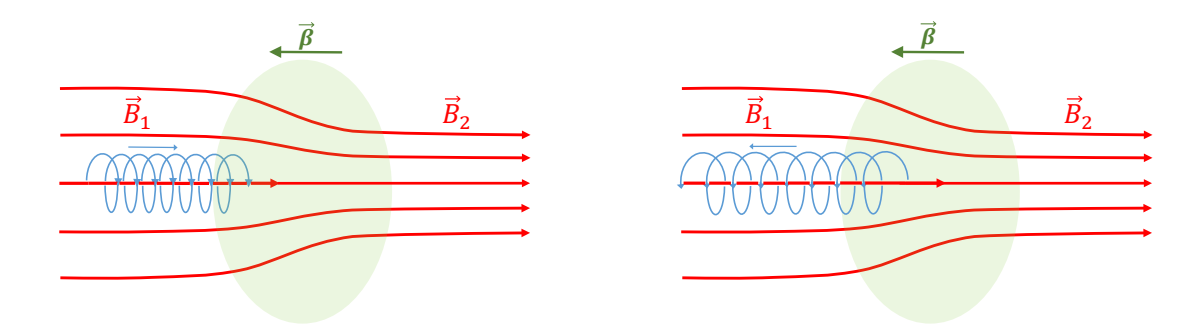


Figure 3.15: Sketch of an electron-mirror interaction for *large* pitch angles. For simplicity, velocity β is directed along the magnetic mirror axis.

angles, $\sin^2 \theta > 1 - \Delta B/B_2$, in which case they may be efficiently accelerated by mirrors. Such a situation is shown in Figure 3.15. In such an interaction, a particle gets reflected from the mirror, and its energy increases according to

$$\Delta \ln(\gamma) \sim 2\beta \cos \theta. \tag{3.61}$$

This energy gain is larger than that associated with a small pitch angle, Equation (3.60). It is also larger or comparable to the curvature acceleration at a similar guide-field strength. Therefore, in the case of a moderate guide field, the population of particles with large pitch angles satisfying $\sin^2 \theta > 1 - (\Delta B/B_2)$, is accelerated by both curvature and mirror effects. As a result, such particles gain energy at a higher exponential rate than the population with small pitch angles, $\sin^2 \theta < 1 - (\Delta B/B_2)$.

This consideration offers us a new way to interpret the model of particle acceleration discussed in Section 3.4: particles are accelerated fast when they are trapped in the phase-space region defined by the pitch angle condition, $\sin^2 \theta > 1 - (\Delta B/B_2)$. Due to pitch angle scattering, particles leak from this region when their pitch angles become smaller. At smaller pitch angles, the acceleration is exponentially weaker and it is neglected. Such a "phase-space leaky box" leads to power-law energy distributions of accelerated particles. The power-law exponent depends on the rate of particle leakage, which in turn, is a function of the turbulence

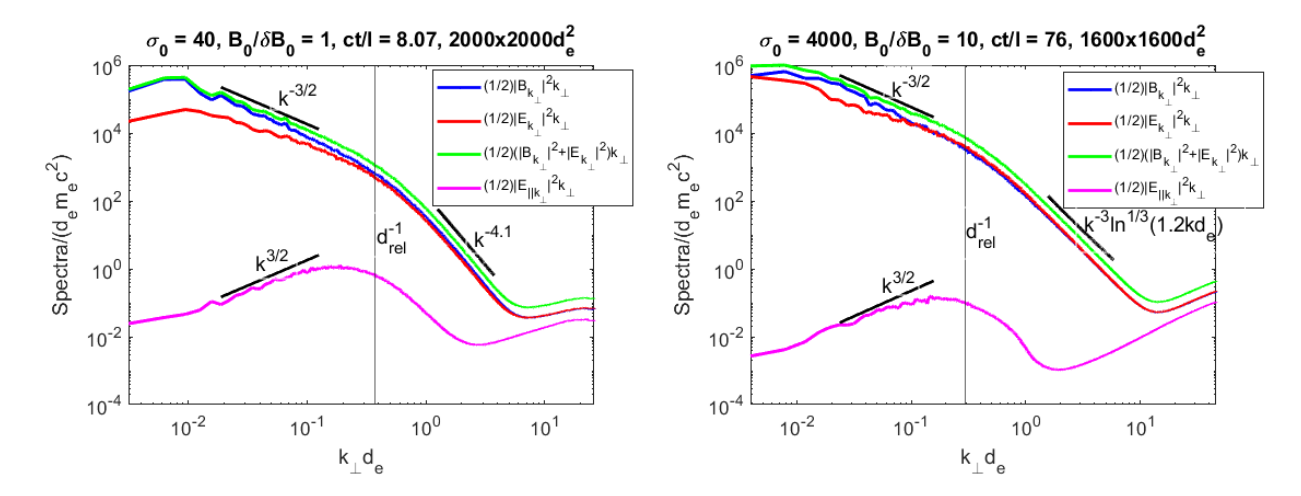


Figure 3.16: Electric and magnetic energy spectra for simulations with $B_0/\delta B_0 = 1$ (left panel) and $B_0/\delta B_0 = 10$ (right panel). Note rather weak parallel electric field fluctuations. The slopes indicated by the solid black lines are given for the reader's orientation.

intensity, $\Delta B/B_2$.

It is also worth noting that in Alfvénic turbulence, mirror structures are generally spatially separated from the regions of large curvature, and, therefore, may be considered as complementary effects. Indeed, phenomenological arguments and numerical simulations suggest that magnetic strength and magnetic curvature are anti-correlated in Alfvénic turbulence (e.g., Schekochihin et al., 2004; Kempski et al., 2023). Moreover, magnetic mirrors are also separated from the intermittent structures that provide pitch angle scattering. Indeed, strong magnetic shears in Afvénic turbulence are typically associated with rotations of magnetic field direction rather than with variations of magnetic field strength (e.g., Zhdankin et al., 2012a,b).

Interpretation of numerical results

It is quite illustrative to compare run IV, with $B_0/\delta B_0 = 1$, and run VII, with $B_0/\delta B_0 = 10$. Both runs are very similar in the way the Alfvénic turbulence is initialized. The only significant difference is the strength of the applied guide field, \mathbf{B}_0 . In both cases, the most efficient phase of particle heating continued until the growing energy of particles approaches

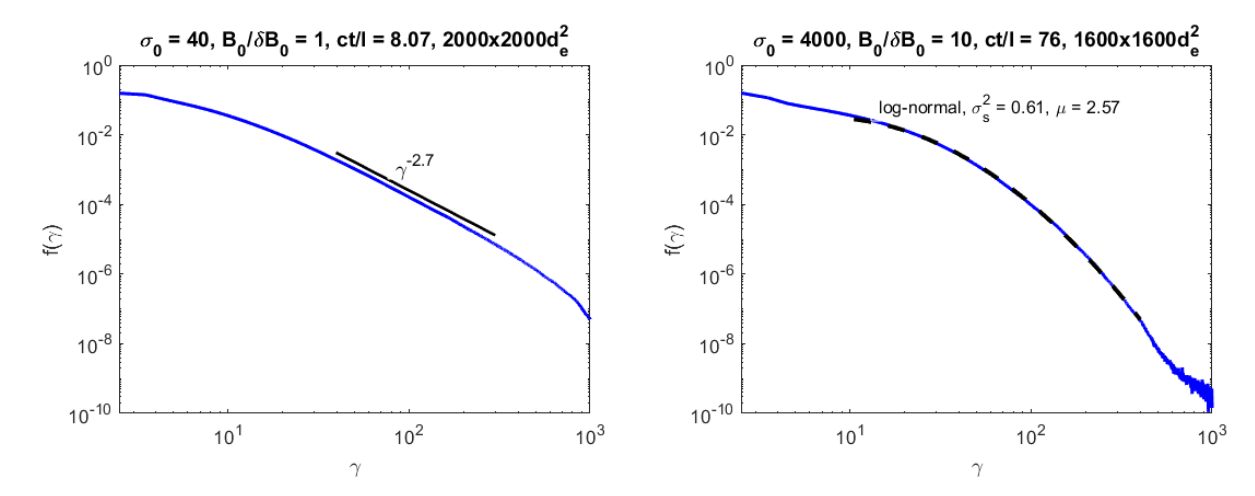


Figure 3.17: Particle energy probability density function for simulations with $B_0/\delta B_0 = 1$ (left panel) and $B_0/\delta B_0 = 10$ (right panel). In the case of a moderate guide field, the energy distribution function has a power-law tail. In the case of a strong guide field, the high-energy tail is well approximated by a log-normal function $f(\gamma) \propto \gamma^{-1} \exp[-(\ln \gamma - \mu)^2/2\sigma_s^2]$, with $\mu \approx 2.6$ and $\sigma_s^2 \approx 0.61$. This function is shown by the dashed line. Note the significantly longer time required to accelerate the particles in the case of a strong guide field.

an approximate equipartition with the decaying energy of electromagnetic fluctuations. This happened when about half of the initial magnetic energy was transferred to particles, so their energies reached $\langle \gamma \rangle \sim 10$ for each species. The electromagnetic spectra of turbulence and the energy distribution functions of the electrons are shown at these moments in Figures 3.16 and 3.17. Figure 3.16 shows that the spectra of electromagnetic fluctuations in the Alfvénic interval, $k_{\perp}d_{\rm rel} \lesssim 1$, are similar in both runs.

Note, however, that it took a significantly longer time to energize the particles in the case of a strong guide field than in the case of a moderate guide field, in qualitative agreement with our discussion. Moreover, the resulting nonthermal tails ($\gamma > 10$) of the energy distribution functions are drastically different in the two cases. In the case of a strong guide field, the distribution is well approximated by a log-normal function. In the case of a moderate guide field, the distribution is close to a power law. This also qualitatively agrees with our modeling.

Figure 3.18 shows the distributions of pitch angles of accelerated particles. In the case of a strong guide field, the pitch angles are extremely small. This is consistent with our formula for the critical energy, Equation (3.57), that gives for this case $\gamma_c \approx 8000$. This

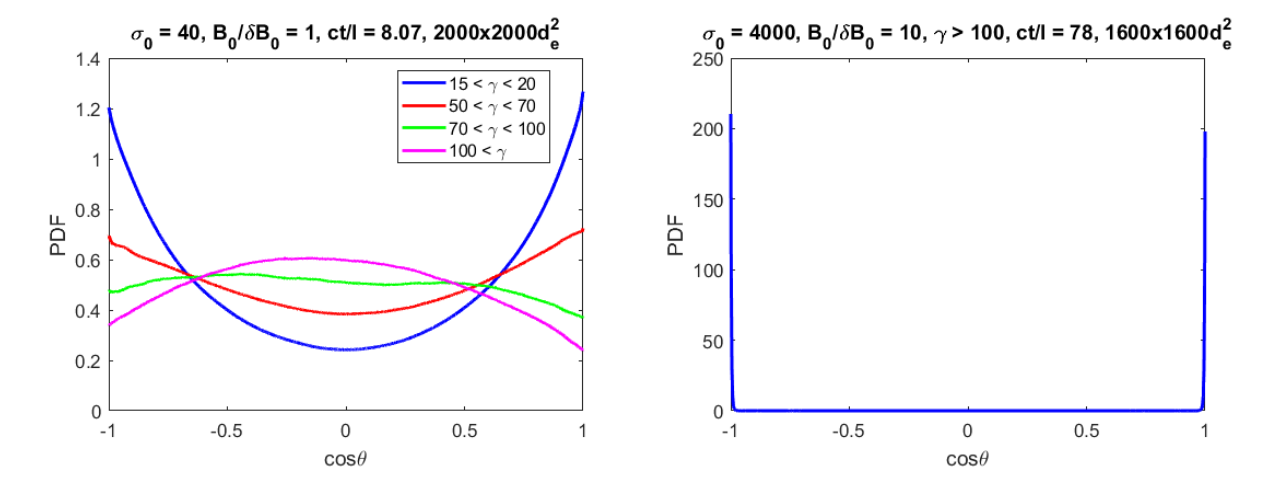


Figure 3.18: pitch angle distribution of ultrarelativistic particles ($\gamma > 100$) for simulations with a moderate guide field, $B_0/\delta B_0 = 1$ (left panel) and a strong guide field, $B_0/\delta B_0 = 10$ (right panel). In the case of a strong guide field, the pitch angles are extremely small. In the case of a moderate guide field, the pitch angles of accelerated particles crucially depend on the particle's energy. For energies smaller than the critical energy, $\gamma \ll \gamma_c$ (in this run, $\gamma_c \approx 70$), the particles are accelerated mostly along the background magnetic field. Above the critical energy, $\gamma \gtrsim \gamma_c$, particles with larger pitch angles are accelerated more efficiently.

means that even the most energetic particles generated in our run, with the energies $\gamma \sim 1000$, will have gyroradii much smaller than $d_{\rm rel}$. The smallest Alfvénic eddy contributing to the acceleration is, therefore, $\lambda_* = d_{\rm rel}$. The process of curvature acceleration is then described by Equation (3.55), leading to a log-normal particle energy distribution.

The situation is fundamentally different in the case of a moderate guide field. Here, the critical energy estimate provided by Equation (3.57), gives $\gamma_c \approx 70$. Figure 3.18, left panel, indeed shows that particles with the smaller energies, $\gamma \ll 70$, are accelerated mostly along the magnetic field lines. However, particles with higher energies $\gamma \gtrsim 70$ are more efficiently accelerated when they have large pitch angles. This is consistent with our picture of particle acceleration suggesting that in the case of a moderate guide field, $B_0 \sim \delta B_0$, particles with $\gamma \gtrsim \gamma_c$ experience strong pitch angle scattering and efficient acceleration by magnetic mirrors.

3.6 Spatial intermittency of fast particles

We have discussed how relativistic turbulence may energize particles and how the different acceleration mechanisms affect the ultrarelativistic tail of the particle energy pdf. One may also wonder how fast particles are distributed in space. In this section, we follow Vega et al. (2023a) and demonstrate that particle heating and acceleration in relativistic turbulence are associated with strong spatial intermittency of the resulting particle distribution function. We argue that the acceleration process creates two populations of particles with different intermittency characteristics. The bulk of the particles, corresponding to the thermal energies $\gamma \lesssim \gamma_{\rm th}$, develops the log-normal distribution of the particle density. The population of the accelerated nonthermal particles ($\gamma \gg \gamma_{\rm th}$), on the other hand, has a strongly inhomogeneous "clumpy" spatial distribution, corresponding to a power-law density distribution function. Strong spatial intermittency of accelerated relativistic particles may be relevant for the radiation flares in such astrophysical objects as pulsar wind nebulae, magnetospheres of black-hole accretion disks, magnetospheres of neutron stars, and blazar jets (e.g., Abdo et al., 2011; Tavani et al., 2011; Wong et al., 2020; Nättilä and Beloborodov, 2021; Grošelj et al., 2024).

In what follows, we first present general physical arguments suggesting that the distribution of plasma particles energized by relativistic turbulence should be spatially intermittent. We then compare the results with simulations II and IV (2.5D), and IX and X (3D).

Phenomenological model

Consider a setting where decaying turbulence is initialized with $1 \ll \sigma_0 \lesssim \tilde{\sigma}_0$. As the magnetic perturbations relax, their energy is converted into relativistic large-scale hydrodynamic plasma flows, whose Lorentz factors $\tilde{\gamma}$ may locally significantly exceed unity. Such ultrarelativistic plasma flows are however highly compressible and, as was pointed out in Section 3.2, their velocities rapidly (on a few large-scale crossing times) become only mildly relativistic. Indeed,

the speed of sound in a relativistic plasma does not exceed $c/\sqrt{3}$ (assuming isotropic pressure and adiabatic large-scale motion), so initial ultrarelativistic and, therefore, supersonic flows rapidly relax to subsonic velocities $\lesssim c/\sqrt{3}$, while simultaneously, the plasma is heated to ultrarelativistic temperatures. This phenomenological picture is consistent with our numerical results, as well as other numerical studies (e.g., Zhdankin et al., 2018a), and with the numerical results presented below.

The resulting relativistic turbulence is therefore inherently compressible. Compressible turbulence is associated with spatially intermittent density fluctuations. In a hydrodynamic picture, the probability distribution function of density fluctuations acquires the log-normal statistics. This may be illustrated in a simple hydrodynamic model of Gaussian random advection. Assume, somewhat idealistically, that the velocity field is nonrelativistic, random, Gaussian, and independent of the density fluctuations. For simplicity, we also assume that this field is short-time correlated, and has a zero mean, $\langle \boldsymbol{U}(\boldsymbol{x},t)\rangle = 0$. Its statistics are therefore fully described by the covariance

$$\langle U^{i}(\boldsymbol{x},t)U^{j}(\boldsymbol{x}',t')\rangle = 2\kappa^{ij}(\boldsymbol{x}-\boldsymbol{x}')\delta(t-t'), \tag{3.62}$$

where the tensor $\kappa^{ij}(\boldsymbol{x}-\boldsymbol{x}')$ describes spatial correlation of the velocity fluctuations, and $\delta(t-t')$ is the Dirac delta function. Starting from the continuity equation for the density field,

$$\frac{\partial n}{\partial t} + \boldsymbol{\nabla} \cdot (n\boldsymbol{U}) = 0, \tag{3.63}$$

which can be viewed as a stochastic Langevin equation with the random noise U(x,t), one can derive the corresponding Fokker-Planck equation for the probability density function of the density field,

$$\frac{\partial P(n,t)}{\partial t} = D \frac{\partial}{\partial n} n \frac{\partial}{\partial n} (nP). \tag{3.64}$$

Here, we introduced the diffusion coefficient defined as

$$D = \nabla_i \nabla_j' \kappa^{ij} (\boldsymbol{x} - \boldsymbol{x}')|_{\boldsymbol{x} = \boldsymbol{x}'}, \tag{3.65}$$

and we sum over repeated indexes. The derivation of the Fokker-Planck equation is standard and can be found in e.g., (Zinn-Justin, 2021, Ch. 34), and the Stratonovich convention is used. As can be directly verified, the solution to the diffusion equation (3.64) is the log-normal distribution. Numerical simulations of nonrelativistic compressible turbulence indeed produce log-normal density distributions (e.g., Kritsuk et al., 2017). Below we will demonstrate that such distributions are also observed in our numerical simulations of relativistic turbulence.

However, as we saw in previous sections, a small population of plasma particles gets accelerated by turbulent electric fields in a run-away fashion, developing power-law tails in the particle energy pdf¹¹. We argue that this population of accelerated, ultrarelativistic particles does not, in general, move with the bulk velocity of the plasma but rather tends to cluster in space. We observe that the statistics of such particles are strongly intermittent, i.e., described by power-law probability density functions, not only in the momentum but also in configuration space.

As discussed in Comisso and Sironi (2019); Wong et al. (2020) and reviewed in Section 1.6, particle acceleration involves two stages. In the first stage, particles are accelerated by reconnection events, which are intermittent in space. In the second stage, particles are accelerated by interaction with random turbulent fluctuations. One can argue that acceleration by turbulence may also lead to spatially intermittent particle distributions.

Given our discussion of acceleration in the previous section and our assumption that $B_0 \lesssim \delta B_0$, it seems appropriate to illustrate how fast particles may cluster in space by considering acceleration by magnetic mirrors. For simplicity, we will consider a quasi-one-dimensional model where particles are scattered by a strong magnetic mirror as shown in

¹¹We remind the reader we are assuming $B_0 \lesssim B_0$. If $B_0 \gg \delta B_0$, the ultrarelativistic tail of the particle energy distribution is a log-normal instead, as seen in Sections 3.4 and 3.5.

Figure 3.19. Such a mirror may correspond to large-scale magnetic fluctuations in turbulence.

Assume that the mirror is moving in the normal direction with the beta factor $\boldsymbol{\beta} = \boldsymbol{U}/c$, the particles propagate along the axis of the mirror at the pitch angle θ , and their beta factor is $\boldsymbol{\beta}_p = \boldsymbol{v}/c$. Assume that the particles have similar Lorenz factors γ and occupy a small spatial volume dV. In the mirror rest frame, the magnetic field is stationary and the

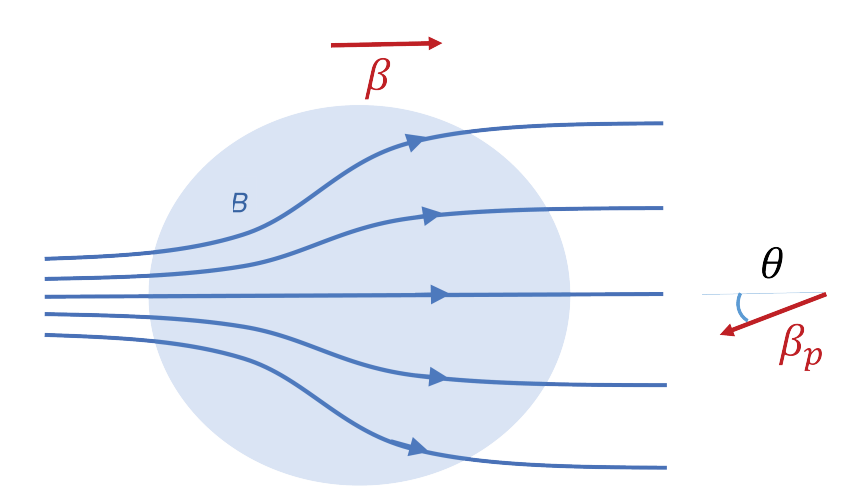


Figure 3.19: Sketh of particle interaction with a strong magnetic mirror moving with a plasma element.

energy of the particles does not change during a reflection. It can be demonstrated by direct calculation that, in the laboratory frame, the energy of the particles after a reflection is given by

$$\gamma' = \Lambda \gamma, \tag{3.66}$$

with the scaling factor

$$\Lambda = \frac{1 + \beta^2 - 2\beta \cdot \beta_p}{1 - \beta^2}.\tag{3.67}$$

Obviously, particles get energized when $\Lambda > 1$. Simultaneously, one can show that a small

volume element filled by the particles gets compressed along the axis of the mirror according to

$$dV' = dV/\Lambda, \tag{3.68}$$

implying that the process of acceleration leads to stronger spatial clusterization of particles. Relation (3.68) holds when particles propagating with the same pitch angle θ , also have the same parallel velocities $\beta_p \cos \theta$. This is possible for the ultrarelativistic case, $\beta_p \to 1$. The ultrarelativistic case also ensures that the factor Λ depends on the first order of β , which makes the acceleration most efficient.

Similarly, one can address the "geometric" dispersion, that is, dispersion due to different pitch angles of particle velocities. One can show that these pitch angles become progressively closer to each other (and to the axis of the mirror) after each reflection with $\Lambda > 1$. If a beam of ultrarelativistic particles is moving within a small collimation angle $d\theta$ around the angle θ , then after the reflection, the new collimation angle satisfies:

$$d\theta' = d\theta/\Lambda. \tag{3.69}$$

Reflections where particles get accelerated lead to stronger angular collimation of the particle beam.

As discussed in Section 3.4, ultrarelativistic particles in runs with $B_0 \lesssim \delta B_0$ have power-law energy distribution functions, $f(\gamma)d\gamma \propto \gamma^{-\alpha} d\gamma$. Based on the consideration presented above, we may analyze the probability density functions of the density, P(n), for such particles. For that consider a small volume of a given number of nearly monoenergetic particles. According to Equation (3.68), as these particles get energized by a factor Λ , the density grows as $n' = \Lambda n$. This together with Equation (3.66) implies their density increases proportionally to their energy, $n \propto \gamma$. The volume occupied by such an element, however, decreases inversely proportionally to n, reducing in this war the fractional volume it represents. The probability

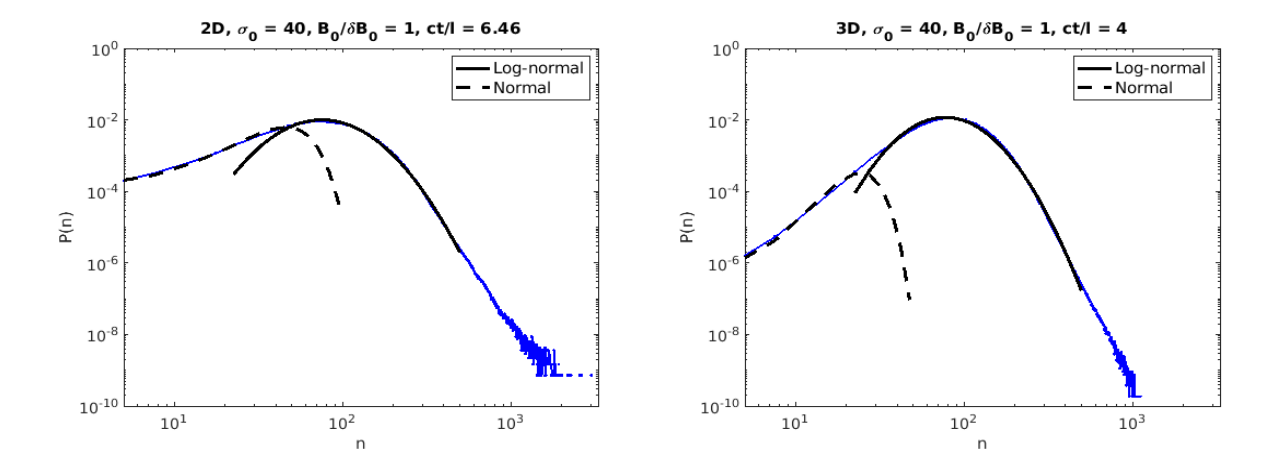


Figure 3.20: Probability density function of particle density n (number of particles per cell) for 2.5D run IV (left) and 3D run IX (right) simulations, both with $\sigma_0 = 40$. Both curves are well approximated by a log-normal distribution around the peak and a normal distribution at low particle density ($n \ll 100$).

to observe density n at a given point in space (or the fractional volume with the densities in the interval [n, n + dn]) is therefore:

$$P(n) dn \propto n^{-\alpha - 1} dn, \tag{3.70}$$

which suggests that the spatial distribution of the accelerated particles is also strongly intermittent and described by power-law probability density functions.

Numerical results

Here we compare our phenomenological predictions to 2.5D simulations (runs II and IV) and 3D simulations (runs IX and X). With the parameters chosen, the inertial scale is resolved in both 2.5D and 3D simulations. The initial gyroradius is resolved in 2.5D but unresolved in 3D runs.

Figure 3.20 shows the distribution of the plasma density obtained in our numerical simulations. The bulk of the distribution function has intermittent (non-Gaussian) statistics and seems to be well approximated by the log-normal distribution, which is consistent with

the prediction of the previous section. At low densities, the numerical curve is, however, better approximated by the normal distribution. This may reflect the fact that the density measurements in particle-in-cell simulations are affected by statistical noise that becomes progressively stronger when particle occupation numbers per cell become progressively smaller.¹²

The left column of Figure 3.21 shows the time evolution of the particle-energy pdf in each simulation. A quasi-steady state with a high-energy power-law tail is reached at (or within a dynamical time $\lambda/U_{\rm rms}$ of) the relaxation time $t_{1/2}$, defined as the time when the total energy in electromagnetic fluctuations has decreased to half the energy in the initial magnetic fluctuations, suggesting that the energization of ultrarelativistic particles forming the power-law tail happens mostly at $t \lesssim t_{1/2}$, while the bulk of the plasma continues to be heated afterward. Also, a comparison with similar runs by Comisso and Sironi (2019, Figures 9 and 11) suggests that at the beginning of the initial-magnetic-field relaxation, the particle acceleration is mostly provided by magnetic reconnection events, while by $t \sim t_{1/2}$ the energization process is taken over by interactions with random turbulent fluctuations developed in the system. (This statement should be understood in a statistical sense, meaning that the particle energy distribution function evolves differently in these two regimes. As for individual particles, their acceleration to high energies involves two stages, even in a quasi-steady state developed at $t_{1/2}$. As shown by Comisso and Sironi (2019), in the initial particle injection stage, rapid particle acceleration is provided by reconnection events, while in the second stage, a gradual stochastic Fermi-type acceleration is provided by interactions with turbulent fluctuations; see also Wong et al. (2020) and our discussion of stochastic acceleration in Sections 3.4 and 3.5.) Since in decaying turbulence the velocity of bulk plasma fluctuations keeps declining at later times, the turbulent acceleration becomes progressively less efficient beyond $t_{1/2}$ as well. We may therefore conclude that the most efficient nonthermal particle acceleration by turbulent fluctuations is achieved on a time scale of $t_{1/2}$.

¹²We note that VPIC uses first-order particle interpolation.

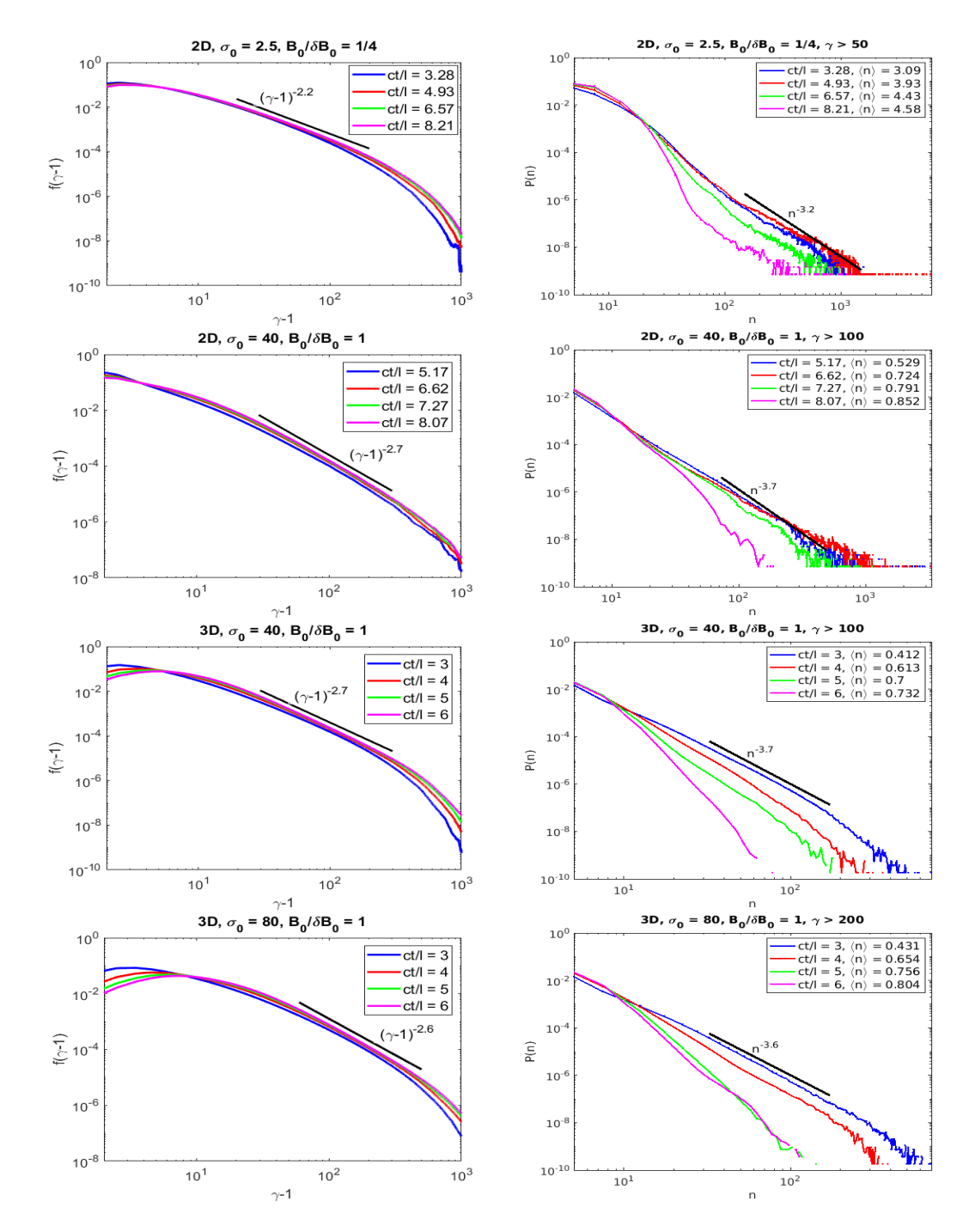


Figure 3.21: Left column: Particle energy pdfs. Quasi-steady states with well-established power-law tails are reached within one or two light-crossing times l/c of the electromagnetic fluctuation energy falling off to half of its initial value. Right column: Particle density pdfs for ultrarelativistic particles. Evidence of strong intermittency (non-Gaussianity) can be seen in the large-density power-law tails. The power slopes α and $\alpha+1$ are given for the reader's orientation.

The right column of Figure 3.21 shows the time evolution of the density pdf calculated only for the energetic particles in each simulation.¹³ We see clear evidence of strong intermittency of density fluctuations associated with the accelerated particles, indicated by power-law tails of the corresponding density distributions. As with Figure 3.20, our 2.5D and 3D simulations (runs IV and IX) produce qualitatively similar results. Comparison of 3D cases IX and X suggests that the power-law tails become better defined at larger magnetizations $\tilde{\sigma}_0$. Around the turbulence relaxation times $t_{1/2}$, the observed power laws are broadly consistent with Equation (3.70). At $t > t_{1/2}$, that is, after the phase of active particle acceleration, the density pdfs steepen and may be expected to eventually evolve toward the distribution functions of the bulk plasma particles.

The log-normal or power-law distributions of the density fluctuations are related to the spatially intermittent, non-space-filing structures formed by turbulence. Such structures are known to affect energy dissipation and plasma heating. As an illustrative example, we consider the intermittency of synchrotron radiation that may be generated in relativistic turbulence. We assume that the medium is optically thin and that the synchrotron cooling time significantly exceeds the particle acceleration time. The average power P of synchrotron radiation emitted by an ultrarelativistic electron propagating at a pitch angle θ is given by

$$P = 2c\sigma_T \gamma^2 \frac{B^2}{8\pi} \beta^2 \sin^2 \theta, \tag{3.71}$$

where

$$\sigma_T = \frac{8\pi}{3} \left(\frac{e^2}{m_e c^2} \right)^2 \tag{3.72}$$

is the Thomson cross-section of the electron. Our numerical code does not include radiation,

¹³In these measurements, the density is not produced by the code as in Figure 3.20, but rather directly calculated by counting the number of energetic particles in each cell. As the particle population numbers are large, the statistical noise does not noticeably affect the measurements. We verified this by constructing the same density pdfs by using larger cells, where the noise is smaller. We did not observe a significant difference with the presented results.

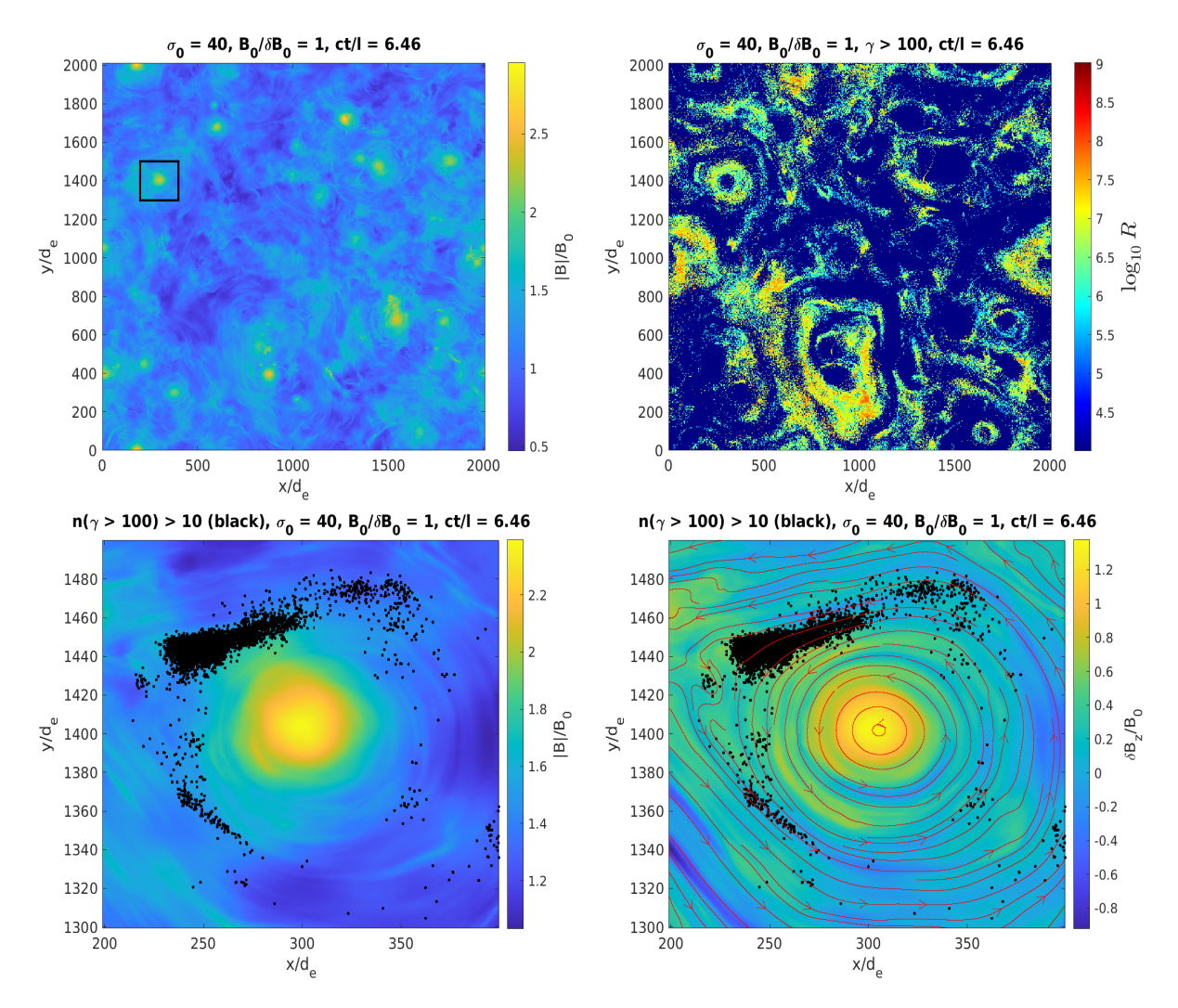


Figure 3.22: Top left: The color map shows the distribution of magnetic-field strength in the simulation domain. Top right: The color map shows the synchrotron radiation proxy $R = \sum_i \gamma_i^2 \beta_i^2 \sin^2 \theta_i B^2 / B_0^2$, where the sum is over the electrons in each cell in Run II and only the energetic particles with $\gamma > 100$ are taken into account. This is a proxy of the synchrotron radiation that would be emitted by electrons if this effect was included in the simulation. Note the logarithmic scale used in the color code, which implies very strong variations of the intensity of radiation in the simulation domain (the bottom of the color bar identifies all cells where $R < 10^4$). Bottom left: An enlarged subdomain indicated by the square in the top left panel. The color map shows the total magnetic field |B| and the black dots identify cells where there are more than 10 energetic ($\gamma > 100$) particles. Bottom right: The color map shows the magnetic fluctuations in the z direction δB_z . The field lines of the in-plane magnetic field δB_{\perp} are shown in red. The clusters of particles seem to concentrate in the vicinity of magnetic structures and align with the magnetic field lines. For the reader's orientation, we note that the gyroradius of ultrarelativistic particles scales in the presented simulation as $\rho_e \approx (\gamma/10)d_e$.

but we note that the radiation power is proportional to $\gamma^2 B^2 \beta^2 \sin^2 \theta$, so we may study the proxy to the density of radiative losses by analyzing the distribution of the local dimensionless quantity $R = \sum_{V} \gamma_i^2 (B/B_0)^2 \beta_i^2 \sin^2 \theta_i$, where we sum over all the electrons contained in a given small volume V. The top panels of Figure 3.22 illustrate the spatial distribution of the magnetic field and the radiation proxy R in run IV. This Figure suggests that relativistic turbulence generates very strong, spatially intermittent variations of the radiation power density in the simulation domain. For instance, 50% of the energetic radiation coming from the particles with $\gamma > 100$ (the top right panel of Figure 3.22), is generated in just 3.3% of the volume of the domain, while 80% of the radiation comes from about 10% of the volume.

The bottom panels of Figure 3.22 show a zoomed-in region of the simulation domain, which illustrates the clusterization of energetic particles with $\gamma > 100$. Fast particles seem to be concentrated in the vicinity of a strong magnetic structure, and the shapes of their clusters follow the morphology of the magnetic field lines. This may also be consistent with the expectation that the interaction of particles with magnetic structures plays an important role in their acceleration, as discussed in Sections 3.4 and 3.5.

3.7 Discussion

Using a two-fluid model, we derived dynamical equations for the turbulent fluctuations of a strongly magnetized, relativistically hot plasma assuming nonrelativistic bulk motion. In the inertial range, $k_{\perp}d_{\rm rel}\ll 1$, the equations become identical to those of nonrelativistic reduced MHD, with the electric fluctuations in place of the bulk kinetic fluctuations. Indeed, we saw in fully relativistic particle-in-cell simulations with $B_0/\delta B_0=3$ (runs V and VI) that the energy spectrum is dominated by magnetic and electric fluctuations in approximate equipartion. In these simulations, the total energy (magnetic plus electric) in the inertial range exhibits a spectrum close to that of Alfvénic turbulence, $W_{k_{\perp}} 2\pi k_{\perp} \propto k_{\perp}^{-3/2}$.

The similarity to nonrelativistic reduced MHD was also seen to manifest in the scale-

dependent dynamic alignment between magnetic and electric fluctuations, and this observation can help us understand the energy spectrum. We found that magnetic and electric fluctuations become progressively more orthogonal to each other towards smaller scales, with the cosine of the angle between them scaling close to $\cos \varphi_{\ell} \propto \ell^{0.25}$. Based on the analogy with the nonrelativistic case, we proposed that such an alignment reduces the strength of nonlinear interactions in the relativistic dynamics, thus explaining the observed -3/2 scaling of the energy spectrum. We also note that run VI, with stronger initial magnetic fluctuations than run V, displayed a slightly shallower scaling of the alignment angle. This may be related to a shorter inertial interval of turbulence due to a larger relativistic inertial scale of thermal particles.

Furthermore, the electric and magnetic energy spectra show an excess of magnetic energy over electric, which becomes progressively smaller at smaller scales, analogous to the generation of the so-called residual energy, that is, the excess of magnetic over kinetic energy known in the nonrelativistic quasi-neutral case. The measured spectrum of the residual energy is close to $R_{k_{\perp}} 2\pi k_{\perp} \propto k_{\perp}^{-2.4}$, which is slightly steeper than its nonrelativistic counterpart, indicating an interesting difference with the nonrelativistic case.

To better study relativistic kinetic-scale turbulence we used strong-guide-field runs VII (with box size similar to other 2.5D runs) and VIII (small box run), which resolve better the sub- d_e range at the expense of a reduced inertial range. Such kinetic-scale turbulence may be relevant for energy dissipation and particle energization in a turbulent plasma, and it is somewhat analogous to the kinetic-Alfvén or inertial-Alfvén turbulence previously studied in nonrelativistic cases. However, we demonstrated that the kinetic-scale energy cascade in the ultrarelativistic case is qualitatively different from the nonrelativistic counterparts.

First, contrary to non-relativistic kinetic-Alfvén or inertial-Alfvén turbulence, the thermal and inertial effects are necessarily of the same order in the ultrarelativistic kinetic-scale turbulence. Second, the scaling of the energy spectrum is slightly steeper than k^{-3} , which is different from the kinetic-Alfvén case (the energy spectrum $\sim k^{-8/3}$ (e.g., Alexandrova

et al., 2009; Boldyrev and Perez, 2012; TenBarge and Howes, 2012; Boldyrev et al., 2015; Zhou et al., 2023)) and the inertial-Alfvén case (the spectrum is $\sim k^{-11/3}$ (e.g., Loureiro and Boldyrev, 2018; Milanese et al., 2020)).

Based on the equations derived from the two-fluid model, we proposed that in the ultrarelativistic case, the energy spectrum is consistent with the Kraichnan spectrum of incompressible 2D turbulence corresponding to the enstrophy cascade, k^{-3} or $k^{-3} \ln^{-1/3}(k/k_0)$ if the intermittency corrections are taken into account. This intermittency-corrected Kraichnan spectrum is seen to be a good match for run VII. The small-box run VIII had stronger initial magnetic fluctuations at the kinetic scales. As a result, the "contamination" of the spectrum by the O-mode was stronger and had to be removed by hand. The resulting spectrum was close to a Kraichnan k_{\perp}^{-3} scaling.

We noted that the kinetic-scale cascade may be affected by Landau damping which, in general, is not weak in the relativistic case. The spectrum, however, exhibits a near power-law behavior despite being affected by the damping. We conjectured that this might be the consequence of the non-locality of kinetic-scale turbulence.

In the astrophysics community, the study of relativistic plasma turbulence is largely motivated by its efficiency as a particle accelerator, observed in multiple numerical simulations presented here and elsewhere (e.g., Zhdankin et al., 2017, 2018b,a, 2019, 2021; Comisso and Sironi, 2018, 2019, 2021; Wong et al., 2020; Nättilä and Beloborodov, 2021; Demidem et al., 2020; Vega et al., 2022b, 2023a, 2024b,a; Chernoglazov et al., 2021; Nättilä and Beloborodov, 2021), potentially explaining the nonthermal ultrarelativistic particles ubiquitous in astrophysical plasmas. In this chapter, we proposed a phenomenological description of nonthermal relativistic particle acceleration in magnetically dominated strong Alfvénic turbulence. We argue that in the limit of strong magnetization, $\tilde{\sigma} \gtrsim 1$, particle acceleration is universal in that it depends only on the relative strength of the guide field and the magnetic turbulent fluctuations. The process of acceleration is governed by the conservation of magnetic moment. In the case of a strong guide field, $B_0 \gg \delta B_0$, the particle's magnetic moment

is conserved and the acceleration is provided by magnetic curvature drifts. The curvature acceleration energizes particles in the direction parallel to the magnetic field lines, resulting in a log-normal tail of particle energy distribution function. The situation is qualitatively different in the case of a moderate or small guide field, $B_0 \lesssim \delta B_0$. In this case, as the gyroradius of an energetic particle exceeds the inner scale of turbulence (in our case, $d_{\rm rel}$), interactions with intense turbulent structures like current sheets can break the particle's magnetic moment. Magnetic mirror effects become important at such energies, resulting in power-law energy distributions of accelerated particles. The proposed phenomenological picture is consistent with available numerical simulations, as shown in Sections 3.4 and 3.5.

Finally, we proposed, based on particle-in-cell numerical simulations and analytical modeling, that magnetically dominated relativistic turbulence is essentially strongly compressible and it naturally generates spatially intermittent distributions of plasma particles. The bulk of the plasma particles, with energies comparable to the average energy (we call it the "thermal energy" $\gamma_{\rm th}$), have an essentially non-Gaussian, log-normal density distribution. The "run-away" fraction of particles that are accelerated to much higher energies $\gamma \gg \gamma_{\rm th}$, exhibit even more intermittent statistics, with the power-law distribution functions of their number density $P(n)dn \propto n^{-\beta}dn$. Based on numerical observations and phenomenological modeling, we argue that the scaling exponents are related approximately as $\beta = \alpha + 1$, where α is the spectral index in the power-law tail of the particle energy pdf.

The strongly non-Gaussian statistics of particle distribution are related to the formation of structures or density "clumps" in the simulation domain. Such strong spatial intermittency may have important implications for energy dissipation in relativistic turbulence. As an example, we have considered the distribution of energetic synchrotron radiation that can be produced by particles with $\gamma \gg \gamma_{\rm th}$ in such turbulence. We observed that the contrast of the radiation intensity spans many orders of magnitude over a simulation domain, with the majority of the radiated energy originating in a small fraction of the plasma volume.

4 CONCLUSIONS

In this dissertation, we explored magnetized plasma turbulence numerically and phenomenologically, in both the nonrelativistic and relativistic regimes. Our study of the former, presented in Chapter 2, focused on plasma environments with $\beta_e \ll \beta_i \sim 1$, which can be found in the magnetosheath and in the solar wind close to the solar corona. This opens up the range between the electron inertial and gyro-scales to turbulent fluctuations. We reviewed iKAW phenomenology, which is based on an electron fluid model and produces the correct scaling law for the magnetic energy spectrum observed in numerical simulations in the range $d_e^{-1} < k_{\perp} < \rho_e$.

We analyzed 2.5D and 3D simulations and found the low electron beta environment to be fertile ground for electron scale current sheets, some of which exhibited signatures of electron-only magnetic reconnection, like an outflow of Alfvénic electron jets. The 3D simulation showed an enhanced electron inflow relative to the 2.5D case, which may be attributed to a field-parallel outflow, as was reported in Pyakurel et al. (2021).

We used the pressure-strain interaction as a measure of energy dissipation in the 3D simulation and found it to be strongly intermittent and concentrated on current sheets. The most intense dissipation event found was seen to correspond to electron-only magnetic reconnection.

The lowest electron beta achieved in our simulations was $\beta_e = 0.04$ in 2.5D and $\beta_e = 0.1$ in 3D, both providing a very small scale separation. To improve on our study of iKAW turbulence, a 3D simulation with a lower electron beta than either one analyzed here would be highly desirable.

In astrophysics, there is interest in relativistic plasma turbulence as a particle accelerator. In Chapter 3 we presented a numerical and phenomenological study of decaying magnetically dominated plasma turbulence, where the magnetic fluctuations seeded at the initialization were seen to quickly heat the plasma to strongly relativistic temperatures, while the bulk

motion was only mildly relativistic. Approximating the bulk motion as nonrelativistic and the microscopic motion as ultrarelativistic, we used a two-fluid model to derive a scaling law for the electromagnetic energy spectrum both in the inertial and in the kinetic ranges. Our phenomenological model for the inertial range was seen to be analogous to nonrelativistic reduced MHD with electric fluctuations in place of bulk velocity fluctuations. In the kinetic range, the turbulent cascade is reminiscent of the enstrophy cascade in 2D incompressible hydrodynamic turbulence. Our numerical results were in good agreement with both models.

Nonthermal particle energization was observed in our simulations of relativistic plasma turbulence, with the particle energy pdf developing a power-law tail for weak guide field, $B_0 \lesssim \delta B_0$. As the guide field is increased, the slope steepens, eventually giving way to a log-normal distribution when $B_0 \gtrsim 3\delta B_0$. We argued that this can be understood in terms of the acceleration mechanism that dominates. When the guide field is strong, the magnetic moment of the particles is conserved and they are accelerated by the parallel electric field (at early times) and by the curvature and polarization drifts. In this case, acceleration is in the field-parallel direction, reducing the pitch angle and effectively neutralizing acceleration by magnetic mirrors. This results in a log-normal particle energy distribution. When the guide field is weak, particles can experience interactions with magnetic structures that break magnetic moment conservation, resulting in pitch angle scattering. Thus, particles may be trapped in regions of the phase space where their pitch angle is large and they are efficiently accelerated by magnetic mirrors, resulting in power-law tails in the particle energy distribution.

Finally, the space distribution of ultrarelativistic particles was seen to be strongly intermittent in our simulations with $B_0 \lesssim \delta B_0$, perhaps the result of acceleration by magnetic mirrors. A study of the space intermittency of ultrarelativistic particles in the simulations with strong guide field is pending.

Another natural continuation of our work on relativistic plasma turbulence would be a statistical study of current sheets, magnetic reconnection, and energy dissipation. The latter would require finding a relativistic generalization of the pressure-strain interaction.

We hope that the work that went into this thesis leaves the field of plasma turbulence at least a tiny step closer to completion.

A LOW-FREQUENCY WAVES IN A RELATIVISTIC PLASMA

We consider a strongly magnetized, magnetically dominated pair plasma, where the cyclotron frequency is much larger than the plasma frequency and the frequency of the considered wave modes. Here, we imply the relativistic versions of the cyclotron and plasma frequencies that depend on the details of the particle distribution function, see the discussion below. In what follows, we denote by $\omega_{pe} = \sqrt{4\pi n_0 e^2/m_e}$ the nonrelativistic electron plasma frequency. We also assume that the electron gyroscale is negligibly small, $k_{\perp}^2 \rho_e^2 \ll 1$.

It is convenient to choose the coordinate frame such that $\mathbf{k} = (k_{\perp}, 0, k_z)$, where z is the direction along the background magnetic field. Under these conditions, the plasma dielectric tensor simplifies to:

$$\varepsilon_{lm} = \begin{pmatrix} 1 & 0 & 0 \\ 0 & 1 & 0 \\ 0 & 0 & P \end{pmatrix},\tag{A.1}$$

where the function $P(\omega, \mathbf{k})$ depends on the particle distribution function and will be discussed later. In order to find the frequencies and polarizations of the plasma modes, we need to solve the wave equation:

$$\left(k^2 \delta_{lm} - k_l k_m - \frac{\omega^2}{c^2} \varepsilon_{lm}\right) E_m = 0,$$
(A.2)

which in the matrix form reads

$$\begin{pmatrix} k_z^2 - \frac{\omega^2}{c^2} & 0 & -k_z k_\perp \\ 0 & k^2 - \frac{\omega^2}{c^2} & 0 \\ -k_z k_\perp & 0 & k_\perp^2 - \frac{\omega^2}{c^2} P \end{pmatrix} \begin{pmatrix} E_x \\ E_y \\ E_z \end{pmatrix} = 0.$$
 (A.3)

To obtain nontrivial solutions, we equate the determinant of the matrix to zero, obtaining:

$$\left(k^2 - \frac{\omega^2}{c^2}\right) \left(\left[k_z^2 - \frac{\omega^2}{c^2}\right] \left[k_\perp^2 - \frac{\omega^2}{c^2}P\right] - k_z^2 k_\perp^2\right) = 0. \tag{A.4}$$

Setting the first multiplicative term to zero, one gets the dispersion relation of the electromagnetic *extraordinary* mode,

$$\omega^2 = k^2 c^2, \tag{A.5}$$

whose electric-field polarization is normal to both the background magnetic field and the wave vector,

$$\boldsymbol{E}_{X} = (0, E_{y}, 0). \tag{A.6}$$

By equating the second term to zero, we obtain

$$k_{\perp}^{2} + k_{z}^{2}P - \frac{\omega^{2}}{c^{2}}P = 0. \tag{A.7}$$

In order to specify the function P in this expression, we need to know the particle distribution function. Following (Godfrey et al., 1975; Arons and Barnard, 1986; Gedalin et al., 1998), we assume that the particle velocity distribution function is one-dimensional, $f(\mathbf{u}) = \tilde{f}(u_z)\delta(\mathbf{u}_\perp)$, with the normalization

$$\int f(\boldsymbol{u}) d^3 u = \int_{-\infty}^{\infty} \tilde{f}(u_z) du_z = 1.$$
(A.8)

In this expression, we denote $u_z = v_z/\sqrt{1 - v_z^2/c^2}$, where v_z is the particle velocity, so that $\gamma^2 = 1 + u_z^2/c^2$. This simplifying assumption is motivated by two independent considerations. First is the fact that in a very strong guide magnetic field such as that relevant, e.g., for pulsar magnetospheres and winds, (e.g., Arons and Barnard, 1986; Gedalin et al., 1998), the

field-perpendicular components of particle momenta are significantly reduced with respect to their field-parallel ones due to strong synchrotron cooling. Second is the numerical observation that magnetically dominated Alfvénic turbulence ($\tilde{\sigma} \gg 1$) strongly heats plasma particles in the field-parallel rather than field-perpendicular direction (Nättilä and Beloborodov, 2022). We also note that in astrophysical applications, plasma can stream along the background magnetic field with relativistic velocity. Our consideration will apply to the plasma rest frame, where we assume that the particle momentum distribution is symmetric with respect to the $\pm z$ -directions.

In the considered limit of a very strong large-scale magnetic field and a one-dimensional particle velocity distribution function, one obtains for a pair plasma (Gedalin et al., 1998):

$$P(\omega, \mathbf{k}) = 1 - \frac{2\omega_{pe}^2}{\omega^2} W(\omega, k_z).$$
(A.9)

The function W in this expression is given by

$$W = -\frac{\omega^2}{k_z} \int_{-c}^{c} \frac{1}{\omega - k_z v_z + i\nu} \frac{d\tilde{f}}{dv_z} dv_z, \tag{A.10}$$

where $\nu \to +0$ is needed to describe collisionless Landau damping. Let us first discuss the limit of large parallel phase velocity, $\omega \gg k_z v_{\rm th}$, where $v_{\rm th}$ is the characteristic (e.g., thermal) speed of the particle distribution. Obviously, this limit can also describe the case of cold nonrelativistic plasma, when plasma temperature is negligibly small. In this limit, we can neglect the imaginary part and integrate Equation (A.10) by parts:

$$W = \omega^2 \int_{-c}^{c} \frac{\tilde{f}}{(\omega - k_z v_z)^2} dv_z \approx \int_{-c}^{c} \tilde{f} dv_z = \int_{-\infty}^{\infty} \left(1 - \frac{v_z^2}{c^2}\right)^{3/2} \tilde{f} du_z \equiv \left\langle \frac{1}{\gamma^3} \right\rangle. \tag{A.11}$$

One can then define the plasma frequency for relativistic pair plasma as follows:

$$\omega_p^2 \equiv 2\omega_{pe}^2 \left\langle \frac{1}{\gamma^3} \right\rangle,\tag{A.12}$$

which provides the relativistic generalization of the nonrelativistic expression. The function P now has the form

$$P = 1 - \frac{\omega_p^2}{\omega^2}.\tag{A.13}$$

Substituting this function into Equation (A.7), we obtain the dispersion relation:

$$\omega^2 = \frac{\left(\omega_p^2 + k^2 c^2\right) \pm \sqrt{\left(\omega_p^2 + k^2 c^2\right)^2 - 4\omega_p^2 k_z^2 c^2}}{2}.$$
(A.14)

Here, the positive sign in front of the square root corresponds to the *ordinary* mode, while the negative sign to the *Alfvén* mode, which transforms into the inertial-Alfvén mode at $k > \omega_p/c$. In the case of cold plasma, both solutions are allowed. However, in our case of relativistic plasma temperature, the latter solution is not applicable as it would correspond to the parallel phase speed smaller than the thermal speed. We, therefore, analyze only the expression corresponding to the "+" sign in Equation (A.14).

In the long-wave limit, $kc \ll \omega_p$, this expression gives $\omega = \omega_p$, and the corresponding electric field is polarized along the background magnetic field, $\mathbf{E} = (0, 0, E_z)$. In the opposite limit, $kc \gg \omega_p$, we get $\omega = kc$. One can check that in this case, the electric field lies in the x-z plane and it is normal to the wave vector \mathbf{k} . In the limit of quasi-perpendicular wave propagation, $k_{\perp} \gg k_z$, the dispersion relation for the ordinary mode simplifies to

$$\omega^2 = \omega_p^2 + k^2 c^2 \tag{A.15}$$

for any value of the wavenumber, with the electric polarization being nearly aligned with the background magnetic field,

$$\mathbf{E}_{\mathcal{O}} \approx (0, 0, E_z). \tag{A.16}$$

We now consider the limit of low phase velocities, $\omega \sim k_z v_{\rm th}$, which will give us the dispersion relation for the Alfvén mode. In this limit, the dispersion relation depends on the details of the particle distribution function. As was discussed previously, magnetically dominated turbulence with $\tilde{\sigma}_0 \gg 1$ leads to ultrarelativistic particle heating, with $v_{\rm th} \approx c$. We will therefore assume relativistic distribution functions in our consideration. For instance, one can consider the one-dimensional equilibrium Maxwell-Jüttner distribution,

$$\tilde{f}(u_z) = \frac{1}{2K_1(1/\theta)c} \exp(-\gamma/\theta), \qquad (A.17)$$

where $\gamma = 1/\sqrt{1 - v_z^2/c^2}$, K_1 is the modified Bessel function of the second kind, and $\theta = k_B T/mc^2$. For ultrarelativistic particle temperatures, $\theta \gg 1$, one can replace $K_1(1/\theta) \approx \theta$. In what follows, we will also need to know the enthalpy density w corresponding to this distribution. For ultrarelativistic one-dimensional gas, the internal energy density and pressure are related as $P_{\parallel} = u$, and we derive the normalized enthalpy density:

$$w = (u + P_{\parallel})/n_0 m_e c^2 = 2\theta. \tag{A.18}$$

We now assume without loss of generality that $k_z > 0$, and rewrite the expression for the W function (A.10) as follows:

$$W = -\frac{\omega^2}{k_z^2 c} \int_{-c}^{c} \frac{1}{(1 - v_z/c) - (1 - \omega/k_z c) + i\nu} \frac{d\tilde{f}}{dv_z} dv_z.$$
 (A.19)

The distribution function declines fast when particle energy exceeds the thermal energy, that is when $\gamma > \theta$, or equivalently $1-v_z/c < 1/(2\theta^2)$, where we have approximated $1/\gamma^2 \approx 2(1-v_z/c)$. The integral is thus dominated by the velocity values satisfying $1-v_z/c \sim 1/(2\theta^2)$. Therefore, the behavior of the ultrarelativistic W-function depends on whether $1-\omega/k_zc$ is greater or smaller than the small parameter $1/(2\theta^2)$. It is easy to see that this is just the condition that compares the parallel phase velocity of the waves, ω/k_z , with the velocity associated with the

thermal motion of the particles, $v_{\rm th}=c\sqrt{1-1/\theta^2}$. These two asymptotic limits should be considered separately; we refer the reader to Godfrey et al. (1975); Gedalin et al. (1998) for a detailed analysis. For our consideration of the ultrarelativistic Alfvén mode with $k_z\ll k_\perp$, the essential limit is

$$\left|1 - \frac{\omega}{k_z c}\right| \ll \frac{1}{2\theta^2}.\tag{A.20}$$

In this limit, the imaginary part of the distribution function is negligible. Moreover, in this case, one can neglect $1 - \omega/k_z c$ with respect to $1 - v_z/c$ in the denominator. The asymptotic expression for the W-function in this limit can then be found from Equation (A.19) where we integrate by parts,

$$W \sim \frac{\omega^2}{k_z^2 c^2} \int_{-c}^{c} \frac{1}{(1 - v_z/c)^2} \tilde{f} \, dv_z \sim \frac{\omega^2}{k_z^2 c^2} \int_{0}^{c} 4\gamma^4 \, \tilde{f} \, dv_z = \frac{\omega^2}{k_z^2 c^2} \int_{0}^{\infty} 4\gamma \, \tilde{f} \, du_z = \frac{\omega^2}{k_z^2 c^2} \, 2 \, \langle \gamma \rangle \,. \tag{A.21}$$

The average value of γ depends on the distribution function. For the considered ultrarelativistic Maxwell-Jüttner distribution, one gets $\langle \gamma \rangle = \theta$. Substituting this into Equation (A.9), one obtains

$$P = 1 - \frac{4\theta\omega_{pe}^2}{k_z^2 c^2} \approx -\frac{4\theta\omega_{pe}^2}{k_z^2 c^2}.$$
 (A.22)

Equation (A.7) then leads to the dispersion relation of the ultrarelativistic Alfvén mode

$$\omega^{2} = k_{z}^{2} c^{2} \left(1 - \frac{k_{\perp}^{2} c^{2}}{4\omega_{pe}^{2} \theta} \right) = k_{z}^{2} c^{2} \left(1 - \frac{k_{\perp}^{2} d_{\text{rel}}^{2}}{w^{2}} \right), \tag{A.23}$$

where we have defined the relativistic inertial scale of a pair plasma as

$$d_{\rm rel}^2 = c^2 \frac{\theta}{\omega_{pe}^2} = c^2 \frac{w}{2\omega_{pe}^2}.$$
 (A.24)

Recalling that our derivation is valid under the assumption that $1 - \omega^2/k_z^2c^2 \ll 1/\theta^2$, we see

that the Alfvén dispersion relation (A.23) holds up to the scales $k_{\perp}^2 d_{\rm rel}^2 \sim 1$. At perpendicular scales comparable to the relativistic inertial scale, the thermal effects become essential and Landau damping becomes strong.

Using Equations (A.3) and (A.22) we get the polarization of the Alfvén mode:

$$\mathbf{E}_{A} = (E_x, 0, E_z), \quad \frac{E_z}{E_x} \approx \frac{k_z k_\perp d_{\text{rel}}^2}{w^2} \ll 1,$$
 (A.25)

so that this mode is nearly potential.

Finally, we discuss the Alfvén wave for the case of the so-called "waterbag" distribution, which has cut-offs in the momentum space. Such functions were used to study relativistic beams in a plasma (e.g., Roberts and Berk, 1967; Davidson and Startsev, 2004), to model pair plasma distributions in pulsar magnetospheres (Arons and Barnard, 1986), and analyzed in detail in Gedalin et al. (1998). We will however modify the "waterbag" distribution by smoothing out its sharp edges. This can be done in many different ways by introducing various regularizations whose particular forms are not relevant for our consideration. We may, for example, adopt the following model function

$$\tilde{f}(u_z) = A \frac{1}{e^{\frac{\gamma - \gamma_m}{\theta}} + 1}.$$
(A.26)

In the limit $\theta/\gamma_m \to 0$, such a distribution approaches (up to the normalization constant A) the Heaviside step function $H(\gamma_m - \gamma)$. We however assume that θ is small but nonzero, $0 < \theta/\gamma_m \ll 1$, in which case the sharp boundary of the step function is smoothed over a narrow region $\Delta \gamma \sim \theta$. In the ultrarelativistic case, $\gamma_m \gg 1$, the normalization constant is $A = 1/(2c\gamma_m)$ and the enthalpy density corresponding to such a distribution is given by $w = \gamma_m$. The derivative of the distribution function is then a θ -broadened delta function, $c d\tilde{f}/du_z = A \delta(\gamma - \gamma_m)$, and we can integrate Equation (A.10) to obtain (Gedalin et al.,

1998):

$$W = \frac{1}{\gamma_m} \frac{\omega^2}{k_z^2 v_m^2} \frac{1}{(\omega^2 / k_z^2 v_m^2 - 1)},$$
(A.27)

where $1/\gamma_m^2 = 1 - v_m^2/c^2$. The resulting dispersion relation for the Alfvén mode is then

$$\omega^2 = k_z^2 c^2 \frac{1 + k_\perp^2 v_m^2 \gamma_m / 2\omega_{pe}^2}{1 + k_\perp^2 c^2 \gamma_m / 2\omega_{pe}^2} = k_z^2 c^2 \frac{1 + \frac{v_m^2}{c^2} k_\perp^2 d_{rel}^2}{1 + k_\perp^2 d_{rel}^2},$$
(A.28)

where we use the relativistic inertial scale

$$d_{\rm rel}^2 = c^2 \frac{\gamma_m}{2\omega_{pe}^2} = c^2 \frac{w}{2\omega_{pe}^2}.$$
 (A.29)

These expressions agree with our hydrodynamic result (3.18). For perpendicular scales larger than the inertial scale, $k_{\perp}^2 d_{\rm rel}^2 \ll 1$, we obtain the familiar ultrarelativistic Alfvén mode, cf. (A.23),

$$\omega^2 \approx k_z^2 c^2 \left(1 - \frac{k_\perp^2 d_{\rm rel}^2}{\gamma_m^2} \right) = k_z^2 c^2 \left(1 - \frac{k_\perp^2 d_{\rm rel}^2}{w^2} \right), \tag{A.30}$$

while in the opposite, "kinetic" range $k_{\perp}^2 d_e^2 \gg 1$, the dispersion relation changes to

$$\omega^2 \approx k_z^2 v_m^2 \left(1 + \frac{1}{k_\perp^2 d_{\text{rel}}^2 w^2} \right).$$
 (A.31)

The parallel phase velocity of this mode exceeds v_m . The Landau damping is weak if this phase velocity is not too close to v_m , that is if their difference is larger than the boundary broadening, $1/\sqrt{1-\omega^2/k_z^2c^2}-\gamma_m > \theta$. Substituting here expression (A.31), we derive the condition for such a mode to exist:

$$k_{\perp}^2 d_{\rm rel}^2 < \frac{\gamma_m}{2\theta}.\tag{A.32}$$

We note the analogy of the "waterbag" distribution with the Fermi distribution in a degenerate gas. The acoustic-type mode (A.31) appearing at kinetic scales in this case is then analogous to the so-called "zero sound", $\omega \approx kv_F$, existing in a degenerate plasma where the particles have a Fermi distribution with a cutoff at the Fermi speed v_F . We also point out that different kinetic particle distributions lead to similar results for the relativistic Alfvén mode when expressed in terms of the fluid parameters $d_{\rm rel}$ and w; this can be seen from comparing Equations (A.23) and (A.30).

B CURVATURE ACCELERATION: THE LOGARITHMIC FACTOR

Here, we derive the logarithmic factor in the formula (3.54) for the curvature acceleration. For that, we introduce the field-parallel spectrum of the magnetic fluctuations defined as

$$W(k_{\parallel}) dk_{\parallel} = \left(\frac{\delta B_{\perp,0}}{B_0}\right)^2 \frac{k_0}{k_{\parallel}^2} dk_{\parallel}, \tag{B.1}$$

where $k_0 = 1/\ell_0$. The normalization is chosen to satisfy

$$\left(\frac{\delta B_{\perp,0}}{B_0}\right)^2 = \int_{k_0}^{\infty} W(k_{\parallel}) dk_{\parallel}. \tag{B.2}$$

We then divide the interval of the wavenumbers k_{\parallel} into logarithmic sub-intervals $[k_n, k_{n+1}]$, where $k_n = k_0 a^n$. Here n = 0, 1, 2, ... is an integer number, and a > 1 is some scaling factor. The energy contained inside such an interval,

$$W_n = \int_{k_n}^{k_{n+1}} W(k_{\parallel}) dk_{\parallel} = \left(\frac{\delta B_{\perp,0}}{B_0}\right)^2 \frac{a-1}{a^{n+1}}, \tag{B.3}$$

is then associated with the energy contained in the eddies of scale $\ell_n = 1/k_n$. An electron propagating along the magnetic field line will encounter $N_n = \ell_0/\ell_n = a^n$ such eddies. According to formula (3.53), the contribution of the eddies of size ℓ_n to the electron energy gain is then proportional to N_nW_n . To find the total acceleration, we need to sum the contributions of all the eddies, from the largest scale, ℓ_0 , to the smallest one, $\ell_* = 1/k_*$:

$$\sum_{n=0}^{n_*-1} N_n W_n = \left(\frac{\delta B_{\perp,0}}{B_0}\right)^2 \frac{a-1}{a} n_*.$$
 (B.4)

Here, we have introduced the total number of the intervals, n_* , which can be evaluated as:

$$n_* = \log_a \left(\frac{k_*}{k_0}\right) = \frac{\ln(\ell_0/\ell_*)}{\ln(a)}.$$
 (B.5)

Since n_* should be an integer, only the integer part of this expression should be taken into account. We then arrive at the final formula

$$\sum_{n=0}^{n_*-1} N_n W_n = A_{\parallel} \ln\left(\frac{\ell_0}{\ell_*}\right) \left(\frac{\delta B_{\perp,0}}{B_0}\right)^2, \tag{B.6}$$

where

$$A_{\parallel} = \frac{a-1}{a\ln(a)}.\tag{B.7}$$

The numerical factor A_{\parallel} is a rather slowly changing function of the scaling parameter a. For instance, for a=2 we get $A_{\parallel}\approx 0.72$.

In a collisionless plasma where fluctuations of the electric and magnetic fields are relatively small in comparison with B_0 , a charged particle preserves the first adiabatic invariant, the magnetic moment. If the magnetic moment is initially small, it will remain small as the particle gets accelerated. The complete expression for the magnetic moment includes not only field-perpendicular but also field-parallel particle momentum (e.g., Northrop, 1963; Littlejohn, 1983, 1984; Egedal et al., 2008). In a curved magnetic field, as the field-parallel momentum increases during particle acceleration, so should the field-perpendicular momentum. For an ultrarelativistic particle, one may then relate the typical values attained by the particle's parallel and perpendicular momenta as the particle propagates in a curved magnetic field:

$$p_{\perp}^2 \sim p_{\parallel}^2 \gamma^2 \rho_0^2 / R_c^2.$$
 (C.1)

Expressing the particle gyroradius as $\rho_{\perp}^2 = \gamma^2 \rho_0^2 \sin^2 \theta$, we rewrite formula (C.1) for a small pitch angle:

$$\rho_{\perp}^2 \sim \rho_0^4 \gamma^4 / R_c^2$$
. (C.2)

If the particle gyroradus, ρ_{\perp} , is smaller than the inner scale of turbulence, $d_{\rm rel}$, the largest curvature of the magnetic-field lines is provided by the smallest turbulent eddies, with scales $d_{\rm rel}$. The curvature radius can then be evaluated as in formula (3.48) of the main text,

$$R_c \sim d_{\rm rel} \left(\frac{B_0}{\delta B_{\perp}(d_{\rm rel})}\right)^2 \sim \lambda_0 \left(\frac{d_{\rm rel}}{\lambda_0}\right)^{1/3} \left(\frac{B_0}{\delta B_{\perp,0}}\right)^2.$$
 (C.3)

Here, for simplicity, we assumed the Goldreich and Sridhar (1995) scaling of turbulence, $\alpha = 1/3$. Substituting this expression into Equation (C.2), we derive the scaling of the typical

particle gyroradius with the energy:

$$\rho_{\perp} \sim \rho_0 \left(\frac{\rho_0}{\lambda_0}\right) \left(\frac{\delta B_{\perp,0}}{B_0}\right)^2 \left(\frac{\lambda_0}{d_{\rm rel}}\right)^{1/3} \gamma^2. \tag{C.4}$$

This gyroradius becomes comparable to the inner scale of turbulence, d_{rel} , when the particle energy reaches the *critical value*:

$$\gamma_c = \frac{B_0}{\delta B_{\perp,0}} \frac{d_{\rm rel}}{\rho_0} \left(\frac{\lambda_0}{d_{\rm rel}}\right)^{1/3}.$$
 (C.5)

For energies larger than the critical energy, the curvature of the magnetic field lines guiding the particle motion, is provided by the eddies comparable to the particle gyroradius, $\lambda \sim \rho_{\perp}$. In this case, the field curvature radius needs to be estimated as

$$R_c \sim \lambda_0 \left(\frac{\rho_\perp}{\lambda_0}\right)^{1/3} \left(\frac{B_0}{\delta B_{\perp,0}}\right)^2.$$
 (C.6)

Substituting Equation (C.6) into Equation (C.2), we derive the scaling of the particle gyroradius with the Lorenz factor,

$$\rho_{\perp} \sim \rho_0 \left(\frac{\delta B_{\perp,0}}{B_0}\right)^{3/2} \left(\frac{\rho_0}{\lambda_0}\right)^{1/2} \gamma^{3/2}. \tag{C.7}$$

This scaling holds only when ρ_{\perp} is larger than the smallest scale of Alfvénic turbulence, $d_{\rm rel}$. Interestingly, in this limit one can give an alternative derivation of formula (C.1), which is more suitable for our analysis of magnetic turbulence. In an Alfvénic turbulent eddy with the field-perpendicular and field-parallel scales, λ and ℓ , the directions of magnetic field lines are known with the angular uncertainty of $\theta_{\lambda} \sim \lambda/\ell$. Therefore, a particle with a gyroradius $\rho_{\perp} \sim \lambda$ cannot maintain a pitch angle smaller than θ_{λ} . Expressing the (small) particle pitch

angle as p_{\perp}/p_{\parallel} , we write this condition as

$$\frac{p_{\perp}}{p_{\parallel}} \sim \frac{\lambda}{\ell}.$$
 (C.8)

The magnetic-line curvature associated with such an eddy can be evaluated as $R_c \sim \ell^2/\lambda$, and the scale of the eddy guiding the particle motion as $\lambda \sim \rho_{\perp} = \gamma \rho_0 \sin \theta$. One can then express λ and ℓ through ρ_{\perp} and R_c and verify that Equation (C.8) becomes equivalent to Equation (C.1).

Once the energy of an accelerated particle exceeds γ_c , we may use Equation (3.59) to rewrite the energy gain Equation (3.55) as:

$$\Delta_0 \ln(\gamma) \sim 3\phi A_\perp \ln\left(\frac{\gamma_0}{\gamma}\right) \left(\frac{\delta B_{\perp,0}}{B_0}\right)^2.$$
(C.9)

Since the right-hand side of this equation now depends on γ , it is more appropriate to write instead of Equation (C.9) the differential equation for the energy evolution:

$$\frac{d\ln(\gamma)}{dt} = A_0 \ln\left(\frac{\gamma_0}{\gamma}\right),\tag{C.10}$$

where we have denoted

$$A_0 = 3\phi A_{\perp} \left(\frac{\delta B_{\perp,0}}{B_0}\right)^2 \frac{c}{\ell_0}.$$
 (C.11)

Assuming that at t = 0, the particle's energy is γ_c , we can solve Equation (C.10) to get:

$$\ln\left(\frac{\gamma}{\gamma_0}\right) = \ln\left(\frac{\gamma_c}{\gamma_0}\right) e^{-A_0 t}.$$
 (C.12)

For $t \ll 1/A_0$, $\ln(\gamma)$ grows linearly with time. At $t \gtrsim 1/A_0$, the particle gyroradius quickly approaches the outer scale of turbulence, $\gamma \sim \gamma_0$, and the curvature acceleration vanishes.

REFERENCES

Abdo, A. A., M. Ackermann, M. Ajello, A. Allafort, L. Baldini, J. Ballet, G. Barbiellini, D. Bastieri, K. Bechtol, R. Bellazzini, B. Berenji, R. D. Blandford, E. D. Bloom, E. Bonamente, A. W. Borgland, A. Bouvier, T. J. Brandt, J. Bregeon, A. Brez, M. Brigida, P. Bruel, R. Buehler, S. Buson, G. A. Caliandro, R. A. Cameron, A. Cannon, P. A. Caraveo, J. M. Casandjian, Ö. Çelik, E. Charles, A. Chekhtman, C. C. Cheung, J. Chiang, S. Ciprini, R. Claus, J. Cohen-Tanugi, L. Costamante, S. Cutini, F. D'Ammando, C. D. Dermer, A. de Angelis, A. de Luca, F. de Palma, S. W. Digel, E. do Couto e Silva, P. S. Drell, A. Drlica-Wagner, R. Dubois, D. Dumora, C. Favuzzi, S. J. Fegan, E. C. Ferrara, W. B. Focke, P. Fortin, M. Frailis, Y. Fukazawa, S. Funk, P. Fusco, F. Gargano, D. Gasparrini, N. Gehrels, S. Germani, N. Giglietto, F. Giordano, M. Giroletti, T. Glanzman, G. Godfrey, I. A. Grenier, M. H. Grondin, J. E. Grove, S. Guiriec, D. Hadasch, Y. Hanabata, A. K. Harding, K. Hayashi, M. Hayashida, E. Hays, D. Horan, R. Itoh, G. Jóhannesson, A. S. Johnson, T. J. Johnson, D. Khangulyan, T. Kamae, H. Katagiri, J. Kataoka, M. Kerr, J. Knödlseder, M. Kuss, J. Lande, L. Latronico, S. H. Lee, M. Lemoine-Goumard, F. Longo, F. Loparco, P. Lubrano, G. M. Madejski, A. Makeev, M. Marelli, M. N. Mazziotta, J. E. McEnery, P. F. Michelson, W. Mitthumsiri, T. Mizuno, A. A. Moiseev, C. Monte, M. E. Monzani, A. Morselli, I. V. Moskalenko, S. Murgia, T. Nakamori, M. Naumann-Godo, P. L. Nolan, J. P. Norris, E. Nuss, T. Ohsugi, A. Okumura, N. Omodei, J. F. Ormes, M. Ozaki, D. Paneque, D. Parent, V. Pelassa, M. Pepe, M. Pesce-Rollins, M. Pierbattista, F. Piron, T. A. Porter, S. Rainò, R. Rando, P. S. Ray, M. Razzano, A. Reimer, O. Reimer, T. Reposeur, S. Ritz, R. W. Romani, H. F. W. Sadrozinski, D. Sanchez, P. M. Saz Parkinson, J. D. Scargle, T. L. Schalk, C. Sgrò, E. J. Siskind, P. D. Smith, G. Spandre, P. Spinelli, M. S. Strickman, D. J. Suson, H. Takahashi, T. Takahashi, T. Tanaka, J. B. Thayer, D. J. Thompson, L. Tibaldo, D. F. Torres, G. Tosti, A. Tramacere, E. Troja, Y. Uchiyama, J. Vandenbroucke, V. Vasileiou, G. Vianello, V. Vitale, P. Wang, K. S. Wood, Z. Yang, and M. Ziegler. 2011. Gamma-Ray Flares from the Crab Nebula. Science 331(6018):739. 1011.3855.

Achterberg, A. 1984. Stochastic Fermi acceleration and the origin of cosmic rays. *Advances* in Space Research 4(2-3):193–204.

Agudelo Rueda, J. A., D. Verscharen, R. T. Wicks, C. J. Owen, N. Nicolaou, A. P. Walsh, I. Zouganelis, K. Germaschewski, and S. Vargas Domínguez. 2021. Three-dimensional magnetic reconnection in particle-in-cell simulations of anisotropic plasma turbulence. *Journal of Plasma Physics* 87(3):905870228. 2103.13232.

Alexandrova, O., J. Saur, C. Lacombe, A. Mangeney, J. Mitchell, S. J. Schwartz, and P. Robert. 2009. Universality of Solar-Wind Turbulent Spectrum from MHD to Electron Scales. *Physical Review Letters* 103:165003.

Arons, J., and J. J. Barnard. 1986. Wave Propagation in Pulsar Magnetospheres: Dispersion Relations and Normal Modes of Plasmas in Superstrong Magnetic Fields. *The Astrophysical Journal* 302:120.

Begelman, Mitchell C., Roger D. Blandford, and Martin J. Rees. 1984. Theory of extragalactic radio sources. *Reviews of Modern Physics* 56(2):255–351.

Birn, J., J. F. Drake, M. A. Shay, B. N. Rogers, R. E. Denton, M. Hesse, M. Kuznetsova, Z. W. Ma, A. Bhattacharjee, A. Otto, and P. L. Pritchett. 2001. Geospace Environmental Modeling (GEM) magnetic reconnection challenge. *Journal of Geophysical Research* 106(A3): 3715–3720.

Biskamp, D. 2003. Magnetohydrodynamic Turbulence, Cambridge, UK: Cambridge University Press. Cambridge University Press.

Blandford, Roger, and David Eichler. 1987. Particle acceleration at astrophysical shocks: A theory of cosmic ray origin. *Physics Reports* 154(1):1–75.

Blum, Harry. 1967. A Transformation for Extracting New Descriptors of Shape. In *Models for the perception of speech and visual form*, ed. Weiant Wathen-Dunn, 362–380. Cambridge: MIT Press.

Boffetta, Guido, and Robert E. Ecke. 2012. Two-Dimensional Turbulence. *Annual Review of Fluid Mechanics* 44(1):427–451.

Boldyrev, S. 2005. On the Spectrum of Magnetohydrodynamic Turbulence. *The Astrophysical Journal Letters* 626:L37–L40. astro-ph/0503053.

Boldyrev, S., C. H. K. Chen, Q. Xia, and V. Zhdankin. 2015. Spectral Breaks of Alfvénic Turbulence in a Collisionless Plasma. *The Astrophysical Journal* 806:238. 1507.00416.

Boldyrev, S., J. Mason, and F. Cattaneo. 2009. Dynamic Alignment and Exact Scaling Laws in Magnetohydrodynamic Turbulence. *The Astrophysical Journal Letters* 699:L39–L42.

Boldyrev, S., J. C. Perez, and Y. Wang. 2012. Residual Energy in Weak and Strong MHD Turbulence. In *Numerical modeling of space plasma slows (astronum 2011)*, ed. N. V. Pogorelov, J. A. Font, E. Audit, and G. P. Zank, vol. 459 of *Astronomical Society of the Pacific Conference Series*, 3. 1202.3453.

Boldyrev, Stanislav. 2006. Spectrum of Magnetohydrodynamic Turbulence. *Physical Review Letters* 96(11):115002. astro-ph/0511290.

Boldyrev, Stanislav, Konstantinos Horaites, Qian Xia, and Jean Carlos Perez. 2013. Toward a Theory of Astrophysical Plasma Turbulence at Subproton Scales. *The Astrophysical Journal* 777(1):41.

Boldyrev, Stanislav, and Nuno F. Loureiro. 2019. Role of reconnection in inertial kinetic-Alfvén turbulence. *Physical Review Research* 1(1):012006. 1901.10096.

Boldyrev, Stanislav, Nuno F. Loureiro, and Vadim Roytershteyn. 2021. Plasma dynamics in low-electron-beta environments. Frontiers in Astronomy and Space Sciences 8:15.

Boldyrev, Stanislav, and Jean Carlos Perez. 2012. Spectrum of Kinetic-Alfvén Turbulence. The Astrophysical Journal Letters 758(2):L44. 1204.5809.

Boldyrev, Stanislav, Jean Carlos Perez, Joseph E. Borovsky, and John J. Podesta. 2011. Spectral Scaling Laws in Magnetohydrodynamic Turbulence Simulations and in the Solar Wind. *The Astrophysical Journal Letters* 741(1):L19. 1106.0700.

Bowers, K. J., B. J. Albright, L. Yin, B. Bergen, and T. J. T. Kwan. 2008. Ultrahigh performance three-dimensional electromagnetic relativistic kinetic plasma simulationa). *Physics of Plasmas* 15(5):055703.

Bresci, Virginia, Martin Lemoine, Laurent Gremillet, Luca Comisso, Lorenzo Sironi, and Camilia Demidem. 2022. Nonresonant particle acceleration in strong turbulence: Comparison to kinetic and MHD simulations. *Physical Review D* 106(2):023028. 2206.08380.

Bruno, Roberto, and Vincenzo Carbone. 2013. The Solar Wind as a Turbulence Laboratory. Living Reviews in Solar Physics 10(1):2.

Bühler, R., and R. Blandford. 2014. The surprising Crab pulsar and its nebula: a review. Reports on Progress in Physics 77(6):066901. 1309.7046.

Camporeale, E., L. Sorriso-Valvo, F. Califano, and A. Retinò. 2018. Coherent Structures and Spectral Energy Transfer in Turbulent Plasma: A Space-Filter Approach. *Physical Review Letters* 120(12):125101. 1711.00291.

Cassak, P. A., Y. H. Liu, and M. A. Shay. 2017. A review of the 0.1 reconnection rate problem. *Journal of Plasma Physics* 83(5):715830501. 1708.03449.

Cassak, P. A., and M. A. Shay. 2007. Scaling of asymmetric magnetic reconnection: General theory and collisional simulations. *Physics of Plasmas* 14(10):102114.

Chandran, B. D. G., A. A. Schekochihin, and A. Mallet. 2015. Intermittency and Alignment in Strong RMHD Turbulence. *The Astrophysical Journal* 807:39. 1403.6354.

Chen, C. H. K. 2016. Recent progress in astrophysical plasma turbulence from solar wind observations. *Journal of Plasma Physics* 82(6):535820602. 1611.03386.

Chen, C. H. K., S. D. Bale, C. S. Salem, and B. A. Maruca. 2013a. Residual Energy Spectrum of Solar Wind Turbulence. *The Astrophysical Journal* 770(2):125. 1304.7818.

Chen, C. H. K., and S. Boldyrev. 2017. Nature of Kinetic Scale Turbulence in the Earth's Magnetosheath. *The Astrophysical Journal* 842(2):122. 1705.08558.

Chen, C. H. K., S. Boldyrev, Q. Xia, and J. C. Perez. 2013b. Nature of Subproton Scale Turbulence in the Solar Wind. *Physical Review Letters* 110(22):225002. 1305.2950.

Chen, C. H. K., T. S. Horbury, A. A. Schekochihin, R. T. Wicks, O. Alexandrova, and J. Mitchell. 2010. Anisotropy of Solar Wind Turbulence between Ion and Electron Scales. *Physical Review Letters* 104:255002.

Chen, C. H. K., L. Leung, S. Boldyrev, B. A. Maruca, and S. D. Bale. 2014. Ion-scale spectral break of solar wind turbulence at high and low beta. *Geophysical Research Letters* 41:8081–8088.

Chen, C. H. K., A. Mallet, T. A. Yousef, A. A. Schekochihin, and T. S. Horbury. 2011. Anisotropy of Alfvénic turbulence in the solar wind and numerical simulations. *Monthly Notices of the Royal Astronomical Society* 415:3219–3226. 1009.0662.

Chen, C. H. K., C. S. Salem, J. W. Bonnell, F. S. Mozer, and S. D. Bale. 2012. Density Fluctuation Spectrum of Solar Wind Turbulence between Ion and Electron Scales. *Physical Review Letters* 109:035001.

Chernoglazov, Alexander, Bart Ripperda, and Alexander Philippov. 2021. Dynamic Alignment and Plasmoid Formation in Relativistic Magnetohydrodynamic Turbulence. *The Astrophysical Journal Letters* 923(1):L13. 2111.08188.

Cho, Jungyeon, and A. Lazarian. 2004. The Anisotropy of Electron Magnetohydrodynamic Turbulence. *The Astrophysical Journal Letters* 615(1):L41–L44. astro-ph/0406595.

Colagrossi, A., S. Marrone, P. Colagrossi, and D. Le Touzé. 2021. Da Vinci's observation of turbulence: A French-Italian study aiming at numerically reproducing the physics behind one of his drawings, 500 years later. *Physics of Fluids* 33(11):115122.

Comisso, L., and A. Bhattacharjee. 2016. On the value of the reconnection rate. *Journal of Plasma Physics* 82(6):595820601. 1609.02998.

Comisso, Luca, and Lorenzo Sironi. 2018. Particle Acceleration in Relativistic Plasma Turbulence. *Physical Review Letters* 121(25):255101. 1809.01168.

———. 2019. The Interplay of Magnetically Dominated Turbulence and Magnetic Reconnection in Producing Nonthermal Particles. *The Astrophysical Journal* 886(2):122. 1909.01420.

——. 2021. Pitch-Angle Anisotropy Controls Particle Acceleration and Cooling in Radiative Relativistic Plasma Turbulence. *Physical Review Letters* 127(25):255102. 2109.02666.

Daughton, W., T.K.M. K M Nakamura, H. Karimabadi, V. Roytershteyn, and B. Loring. 2014. Computing the reconnection rate in turbulent kinetic layers by using electron mixing to identify topology. *Physics of Plasmas* 21(5).

Davidson, Ronald C., and Edward A. Startsev. 2004. Self-consistent Vlasov-Maxwell description of the longitudinal dynamics of intense charged particle beams. *Physical Review Accelerators and Beams* 7(2):024401.

Delzanno, G.L. 2015. Multi-dimensional, fully-implicit, spectral method for the Vlasov—Maxwell equations with exact conservation laws in discrete form. *Journal of Computational Physics* 301:338–356.

Demidem, Camilia, Martin Lemoine, and Fabien Casse. 2020. Particle acceleration in relativistic turbulence: A theoretical appraisal. *Phys. Rev. D* 102(2):023003. 1909.12885.

Doss, C. E., C. M. Komar, P. A. Cassak, F. D. Wilder, S. Eriksson, and J. F. Drake. 2015. Asymmetric magnetic reconnection with a flow shear and applications to the magnetopause. *Journal of Geophysical Research (Space Physics)* 120(9):7748–7763. 1509.01575.

Drake, J. F., M. Swisdak, and R. Fermo. 2013. The Power-law Spectra of Energetic Particles during Multi-island Magnetic Reconnection. *The Astrophysical Journal Letters* 763(1):L5. 1210.4830.

Egedal, J., W. Fox, N. Katz, M. Porkolab, M. ØIeroset, R. P. Lin, W. Daughton, and J. F. Drake. 2008. Evidence and theory for trapped electrons in guide field magnetotail reconnection. *Journal of Geophysical Research (Space Physics)* 113(A12):A12207.

Ergun, R. E., N. Ahmadi, L. Kromyda, S. J. Schwartz, A. Chasapis, S. Hoilijoki, F. D. Wilder, P. A. Cassak, J. E. Stawarz, K. A. Goodrich, D. L. Turner, F. Pucci, A. Pouquet, W. H. Matthaeus, J. F. Drake, M. Hesse, M. A. Shay, R. B. Torbert, and J. L. Burch. 2020. Particle Acceleration in Strong Turbulence in the Earth's Magnetotail. *The Astrophysical Journal* 898(2):153.

Eyink, Gregory, Ethan Vishniac, Cristian Lalescu, Hussein Aluie, Kalin Kanov, Kai Bürger, Randal Burns, Charles Meneveau, and Alexander Szalay. 2013. Flux-freezing breakdown in high-conductivity magnetohydrodynamic turbulence. *Nature* 497(7450):466–469.

Eyink, Gregory L. 2018a. Cascades and Dissipative Anomalies in Nearly Collisionless Plasma Turbulence. *Physical Review X* 8(4):041020. 1803.03691.

——. 2018b. Review of the Onsager "Ideal Turbulence" Theory. arXiv e-prints arXiv:1803.02223. 1803.02223.

Fermi, Enrico. 1949. On the Origin of the Cosmic Radiation. *Physical Review* 75(8): 1169–1174.

French, Omar, Fan Guo, Qile Zhang, and Dmitri A. Uzdensky. 2023. Particle Injection and Nonthermal Particle Acceleration in Relativistic Magnetic Reconnection. *The Astrophysical Journal* 948(1):19. 2210.08358.

Frisch, U. 1995. Turbulence. The legacy of A. N. Kolmogorov. Cambridge University Press.

Gedalin, M., D. B. Melrose, and E. Gruman. 1998. Long waves in a relativistic pair plasma in a strong magnetic field. *Physical Review E* 57(3):3399-3410.

Godfrey, B. B., B. S. Newberger, and K. A. Taggart. 1975. A relativistic plasma dispersion function. *IEEE Transactions on Plasma Science* 3:60–67.

Goldreich, P., and S. Sridhar. 1995. Toward a theory of interstellar turbulence. 2: Strong alfvenic turbulence. The Astrophysical Journal 438:763–775.

Grošelj, Daniel, Hayk Hakobyan, Andrei M. Beloborodov, Lorenzo Sironi, and Alexander Philippov. 2024. Radiative Particle-in-Cell Simulations of Turbulent Comptonization in Magnetized Black-Hole Coronae. *Physical Review Letters* 132(8):085202. 2301.11327.

Grošelj, Daniel, Alfred Mallet, Nuno F. Loureiro, and Frank Jenko. 2018. Fully Kinetic Simulation of 3D Kinetic Alfvén Turbulence. *Physical Review Letters* 120(10):105101. 1710.03581.

Guo, Fan, Xiaocan Li, Omar French, Qile Zhang, William Daughton, Yi-Hsin Liu, William Matthaeus, Patrick Kilian, Grant Johnson, and Hui Li. 2023a. Comment on "Nonideal Fields Solve the Injection Problem in Relativistic Reconnection". *Physical Review Letters* 130(18):189501. 2208.03435.

Guo, Fan, Yi-Hsin Liu, Xiaocan Li, Hui Li, William Daughton, and Patrick Kilian. 2020. Recent progress on particle acceleration and reconnection physics during magnetic reconnection in the magnetically-dominated relativistic regime. *Physics of Plasmas* 27(8):080501. 2006.15288.

Guo, Fan, Yi-Hsin Liu, Seiji Zenitani, and Masahiro Hoshino. 2023b. Magnetic Reconnection and Associated Particle Acceleration in High-energy Astrophysics. *arXiv e-prints* arXiv:2309.13382. 2309.13382.

Haggerty, C. C., T. N. Parashar, W. H. Matthaeus, M. A. Shay, Y. Yang, M. Wan, P. Wu, and S. Servidio. 2017. Exploring the statistics of magnetic reconnection X-points in kinetic particle-in-cell turbulence. *Physics of Plasmas* 24(10):102308. 1706.04905.

Howes, G. G. 2015. A dynamical model of plasma turbulence in the solar wind. *Philosophical Transactions of the Royal Society of London Series A* 373(2041):20140145–20140145. **1502**. 04109.

Howes, G. G., J. M. TenBarge, W. Dorland, E. Quataert, A. A. Schekochihin, R. Numata, and T. Tatsuno. 2011. Gyrokinetic Simulations of Solar Wind Turbulence from Ion to Electron Scales. *Physical Review Letters* 107:035004.

Karimabadi, H., V. Roytershteyn, M. Wan, W. H. Matthaeus, W. Daughton, P. Wu, M. Shay, B. Loring, J. Borovsky, E. Leonardis, S. C. Chapman, and T. K. M. Nakamura. 2013. Coherent structures, intermittent turbulence, and dissipation in high-temperature plasmas. *Physics of Plasmas* 20(1):012303.

Kasper, J. C., K. G. Klein, E. Lichko, Jia Huang, C. H. K. Chen, S. T. Badman, J. Bonnell, P. L. Whittlesey, R. Livi, D. Larson, M. Pulupa, A. Rahmati, D. Stansby, K. E. Korreck, M. Stevens, A. W. Case, S. D. Bale, M. Maksimovic, M. Moncuquet, K. Goetz, J. S. Halekas, D. Malaspina, Nour E. Raouafi, A. Szabo, R. MacDowall, Marco Velli, Thierry Dudok de Wit, and G. P. Zank. 2021. Parker solar probe enters the magnetically dominated solar corona. *Phys. Rev. Lett.* 127:255101.

Kempski, Philipp, Drummond B. Fielding, Eliot Quataert, Alisa K. Galishnikova, Matthew W. Kunz, Alexander A. Philippov, and Bart Ripperda. 2023. Cosmic ray transport

in large-amplitude turbulence with small-scale field reversals. Monthly Notices of the RAS 525(4):4985–4998. 2304.12335.

Kiyani, K. H., S. C. Chapman, Y. V. Khotyaintsev, M. W. Dunlop, and F. Sahraoui. 2009. Global Scale-Invariant Dissipation in Collisionless Plasma Turbulence. *Physical Review Letters* 103:075006.

Klimchuk, James A. 2006. On Solving the Coronal Heating Problem. *Solar Physics* 234(1): 41–77. astro-ph/0511841.

Kolmogorov, A. 1941a. The local structure of turbulence in incompressible viscous fluid for very large Reynolds numbers. *Akademiia Nauk SSSR Doklady* 30:301–305.

Kolmogorov, Andrey Nikolaevich. 1941b. Dissipation of Energy in Locally Isotropic Turbulence. Akademiia Nauk SSSR Doklady 32:16–18.

Kraichnan, Robert H. 1967. Inertial Ranges in Two-Dimensional Turbulence. *Physics of Fluids* 10(7):1417–1423.

Kritsuk, A. G., S. D. Ustyugov, and M. L. Norman. 2017. The structure and statistics of interstellar turbulence. *New Journal of Physics* 19(6):065003. 1705.01912.

Kulsrud, Russell M., and Attilio Ferrari. 1971. The Relativistic Quasilinear Theory of Particle Acceleration by Hydromagnetic Turbulence. *Astrophysics and Space Science* 12(2): 302–318.

Lemoine, M., K. Murase, and F. Rieger. 2023. Nonlinear aspects of stochastic particle acceleration. arXiv e-prints arXiv:2312.04443. 2312.04443.

Lemoine, Martin. 2021. Particle acceleration in strong MHD turbulence. Physical Review D $104(6):063020.\ 2104.08199.$

Lemoine, Martin, Oscar Ramos, and Laurent Gremillet. 2016. Corrugation of Relativistic Magnetized Shock Waves. *The Astrophysical Journal* 827(1):44. 1607.00768.

Littlejohn, Robert G. 1983. Variational principles of guiding centre motion. *Journal of Plasma Physics* 29(1):111–125.

———. 1984. Linear relativistic gyrokinetic equation. *Physics of Fluids* 27(4):976–982.

Loureiro, Nuno F., and Stanislav Boldyrev. 2017. Role of Magnetic Reconnection in Magnetohydrodynamic Turbulence. *Physical Review Letters* 118(24):245101.

———. 2018. Turbulence in Magnetized Pair Plasmas. *The Astrophysical Journal Letters* 866(1):L14. 1805.09224.

Lysak, Robert L., and William Lotko. 1996. On the kinetic dispersion relation for shear Alfvén waves. *Journal of Geophysics Research* 101(A3):5085–5094.

Mallet, A., A. A. Schekochihin, and B. D. G. Chandran. 2017. Disruption of sheet-like structures in Alfvénic turbulence by magnetic reconnection. *Monthly Notices of the RAS* 468(4):4862–4871. 1612.07604.

Mandt, M. E., R. E. Denton, and J. F. Drake. 1994. Transition to whistler mediated magnetic reconnection. *Geophysical Research Letters* 21(1):73–76.

Marcowith, A., A. Bret, A. Bykov, M. E. Dieckman, L. O'C Drury, B. Lembège, M. Lemoine, G. Morlino, G. Murphy, G. Pelletier, I. Plotnikov, B. Reville, M. Riquelme, L. Sironi, and A. Stockem Novo. 2016. The microphysics of collisionless shock waves. *Reports on Progress in Physics* 79(4):046901. 1604.00318.

Maron, J., and P. Goldreich. 2001. Simulations of Incompressible Magnetohydrodynamic Turbulence. *The Astrophysical Journal* 554:1175–1196. astro-ph/0012491.

Marusic, Ivan, and Susan Broomhall. 2021. Leonardo da Vinci and Fluid Mechanics. *Annual Review of Fluid Mechanics* 53:1–25.

Mason, J., F. Cattaneo, and S. Boldyrev. 2008. Numerical measurements of the spectrum in magnetohydrodynamic turbulence. *Physical Review E* 77(3):036403. 0706.2003.

Mason, J., J. C. Perez, S. Boldyrev, and F. Cattaneo. 2012. Numerical simulations of strong incompressible magnetohydrodynamic turbulence. *Physics of Plasmas* 19(5):055902–055902. 1202.3474.

Mason, Joanne, Fausto Cattaneo, and Stanislav Boldyrev. 2006. Dynamic Alignment in Driven Magnetohydrodynamic Turbulence. *Physical Review Letters* 97(25):255002. astro-ph/0602382.

Matteini, L., O. Alexandrova, C. H. K. Chen, and C. Lacombe. 2017. Electric and magnetic spectra from MHD to electron scales in the magnetosheath. *Monthly Notices of the RAS* 466(1):945–951.

Matthaeus, W. H., and M. Velli. 2011. Who Needs Turbulence?. A Review of Turbulence Effects in the Heliosphere and on the Fundamental Process of Reconnection. *Space Science Reviews* 160(1-4):145–168.

Mihalas, D., and B. W. Mihalas. 1999. Foundations of radiation hydrodynamics. Dover.

Milanese, Lucio M., Nuno F. Loureiro, Maximilian Daschner, and Stanislav Boldyrev. 2020. Dynamic Phase Alignment in Inertial Alfvén Turbulence. *Physical Review Letters* 125(26): 265101. 2010.00415.

Müller, W.-C., and R. Grappin. 2005. Spectral Energy Dynamics in Magnetohydrodynamic Turbulence. *Physical Review Letters* 95(11):114502. physics/0509019.

Müller, Wolf-Christian, Dieter Biskamp, and Roland Grappin. 2003. Statistical anisotropy of magnetohydrodynamic turbulence. *Physical Review E* 67(6):066302. physics/0306045.

Nättilä, Joonas, and Andrei M. Beloborodov. 2021. Radiative Turbulent Flares in Magnetically Dominated Plasmas. *The Astrophysical Journal* 921(1):87. 2012.03043.

———. 2022. Heating of Magnetically Dominated Plasma by Alfvén-Wave Turbulence. *Physical Review Letters* 128(7):075101. 2111.15578.

Navier, C. L. M. H. 1823. Mémoire sur les lois du mouvement des fluides. *Mém. Acad. Roy. Sci.* 6:389–440.

Northrop, G., Theodore. 1963. The Adiabatic Motion of Charged Particles (Interscience Publishers, Inc., John Wiley & Sons, New York). Inderscience Publishers.

Obukhov, A. M. 1941. On the distribution of energy in the spectrum of turbulent flow. Akademiia Nauk SSR Doklady 32:22–24.

Øksendal, B. 2003. Stochastic differential equations. Springer.

Oughton, S., W. H. Matthaeus, and P. Dmitruk. 2017. Reduced MHD in Astrophysical Applications: Two-dimensional or Three-dimensional? *The Astrophysical Journal* 839(1):2.

Papini, Emanuele, Luca Franci, Simone Landi, Andrea Verdini, Lorenzo Matteini, and Petr Hellinger. 2019. Can Hall Magnetohydrodynamics Explain Plasma Turbulence at Sub-ion Scales? *The Astrophysical Journal* 870(1):52. 1810.02210.

Parker, E. N. 1990. Intrinsic magnetic discontinuities and solar X-ray emission. *Geophysical Research Letters* 17(11):2055–2058.

Parnell, C. E., and I. De Moortel. 2012. A contemporary view of coronal heating. *Philosophical Transactions of the Royal Society of London Series A* 370(1970):3217–3240. 1206.6097.

Passot, T., P. L. Sulem, and E. Tassi. 2017. Electron-scale reduced fluid models with gyroviscous effects. *Journal of Plasma Physics* 83(4):715830402. 1704.02576.

——. 2018. Gyrofluid modeling and phenomenology of low- β_e Alfvén wave turbulence. Physics of Plasmas 25(4):042107. 1801.06120.

Perez, J. C., and S. Boldyrev. 2008. On Weak and Strong Magnetohydrodynamic Turbulence. The Astrophysical Journal Letters 672:L61. 0712.2086. Perez, J. C., J. Mason, S. Boldyrev, and F. Cattaneo. 2012. On the Energy Spectrum of Strong Magnetohydrodynamic Turbulence. *Physical Review X* 2(4):041005. 1209.2011.

Pezzi, Oreste, Pasquale Blasi, and William H. Matthaeus. 2022. Relativistic Particle Transport and Acceleration in Structured Plasma Turbulence. *The Astrophysical Journal* 928(1):25. 2112.09555.

Phan, T. D., J. P. Eastwood, M. A. Shay, J. F. Drake, B. U. Ö. Sonnerup, M. Fujimoto, P. A. Cassak, M. Øieroset, J. L. Burch, R. B. Torbert, A. C. Rager, J. C. Dorelli, D. J. Gershman, C. Pollock, P. S. Pyakurel, C. C. Haggerty, Y. Khotyaintsev, B. Lavraud, Y. Saito, M. Oka, R. E. Ergun, A. Retino, O. Le Contel, M. R. Argall, B. L. Giles, T. E. Moore, F. D. Wilder, R. J. Strangeway, C. T. Russell, P. A. Lindqvist, and W. Magnes. 2018. Electron magnetic reconnection without ion coupling in Earth's turbulent magnetosheath. *Nature* 557:202–206.

Podesta, J. J., B. D. G. Chandran, A. Bhattacharjee, D. A. Roberts, and M. L. Goldstein. 2009. Scale-dependent angle of alignment between velocity and magnetic field fluctuations in solar wind turbulence. *Journal of Geophysical Research (Space Physics)* 114:A01107.

Pongkitiwanichakul, Peera, and Benjamin D. G. Chandran. 2014. Stochastic Acceleration of Electrons by Fast Magnetosonic Waves in Solar Flares: The Effects of Anisotropy in Velocity and Wavenumber Space. *The Astrophysical Journal* 796(1):45. 1406.0802.

Pyakurel, P. S., M. A. Shay, J. F. Drake, T. D. Phan, P. A. Cassak, and J. L. Verniero. 2021. Faster Form of Electron Magnetic Reconnection with a Finite Length X-Line. *Physical Review Letters* 127(15):155101.

Richardson, L. F. 1922. Weather prediction by numerical process. Cambridge University Press.

Roberts, K. V., and H. L. Berk. 1967. Nonlinear Evolution of a Two-Stream Instability. *Physical Review Letters* 19(6):297–300.

Roytershteyn, V., S. Boldyrev, G. L. Delzanno, C. H. K. Chen, D. Grošelj, and N. F. Loureiro. 2018. Inertial Kinetic-Alfv\'en Turbulence. arXiv e-prints. 1810.12428.

Roytershteyn, Vadim, Stanislav Boldyrev, Gian Luca Delzanno, Christopher H. K. Chen, Daniel Grošelj, and Nuno F. Loureiro. 2019. Numerical Study of Inertial Kinetic-Alfvén Turbulence. *The Astrophysical Journal* 870(2):103.

Sahraoui, F., S. Y. Huang, G. Belmont, M. L. Goldstein, A. Rétino, P. Robert, and J. De Patoul. 2013a. Scaling of the Electron Dissipation Range of Solar Wind Turbulence. *The Astrophysical Journal* 777(1):15. 1303.7394.

———. 2013b. Scaling of the Electron Dissipation Range of Solar Wind Turbulence. *The Astrophysical Journal* 777:15.

Schekochihin, A. A., S. C. Cowley, W. Dorland, G. W. Hammett, G. G. Howes, E. Quataert, and T. Tatsuno. 2009. Astrophysical Gyrokinetics: Kinetic and Fluid Turbulent Cascades in Magnetized Weakly Collisional Plasmas. *The Astrophysical Journal, Supplement* 182(1): 310–377. 0704.0044.

Schekochihin, Alexander A. 2022. MHD turbulence: a biased review. *Journal of Plasma Physics* 88(5):155880501. 2010.00699.

Schekochihin, Alexander A., Steven C. Cowley, Samuel F. Taylor, Jason L. Maron, and James C. McWilliams. 2004. Simulations of the Small-Scale Turbulent Dynamo. *The Astrophysical Journal* 612(1):276–307. astro-ph/0312046.

Scudder, Jack, and William Daughton. 2008. Illuminating electron diffusion regions of collisionless magnetic reconnection using electron agyrotropy. *Journal of Geophysical Research: Space Physics* 113(6):1–16.

Selkowitz, Robert, and Eric G. Blackman. 2004. Stochastic Fermi acceleration of subrelativistic electrons and its role in impulsive solar flares. *Monthly Notices of the RAS* 354(327): 870–882. astro-ph/0407504.

Servidio, S., W. H. Matthaeus, M. A. Shay, P. A. Cassak, and P. Dmitruk. 2009. Magnetic Reconnection in Two-Dimensional Magnetohydrodynamic Turbulence. *Physical Review Letters* 102(11):115003.

Sharma Pyakurel, P., M. A. Shay, T. D. Phan, W. H. Matthaeus, J. F. Drake, J. M. TenBarge, C. C. Haggerty, K. G. Klein, P. A. Cassak, T. N. Parashar, M. Swisdak, and A. Chasapis. 2019. Transition from ion-coupled to electron-only reconnection: Basic physics and implications for plasma turbulence. *Physics of Plasmas* 26(8):082307. 1901.09484.

Shi, Chen, Marco Velli, Roberto Lionello, Nikos Sioulas, Zesen Huang, Jasper S. Halekas, Anna Tenerani, Victor Réville, Jean-Baptiste Dakeyo, Milan Maksimović, and Stuart D. Bale. 2023. Proton and Electron Temperatures in the Solar Wind and Their Correlations with the Solar Wind Speed. *The Astrophysical Journal* 944(1):82. 2301.00852.

Sironi, Lorenzo. 2022. Nonideal Fields Solve the Injection Problem in Relativistic Reconnection. *Physical Review Letters* 128(14):145102. 2203.04342.

Sironi, Lorenzo, and Anatoly Spitkovsky. 2014. Relativistic Reconnection: An Efficient Source of Non-thermal Particles. *The Astrophysical Journal Letters* 783(1):L21. 1401.5471.

Stawarz, J. E., J. P. Eastwood, T. D. Phan, I. L. Gingell, M. A. Shay, J. L. Burch, R. E. Ergun, B. L. Giles, D. J. Gershman, O. Le Contel, P. A. Lindqvist, C. T. Russell, R. J. Strangeway, R. B. Torbert, M. R. Argall, D. Fischer, W. Magnes, and L. Franci. 2019. Properties of the Turbulence Associated with Electron-only Magnetic Reconnection in Earth's Magnetosheath. *The Astrophysical Journal Letters* 877(2):L37.

Stokes, G. G. 1843. On some cases of fluid motion. Camb. Phil. Soc. 8:105.

Stone, James M., Eve C. Ostriker, and Charles F. Gammie. 1998. Dissipation in Compressible Magnetohydrodynamic Turbulence. *The Astrophysical Journal Letters* 508(1):L99–L102. astro-ph/9809357.

Streltsov, A., and W. Lotko. 1995. Dispersive field line resonances on auroral field lines. Journal of Geophysics Research 100(A10):19457–19472.

Svensson, R. 1982. Electron-Positron Pair Equilibria in Relativistic Plasmas. *The Astro*physical Journal 258:335.

Tavani, M., A. Bulgarelli, V. Vittorini, A. Pellizzoni, E. Striani, P. Caraveo, M. C. Weisskopf,
A. Tennant, G. Pucella, A. Trois, E. Costa, Y. Evangelista, C. Pittori, F. Verrecchia, E. Del
Monte, R. Campana, M. Pilia, A. De Luca, I. Donnarumma, D. Horns, C. Ferrigno, C. O.
Heinke, M. Trifoglio, F. Gianotti, S. Vercellone, A. Argan, G. Barbiellini, P. W. Cattaneo,
A. W. Chen, T. Contessi, F. D'Ammando, G. DeParis, G. Di Cocco, G. Di Persio, M. Feroci,
A. Ferrari, M. Galli, A. Giuliani, M. Giusti, C. Labanti, I. Lapshov, F. Lazzarotto, P. Lipari,
F. Longo, F. Fuschino, M. Marisaldi, S. Mereghetti, E. Morelli, E. Moretti, A. Morselli,
L. Pacciani, F. Perotti, G. Piano, P. Picozza, M. Prest, M. Rapisarda, A. Rappoldi, A. Rubini,
S. Sabatini, P. Soffitta, E. Vallazza, A. Zambra, D. Zanello, F. Lucarelli, P. Santolamazza,
P. Giommi, L. Salotti, and G. F. Bignami. 2011. Discovery of Powerful Gamma-Ray Flares
from the Crab Nebula. Science 331(6018):736. 1101.2311.

Teller, Edward. 1954. Theory of Origin of Cosmic Rays. Reports on Progress in Physics 17(1):154–172.

TenBarge, J. M., and G. G. Howes. 2012. Evidence of critical balance in kinetic Alfvén wave turbulence simulations a). *Physics of Plasmas* 19(5):055901. 1201.0056.

TenBarge, J. M., B. Ripperda, A. Chernoglazov, A. Bhattacharjee, J. F. Mahlmann, E. R. Most, J. Juno, Y. Yuan, and A. A. Philippov. 2021. Weak Alfvénic turbulence in relativistic plasmas. Part 1. Dynamical equations and basic dynamics of interacting resonant triads. *Journal of Plasma Physics* 87(6):905870614. 2105.01146.

Tobias, S. M., F. Cattaneo, and S. Boldyrev. 2013. MHD Dynamos and Turbulence, in Ten Chapters in Turbulence, ed. P.A. Davidson, Y. Kaneda, and K.R. Sreenivasan: Cambridge University Press, p. 351-404. . 1103.3138.

Trotta, Domenico, Luca Franci, David Burgess, and Petr Hellinger. 2020. Fast Acceleration of Transrelativistic Electrons in Astrophysical Turbulence. *The Astrophysical Journal* 894(2): 136. 1910.11935.

Uzdensky, Dmitri A., Benoît Cerutti, and Mitchell C. Begelman. 2011. Reconnection-powered Linear Accelerator and Gamma-Ray Flares in the Crab Nebula. *The Astrophysical Journal Letters* 737(2):L40. 1105.0942.

Vega, Cristian, Stanislav Boldyrev, and Vadim Roytershteyn. 2022a. Spectra of Magnetic Turbulence in a Relativistic Plasma. *The Astrophysical Journal Letters* 931(1):L10. 2204. 04530.

———. 2024a. Particle acceleration in relativistic Alfvénic turbulence. In preparation.

——. 2024b. Relativistic Alfvén Turbulence at Kinetic Scales. *The Astrophysical Journal* 965(1):27. 2402.16218.

Vega, Cristian, Stanislav Boldyrev, Vadim Roytershteyn, and Mikhail Medvedev. 2022b. Turbulence and Particle Acceleration in a Relativistic Plasma. *The Astrophysical Journal Letters* 924(1):L19. 2111.04907.

Vega, Cristian, Vadim Roytershteyn, Gian Luca Delzanno, and Stanislav Boldyrev. 2020. Electron-only Reconnection in Kinetic-Alfvén Turbulence. *The Astrophysical Journal Letters* 893(1):L10.

———. 2023b. Electron-scale current sheets and energy dissipation in 3D kinetic-scale plasma turbulence with low electron beta. *Monthly Notices of the RAS* 524(1):1343–1351. 2306.01932.

Wan, M., W. H. Matthaeus, H. Karimabadi, V. Roytershteyn, M. Shay, P. Wu, W. Daughton, B. Loring, and S. C. Chapman. 2012. Intermittent Dissipation at Kinetic Scales in Collisionless Plasma Turbulence. *Physical Review Letters* 109(19):195001.

Wan, M., W. H. Matthaeus, V. Roytershteyn, H. Karimabadi, T. Parashar, P. Wu, and M. Shay. 2015. Intermittent Dissipation and Heating in 3D Kinetic Plasma Turbulence. *Physical Review Letters* 114(17):175002.

Wan, M., W. H. Matthaeus, V. Roytershteyn, T. N. Parashar, P. Wu, and H. Karimabadi. 2016. Intermittency, coherent structures and dissipation in plasma turbulence. *Physics of Plasmas* 23(4):042307.

Wang, Chih-Ping, Matina Gkioulidou, Larry R. Lyons, and Vassilis Angelopoulos. 2012. Spatial distributions of the ion to electron temperature ratio in the magnetosheath and plasma sheet. *Journal of Geophysical Research (Space Physics)* 117(A8):A08215.

Wong, Kai, Vladimir Zhdankin, Dmitri A. Uzdensky, Gregory R. Werner, and Mitchell C. Begelman. 2020. First-principles Demonstration of Diffusive-advective Particle Acceleration in Kinetic Simulations of Relativistic Plasma Turbulence. *The Astrophysical Journal Letters* 893(1):L7. 1901.03439.

Xu, Siyao, and Alex Lazarian. 2023. Turbulent Reconnection Acceleration. *The Astrophysical Journal* 942(1):21. 2211.08444.

Yan, Huirong, A. Lazarian, and Vahé Petrosian. 2008. Particle Acceleration by Fast Modes in Solar Flares. *The Astrophysical Journal* 684(2):1461–1468. 0801.3786.

Yang, Y., W. H. Matthaeus, T. N. Parashar, C. C. Haggerty, V. Roytershteyn, W. Daughton, M. Wan, Y. Shi, and S. Chen. 2017. Energy transfer, pressure tensor, and heating of kinetic plasma. *Physics of Plasmas* 24(7):072306.

Yang, Yan, William H. Matthaeus, Sohom Roy, Vadim Roytershteyn, Tulasi N. Parashar, Riddhi Bandyopadhyay, and Minping Wan. 2022. Pressure-Strain Interaction as the Energy Dissipation Estimate in Collisionless Plasma. *The Astrophysical Journal* 929(2):142. 2202. 02409.

Yuan, Feng, and Ramesh Narayan. 2014. Hot Accretion Flows Around Black Holes. *Annual Review of Astronomy and Astrophysics* 52:529–588. 1401.0586.

Zhdankin, V., S. Boldyrev, J. C. Perez, and S. M. Tobias. 2014. Energy Dissipation in Magnetohydrodynamic Turbulence: Coherent Structures or "Nanoflares"? *The Astrophysical Journal* 795:127. 1409.3285.

Zhdankin, V., D. A. Uzdensky, J. C. Perez, and S. Boldyrev. 2013. Statistical Analysis of Current Sheets in Three-dimensional Magnetohydrodynamic Turbulence. *The Astrophysical Journal* 771:124. 1302.1460.

Zhdankin, Vladimir. 2021. Particle Energization in Relativistic Plasma Turbulence: Solenoidal versus Compressive Driving. *The Astrophysical Journal* 922(2):172. 2106.00743.

Zhdankin, Vladimir, Stanislav Boldyrev, and Christopher H. K. Chen. 2016. Intermittency of energy dissipation in Alfvénic turbulence. *Monthly Notices of the RAS* 457(1):L69–L73. 1512.07355.

Zhdankin, Vladimir, Stanislav Boldyrev, and Joanne Mason. 2012a. Distribution of Magnetic Discontinuities in the Solar Wind and in Magnetohydrodynamic Turbulence. *The Astrophysical Journal Letters* 760(2):L22. 1210.3613.

Zhdankin, Vladimir, Stanislav Boldyrev, Joanne Mason, and Jean Carlos Perez. 2012b. Magnetic Discontinuities in Magnetohydrodynamic Turbulence and in the Solar Wind. *Physical Review Letters* 108(17):175004. 1204.4479.

Zhdankin, Vladimir, Dmitri A. Uzdensky, and Matthew W. Kunz. 2021. Production and Persistence of Extreme Two-temperature Plasmas in Radiative Relativistic Turbulence. *The Astrophysical Journal* 908(1):71. 2007.12050.

Zhdankin, Vladimir, Dmitri A. Uzdensky, Gregory R. Werner, and Mitchell C. Begelman. 2018a. Numerical investigation of kinetic turbulence in relativistic pair plasmas - I. Turbulence statistics. *Monthly Notices of the RAS* 474(2):2514–2535. 1709.04963.

——. 2018b. System-size Convergence of Nonthermal Particle Acceleration in Relativistic Plasma Turbulence. *The Astrophysical Journal Letters* 867(1):L18. 1805.08754.

———. 2019. Electron and Ion Energization in Relativistic Plasma Turbulence. *Physical Review Letters* 122(5):055101. 1809.01966.

Zhdankin, Vladimir, Gregory R. Werner, Dmitri A. Uzdensky, and Mitchell C. Begelman. 2017. Kinetic Turbulence in Relativistic Plasma: From Thermal Bath to Nonthermal Continuum. *Physical Review Letters* 118(5):055103. 1609.04851.

Zhou, Muni, Zhuo Liu, and Nuno F. Loureiro. 2023. Spectrum of kinetic-Alfvén-wave turbulence: intermittency or tearing mediation? *Monthly Notices of the RAS* 524(4): 5468–5476. 2208.02441.

Zinn-Justin, Jean. 2021. Quantum Field Theory and Critical Phenomena: Fifth Edition (5th edn). Oxford University Press.

Zrake, Jonathan, and Andrew I. MacFadyen. 2012. Numerical Simulations of Driven Relativistic Magnetohydrodynamic Turbulence. *The Astrophysical Journal* 744(1):32. 1108. 1991.

Zweibel, Ellen G., and Masaaki Yamada. 2009. Magnetic reconnection in astrophysical and laboratory plasmas. *Annual Review of Astronomy and Astrophysics* 47(1):291–332.

Zweibel, Ellen G., and Masaaki Yamada. 2016. Perspectives on magnetic reconnection. Proceedings of the Royal Society of London Series A 472(2196):20160479.